Development of Ultra Low-Temperature Electronics for the AEgIS Experiment

Thomas Kaltenbacher

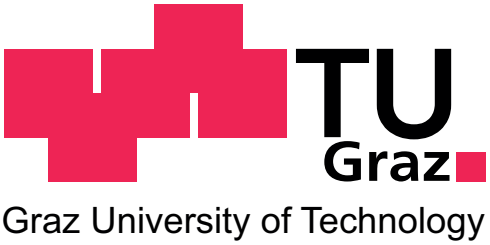

A dissertation submitted to the Graz University of Technology in accordance with the requirements of the degree of "Dr.techn."

Supervisor: Univ.-Prof. Dipl.-Ing. Dr.techn. Wolfgang PRIBYL
Co-Supervisor: Priv.-Doz. Dr. Alban KELLERBAUER
CERN Supervisor: Dr. Michael DOSER
CERN Co-Supervisor: Dr. Friedhelm CASPERS

Graz, February 2013

Eidesstattliche Erklärung

Ich erkläre an Eides statt, dass ich die vorliegende Arbeit selbstständig verfasst, andere als die angegebenen Quellen/Hilfsmittel nicht benutzt, und die den benutzten Quellen wörtlich und inhaltlich entnommenen Stellen als solche kenntlich gemacht habe.

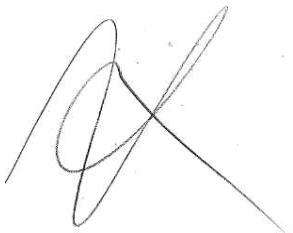

Graz, am 19.01.2013 .....

(Unterschrift)

Statutory Declaration

I declare that I have authored this thesis independently, that I have not used other than the declared sources/resources, and that I have explicitely marked all material which has been quotes either literally or by content from the used sources.

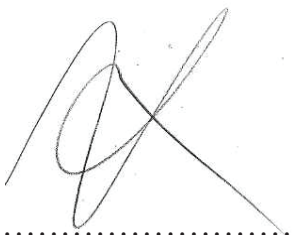

19th JAN 2013 .....

date (signature)

Acknowledgments

During my stay at CERN I have met many brilliant and helpful persons who contributed in many different ways to my work and for this I would like to say THANK YOU to all of them.
I want to thank Michael Doser and Wolfgang Pribyl for being my supervisors and guiding my work so that I could succeed eventually, and Wolfgang Bösch for his administrative support and for providing software tools. Furthermore, I am very grateful for the support of my co-supervisor Fritz Caspers and Stefan Ulmer, who gave me a helping hand and who always answered my numerous questions concerning cryogenic electronics and RF topics.
Thank you Stefan Stahl and Randall Kirschman for your feedback and expertise and knowledge you have shared with me. My thanks also go to Alban Kellerbauer, who gave me the chance to use his Penning trap setup at the MPI-K institute in Heidelberg and for his support as well as correcting my thesis.
Thanks to Richard Beltron and Olaf Dunkel who were winding the superconducting coils for me at CERN. My thanks also go to Philipp Ranitzsch and Philipp Bräunig for giving me a helping hand during my stay at the KIP in Heidelberg.
I have to thank Silke Federmann, William Creus and Michael Betz for many inspiring discussions during countless coffee breaks. A big "thank you" goes to the Cryo Lab at CERN, especially Johan Bremer, Claire Henriroux, Hendrik Derking, Carlos Rementeria, Tomasz Sliwinski, Christoph Balle, Gerhard Burghart, Jean-Louis Servais, Jean-Luc Carpano, Laetitia Dufay-Chanat, Pier Paolo Granieri and Thomas Eisel for supporting my cryogenic measurement activities.
I am indebted to Christian Löffler, Bernard Cantin and Joseph Samaniego-Evans for their technical and engineering support. I would like to thank Montserrat Fernandez-Bolaños and Pavel Kejik at EPFL in Lausanne for providing MEMS switches I could test and for the gold ball bonding. Thank you Bruno Reig for sending me numerous MEMS switches and the useful background information.
Thank you Mikio Fujiwara for sending me GaAs JFETs and Ian Mcgill for the aluminum

wedge bonding of them at CERN. I would also like to thank Andreas Knecht and James Storey for correcting this thesis.
Thanks to my parents Anna and Otto, who always supported me mentally and financially. Last but definitely not least, I would like to thank Agnieszka, my lovely girlfriend, for supporting and staying with me without reservation.

Abstract

This thesis presents the development of electronics for operation at cryogenic temperatures, with particular emphasis on the cryogenic electronics required for the Antimatter Experiment: Gravity, Interferometry, Spectroscopy (AE$\bar{g}$IS) experiment at the European Organisation for Nuclear Research (CERN). The research is focused on a highly sensitive charged particle detection system for a Penning trap, on cryogenic low-pass filters and on a low-loss DC-contact RF switch. The detection system consists of a high quality factor tuned circuit including a superconducting coil, and a low-noise amplifier. Since the experimental setup of the AE$\bar{g}$IS experiment requires it, the developed electronics must reliably operate at 4.2 K ($\sim -269°$C) and in high constant magnetic field of more than 1 Tesla. Therefore, the performance of the cryogenic electronic designs were carefully evaluated at low-temperature/high magnetic field, the result of which have important implications for the AE$\bar{g}$IS experiment. Moreover, a new possibility of replacing the superconducting coil by a very high quality factor crystal resonator is presented and its possible application in experiments with charged, trapped particles is described.

Kurzfassung

Diese Dissertation beschreibt die Entwicklung und den Aufbau von Tiefsttemperatur-Elektronik (Kryoelektronik), die fuer das Antimaterie-Experiment AE$\bar{g}$IS (Antimatter Experiment: Gravity, Interferometry, Spectroscopy) am Forschungszentrum der Europäischen Organisation fuer Kernforschung (CERN). Diese Elektronik-Komponenten beinhalten ein sehr empfindliches Detektionssystem für geladene Teilchen, gefangen in einer Penning-Falle, kryogene Tiefpassfilter und einem verlustarmen Hochfrequenz-Schalter mit ohmschen Kontakt. Die Detektionseinheit ist aus einem Resonator mit supraleitender Spule und einem rauscharmen Verstärker aufgebaut. Da das AE$\bar{g}$IS-Experiment bei 4.2 K (ca. $-269°$C) und in einem hohen Gleichmagnetfeld von mindestens 1 Tesla betrieben wird, müssen auch die vorher genannten Komponenten in dieser Umgebung zuverlässig funktionieren. Um dieses Ziel zu erreichen, wurde die entwickelte Elektronik bei kryogenen Temperaturen und im hohen Magnetfeld getestet. Die Ergebnisse dieser Evaluierung sind sehr wichtig fuer das Experiment. Es wurde auch eine neue Möglichkeit aufgezeigt, wie man die vorher genannte supraleitende Spule durch einen Quarzresonator

ersetzen kann und somit Vorteile für Experimente mit gespeicherten, geladenen Teilchen bieten könnte.

List of Abbreviations

$\bar{\mathrm{H}}$	Antihydrogen
$\bar{\mathrm{n}}$	Antineutron; antiparticle of the neutron
$\bar{\mathrm{p}}$	Antiproton; negatively charged proton
ϵ_0	Vacuum permittivity; $\epsilon_0 \approx 8.854187 \times 10^{-12}$ F/m
$\mathbf{\Gamma}$-plane	Complex reflection coefficient plane
$\mathbf{Z}$-plane	Complex impedance plane
e^+	Positron or anti-electron; positively charged electron
RuO_2	Ruthenium dioxide
c	Speed of light in vacuum; $c = 299792458$ m/s
k	Boltzmann's constant; $k \approx 1.380648 \times 10^{-23}$ J/K
$\mathbf{B}$-field	Magnetic field
AC voltage/current	Alternating electrical voltage/current
ADS	Advanced Design System
AE$\bar{\mathrm{g}}$IS	Antimatter Experiment: Gravity, Interferometry, Spectroscopy
CERN	European Organization for Nuclear Research
CPT	Charge conjugation, Parity inversion, Time inversion
dBm	Absolute power in dB referred to 1 mW
DC voltage/current	Direct electrical voltage/current
DUT	Device Under Test
EIA	Electronic Industries Alliance

ESD	Electrostatic discharge
eV	Electronvolt; unit of energy 1eV $\approx 1.6 \times 10^{-19}$ J $\approx$ 11604.5 K
GaAs	Galium arsenide
GND	Electrical ground potential (signal or power supply)
GPIB	General Purpose Interface Bus
IL	Insertion Loss
LC filter	Inductor-Capacitor filter
LF	Low Frequency
LHe	Liquid helium; boiling point at 4.2 K under atmospheric pressure
LN	Liquid nitrogen; boiling point at 77 K under atmospheric pressure
MEMS	Microelectromechanical Systems
mil	thousandth of an inch (25.4 μm)
MMIC	Monolithic Microwave Integrated Circuit
NbTi	Niobium-titanium
NP0, C0G	Class of low dielectric constant material; Negative Positive Zero Capacitance/Temperature Dependence
PCB	Printed Circuit Board
PEM	Plastic Encapsulated Microcircuit
Ps	Positronium; meta-stable bound state of positron and electron
PZT	Lead Zirconate Titanate
Q-factor	Quality factor of resonating systems
RC filter	Resistor-Capacitor filter
RF	Radio Freqeuncy
RRR	Residual Resistivity Ratio
SA	Spectrum Analyzer

Si	Silicon
SMD	Surface Mounted Device
SMT	Surface Mounted Technology
SMU	Source Monitor Unit
SOIC	Small Outline Integrated Circuit
SPICE	Simulation Program with Integrated Circuit Emphasis
UHV	Ultra High Vacuum
VNA	Vector Network Analyzer

Contents

Motivation for Cryogenic Electronics Research

Cryogenic environments are defined to be below -150 °C or $\sim$ 123 K in temperature. Since decades, low-temperature is considered as design parameter for improving the performance of electronic systems. For instance, microwave receivers used for radio astronomy (noise reduction) or supercomputers (higher clock rates) are operated at liquid nitrogen temperature (77 K). Other applications such as deep-space mission equipment or experiments conducted at cryogenic temperature represent an environment where electronics has to operate. Since conventional electronic components are usually not specified for temperatures below -55 °C or $\sim$ 218 K, those devices have to be characterized at low-temperature. Usually, material properties and device behavior change significantly upon cooling. Therefore, all important changes in the device behavior have to be carefully evaluated and considered in the low-temperature (compatible) electronic design. Moreover, usually there are no models for simulation of electronic components, especially semiconductors, available at cryogenic temperatures. As a consequence, a lot of effort has to be invested into the parameter extraction of materials and devices in order to describe the effective changes upon cooling. Another very important point is to design cryogenic electronics such that they are very reliable, since low-temperature environments are usually inaccessible for maintenance especially in case of a running experiment.

1. Introduction

There remain many open questions concerning the universe and all the matter in it. One of the biggest mystery is "where is all the antimatter gone?" since matter and antimatter "always" appear in pairs. Under the assumption of perfect symmetry between matter and antimatter, every particle would either have had to annihilate with its antiparticle, leading to a photon-dominated universe, or else, large domains of the universe have to consist exclusively of antimatter. Neither of these options appears to be realized. A difference has been found between the behavior of matter and antimatter, but it is too small to explain our observed matter dominated universe[1]. Another question is the gravitational interaction of matter and antimatter. "Will antimatter fall up or down in the gravitational field of our earth?" The following two sections will present an introduction to the most important findings concerning antimatter and the AEgIS experiment at the European Organization for Nuclear Research (CERN). The AEgIS collaboration proposes to perform the very first direct measurement of gravitational interaction between matter and antimatter using antihydrogen ($\bar{H}$) atoms. Antihydrogen is the bound state of an antiproton ($\bar{p}$) and a positron (e^+) and represents the simplest stable system of bound antimatter. Furthermore, high precision tests performed with $\bar{H}$ could lead to deeper understanding of the laws of nature.

1.1. Antimatter and Antimatter Experiments - A brief historical review

The history of antimatter began with its first prediction by Paul Dirac in 1928 when he combined Einsteins's special relativity with quantum mechanics [1]. It took four more years in order to show the first evidence[2] that the the positively charged electron - the so-

[1] Symmetry (CP) violations were found in the kaon and B-meson systems. However, they are too small to explain the large asymmetry.

[2] Already in 1923 photographs of cloud chamber experiments showed tracks of positrons but no one could interpret them as positively charged electrons [2].

called positron (e^+; also called anti-electron) - exists [3]. Figure 1.1 shows a photograph of cosmic ray tacks in a cloud chamber. The picture was taken in 1932 and published in 1933. It shows a positron moving upwards through a 6 mm thick lead plate. The positron was produced by a high energy cosmic ray hitting an atom below the lead plate. When passing through the plate, the positron looses energy and its curving becomes tighter in a 1.5 T magnetic field. In 1955 and 1956 the remaining anti-particle constituents of bulk matter known at this time were experimentally discovered, namely the antiproton [4] and the antineutron [5]. Thereafter, more fundamental particles - so-called quarks - were discovered. Quarks are the fundamental constituents of matter and they also have their corresponding antiparticles, so-called antiquarks [6–8]. For instance, the proton is formed by two up quarks and one down quark and the antiproton by two anti-up quarks (also up antiquarks) and one anti-down quark (also down antiquark) respectively. The Standard Model of particle physics is the theory which describes fundamental interactions[3]. At this point I would like to refer to [11,12] where detailed information about other fundamental particles and their antiparticles can be found since they are beyond the scope of this thesis.

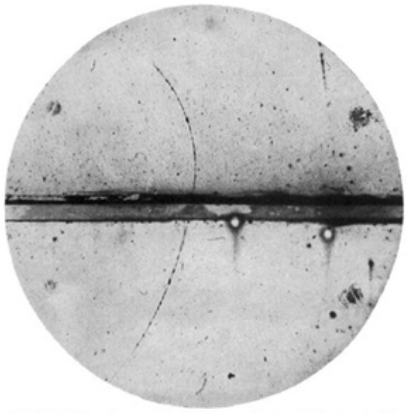

Figure 1.1.: Photograph of a positron passing through a lead plate (horizontal line) in a cloud chamber. The track is curved due to the surrounding 1.5 T magnetic field. (Reprinted from [3])

Since the discovery of antimatter scientists have developed experiments to measure its properties. Particles and antiparticles are produced in pairs when energy is converted into mass. This emergence of substance from pure energy is described in Einstein's famous

[3]Note that the Standard Model is not a complete theory of fundamental interactions since for instance it does not incorporate gravitation by means of general relativity. There are more deficiencies in the Standard Model which hints at "physics beyond the Standard Model" which is treated for instance in [9, 10].

equation

$$E^2 = (mc^2)^2 + (pc)^2, \tag{1.1}$$

which gives the energy of a massive object, with the kinetic energy (left term) when this (massive) object is moved (right term) [2]. Equation (1.1) gives the total energy of an object in motion, where m is its mass, c is the speed of light in vacuum and p is the momentum. It takes at least $2mc^2$ in order to synthesize a particle - antiparticle pair. For instance, in order to produce an antiproton, one has to provide energy[4] of at least $2 \times 0.938\ \mathrm{GeV/c^2} = 1.876\ \mathrm{GeV/c^2}$. This amount of energy is produced by accelerating protons almost to the speed of light and shooting them against a target which could be a piece of metal, where the energy contained in the protons and their kinetic energy is converted into another set of particles and antiparticles emerging from this spot. This way antiprotons are produced but they escape after conversion and annihilate by hitting surrounding matter. In order to do experiments with antiparticles, they have to be somehow contained away from matter and they have to be cooled[5].

Bruno Touschek proposed in 1960 to store and collide electrons and positrons in one storage ring [13]. Electric and magnetic fields keep the particles on their circular path in the ring and the vacuum prevents the particles from unwanted collisions. The first storage ring to store antiparticles was the "anelllo di accumulation" (ADA), which was built close to Rome. Gersh Budker proposed in the early 1960s to use electrons in order to cool protons and antiprotons by means of Coulomb scattering [14]. The idea is to load charged particles e.g antiprotons, into a storage ring and at certain positions they interact with a dense cloud of electrons (so-called electron gas). The electrons have less energy then the antiprotons and in this way the antiprotons are "slowed down" since they transfer kinetic energy to the electrons. Electron cooling was first tested in 1974 with protons at NAP-M, a storage ring in Novosibirsk [15].

In the early 1970s Simon van der Meer at CERN invented another method to cool charged particles called stochastic cooling [16]. A group of particles is often referred to as beam and this beam spreads around a central momentum since some particles are faster and others are slower. Using a high bandwidth low-noise amplifier connected to a so-called pick-up, the position and phase of the particles can be determined and the aforementioned

[4] Since $E = mc^2$, energy and mass is exchangeable. It is common in particle physics to express mass in terms of energy ($1GeV/c^2 = 1.783 \times 10^{-27}$ kg).

[5] The term cooling is often used in particle physics for deceleration and reduction of the energy spread of charged particle beams.

spread can be reduced by correcting the average position of the particles by means of a kicker [16]. Figure 1.2 shows the principle of stochastic cooling.

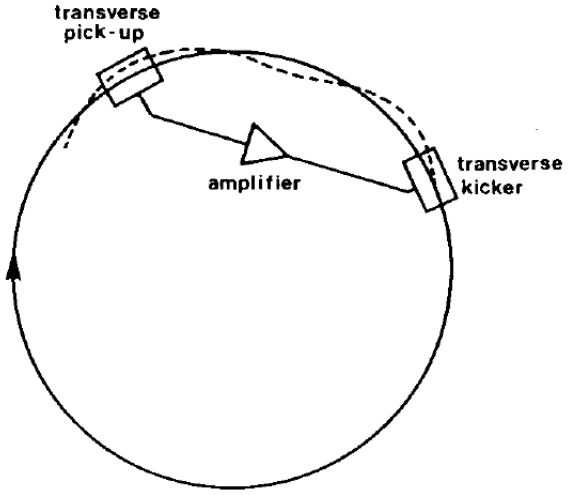

Figure 1.2.: Schematic of the principle of stochastic cooling of a particle beam (dashed line). The pick-up detects the position and phase of the particles and corrects their momentum spread with a kicker. (Reprinted from [17])

In 1975 the first proof-of-principle was carried out in the intersecting storage rings (ISR) at CERN [18] where the world's first proton-proton collisions were produced in 1971. After several successful experiments using stochastic cooling, the first antiproton accumulator (AA) was built at the end of the 1970s. Later, the AA was supplemented by a second ring, the antiproton collector (AC), which lead to the antiproton accumulator complex (AAC). The AAC produced antiprotons at CERN until 1996.

Another very important facility at this time was CERN's low energy antiproton ring (LEAR) where stochastic and electron cooling were used in a complementary manner since stochastic cooling works well for high energy beams and at lower energies electron cooling is more efficient. LEAR was assembled in 1982 and it was in this facility in 1995 that the first (hot[6]) antihydrogen atoms were produced when antiprotons collided with xenon atoms [19]. Later, parts of LEAR's functionality were replaced by the antiproton decelerator (AD) which was the result of the reuse of the AC and the removal of the AA. The AD is called the "antimatter factory" and has been in operation since the year 2000. Up to now, the AD at CERN is the only facility worldwide providing low energy antiprotons for antimatter experiments. However, the antiprotons ejected from the AD

[6]The term hot is used for energies higher than several MeV.

still have a kinetic energy of 5 MeV (∼10% of speed of light) which makes precision experiments with them impossible. Hans Dehmelt invented the so-called Penning trap[7] named after the Dutch physicist Frans Penning, who inspired Dehmelt to use a combination of magnetic and electric fields within high vacuum in order to store charged particles (see Figure 1.3). The Penning trap allowed Dehmelt to isolate single electrons [20] for high precision measurements of the electron magnetic moment and mass in the early 1970s and later on he did the same measurements with positrons [21].

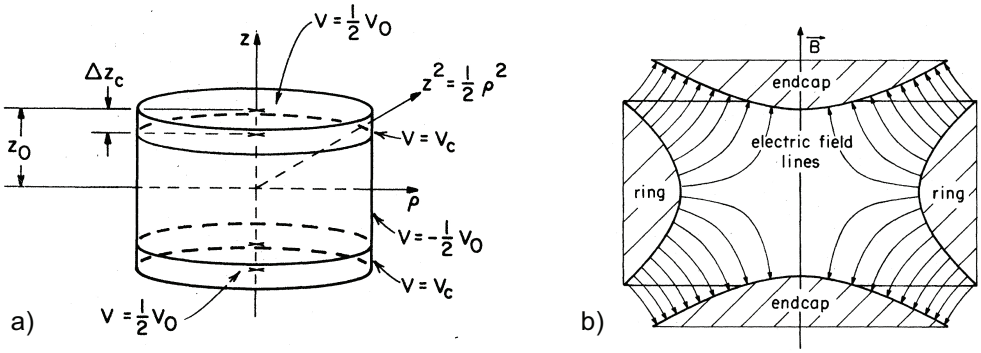

Figure 1.3.: Schematic of two common Penning trap types. a) Cylindrical Penning trap (also called Malmberg-Penning trap) with three electrodes. The field configuration is almost the same as for the parabolic Penning trap. b) Parabolic Penning trap consisting of two endcap electrodes and one ring electrode. The magnetic field **B** confines the charged particles in radial direction **z** and the static electric field forms a minimum in the center of the trap. (Figures reprinted from [22])

Combining a Penning trap and the aforementioned cooling techniques for antiprotons lead to the first trapped, cold antiprotons in 1986 [23] at the LEAR facility. The antiprotons ejected from LEAR still had a kinetic energy of 5 MeV and only the usage of so-called degrader foils[8] reduced the kinetic energy of the antiprotons so that they could be captured by rising voltages of some kV. At this point all the "ingredients" necessary for producing cold antihydrogen atoms were theoretically in place - cold antiprotons and positrons. The first low energy antihydrogen atoms were produced in 2002 by the ATHENA collaboration [24] and later the same year confirmed by the ATRAP collaboration [25] both based at CERN's AD . Thereafter, in 2005 ATHENA was disbanded and many of the former members started to work on the ALPHA experiment. In 2010 the ALPHA collaboration was successfully trapped antihydrogen atoms in a magnetic

[7]Throughout this thesis the term Penning trap is used also for the Malmberg-Penning trap.
[8]Thin metal foils in the range of some few up to several tens of μm thickness placed in the beam line toward the Penning trap.

CERN ID	Experiment Name	Comment
AD-1	ATHENA[a]	disbanded in 2004
AD-2	ATRAP[b]	TRAP experiment was the predecessor
AD-3	ASACUSA[c]	antiprotonic helium
AD-4	ACE[d]	antiprotons used for cancer therapy
AD-5	ALPHA[e]	is being upgraded to ALPHA-2
AD-6	AE$\bar{g}$IS[f]	constructed and operational since spring 2012
AD-7	GBAR[g]	planned

[a] `http://athena.web.cern.ch/athena/`
[b] `http://public.web.cern.ch/public/en/research/ATRAP-en.html`
[c] `http://asacusa.web.cern.ch/ASACUSA/`
[d] `http://public.web.cern.ch/public/en/research/ACE-en.html`
[e] `http://alpha.web.cern.ch/`
[f] `http://aegis.web.cern.ch/aegis/`
[g] `http://gbar.in2p3.fr/`

Table 1.1.: List of recent antimatter experiments at CERN.

trap [26] and demonstrated the first antimatter spectroscopy by "shining" microwaves on the trapped antihydrogen atoms in 2012 [27]. The long term goal of the ALPHA collaboration is to apply the spectroscopic techniques developed for the study of hydrogen, which is one of the most precisely studied systems in physics, to the study of antihydrogen. [28]. Antimatter provides the opportunity to test experimentally one of the foundations of the Standard Model of particle physics, the so-called CPT-theorem. The theorem states that there is a fundamental symmetry of physical laws under the simultaneous inversion of charge, parity and time (CPT). In other words, it means that there is an invariance of the behavior of a particle if the spatial coordinates are reversed (parity inversion), time flows backwards (time inversion) and the particle is replaced by its antiparticle (charge conjugation). The CPT-theory also states, that every particle type has a corresponding antiparticle type [2]. Another important application of antihydrogen is to test the currently unmeasured gravitational interaction between antimatter and matter. The following section will show how the AE$\bar{g}$IS collaboration wants to measure the effect of gravitational acceleration on antihydrogen.

For completeness' sake, Table 1.1 shows a list of recent antimatter experiments at CERN using the antiprotons ejected from the AD[9].

[9] The AD will be extended by an additional ring called extra low energy antiproton ring (ELENA) for further cooling of antiprotons. ELENA is scheduled to be operational in 2017 [29].

1.2. The AEgIS Experiment at CERN

The weak equivalence principle (WEP) is based on the universality of the free-fall which has been tested to be valid to a very high precision [30]. The WEP is one of the cornerstones of general relativity and makes no distinction between matter and antimatter particles. However, there has never been a direct verification of the WEP with antimatter. Since there are different predictions about the response of antimatter to gravitational fields [31, 32] the validity of the WEP in antimatter systems will finally be given by experimental evidence. The antimatter experiment: gravity, interferometry, spectroscopy (AEgIS) proposes to perform the first direct measurement of the gravitational interaction between matter and antimatter using an antihydrogen beam [33,34]. AEgIS' primary scientific goal is to measure the Earth's local gravitational acceleration $\bar{g}$[10] on antihydrogen with 1% relative precision. The gravity measurement will be carried out by detecting the vertical displacement of the fringe pattern produced by the antihydrogen beam traversing through a classical Moiré deflectometer by means of a position-sensitive detector [34]. Figure 1.4 shows the principle of the proposed antihydrogen ($\bar{H}$) production and the $\bar{H}$ beam formation by means of an accelerating (inhomogeneous) electric field.

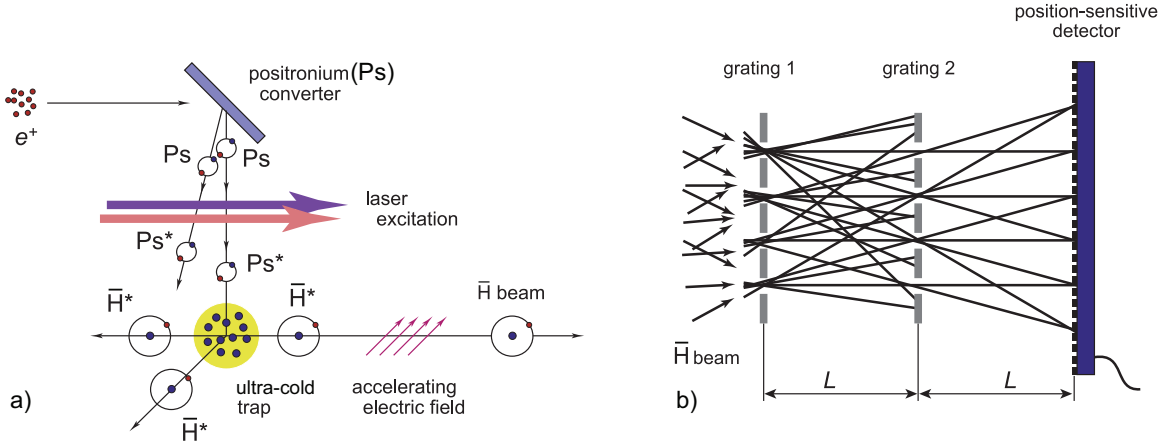

Figure 1.4.: a) Schematic of $\bar{H}$ production by laser-controlled, resonant charge exchange between excited state positronium (Ps^*) and antiprotons. b) Schematic of the Moiré deflectometer with grating distance L combined with a position-sensitive detector.

The $\bar{H}$ production takes place during a charge exchange process between excited state

[10]The gravitational acceleration is usually denoted as g, but in case of interaction between matter and antimatter it is referred to as $\bar{g}$.

positronium[11] and antiprotons [35, 36]:

$$Ps^* + \bar{p} \rightarrow \bar{H}^* + e^-. \tag{1.2}$$

Equation (1.2) shows the only $\bar{H}$ formation reaction mentioned in this thesis. A more detailed account of other $\bar{H}$ production methods can be found in [37]. Positronium is produced by bombarding a nanoporous material (Ps converter or Ps target) with an intense bunch of e^+ [38]. The Ps emerging from the target is excited to the Rydberg state by a two-step laser excitation, in order to increase the $\bar{H}$ production efficiency and to increase sensitivity to the time varying electric fields used to create the $\bar{H}$ beam [35]. Moreover, the laser excitation increases the Ps average lifetime, so that the Ps does not (self)annihilate before the collision with the antiprotons.

To perform a $\bar{g}$ measurement with 1% precision it is crucial to store antiprotons ($\bar{p}$) in a Penning trap and to cool the antiprotons to 100 mK since the temperature of the antiprotons dominates the $\bar{H}$ temperature [33]. The requirement for the ultra-cold $\bar{H}$ is motivated by the allowed vertical spread of the $\bar{H}$ beam after acceleration. To reach such low energies requires the development of new techniques to cool the antiprotons. Two promising techniques are sympathetic cooling with e^- and evaporative cooling[12]. Sympathetic cooling of $\bar{p}$'s could be realized by storing them together with e^- so that they overlap. The e^- may be coupled to an external tuned circuit in order to be resistively cooled (see section 2.1) and the cold plasma of e^- in turn could cool the $\bar{p}$ by coulomb interaction. In order not to drive (heat) the trapped particles, there is the need for a cryogenic low-noise environment. Developing low-noise electronics coupled to these trapped particles, is the main goal of this thesis.

The temperature of the Penning traps in the current AE$\bar{g}$IS apparatus is 4.2 K, but this will be lowered to 100 mK in a future upgrade by means of a dilution refrigerator [33]. Figure 1.6 shows an overview of the AE$\bar{g}$IS experimental setup at CERN. The AE$\bar{g}$IS apparatus mainly consists of the 1 T and 5 T magnets embedded in liquid helium (LHe) vessels and connected through the central region. Furthermore, liquid nitrogen (LN) vessels are surrounding the LHe container in order to provide a thermal shielding so that the heat input is decreased. Penning traps are placed inside the magnet bores in the cryogenic ultra-high vacuum, where they are thermally and mechanically anchored to

[11] Positronium (Ps) is a meta-stable exotic atom which consists of the bound state of an electron (e^-) and positron (e^+).

[12] Evaporative cooling is a method were the trapped particles are cooled by releasing the "hottest" ones by lowering the trap potential.

the LHe vessel at the base temperature of 4.2 K. About 3×10^7 $\bar{p}$'s are ejected every 100 s from the AD. After passing through degrader foils, in order to reduce the kinetic energy, about 10^5 $\bar{p}$'s are trapped in the catching trap. The catching trap is housed in the 5 T magnet bore and contains high-voltage (HV) electrodes where a trapping potential up to 9 kV is applied[13]. Afterwards, the stored $\bar{p}$'s are transferred further down stream through transfer traps into the ultra-cold trap in the 1 T magnet. It in this trap, the $\bar{p}$s have to be stored and cooled in order to produce cold $\bar{H}$ atoms in the next step. Note that the tuned circuit (described in Section 4.1) is connected to the ultra-cold trap and the cryogenic amplifier (described in Chapter 6) is thermally anchored to the trap support. About 10^8 e^+ are produced[14] and collected in a Surko-type positron accumulator. The positrons are transferred into the 1 T magnet in front of the the double stack trap at the place of the sectorized electrode (see Figure 1.5). This sectorized electrode is used to invoke a radial displacement of the positrons [39] in order to store them in the off-axis trap. The final step for the $\bar{H}$ production is to accelerate the positrons towards the porous target where the conversion from positrons into positronium (Ps) takes place. The Ps is then laser excited and diffuses down to the cold $\bar{p}$s and the $\bar{H}$ formation is triggered (see Figure 1.4).

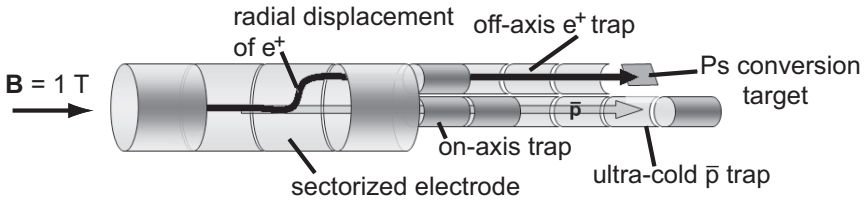

Figure 1.5.: Schematic of the trap system placed in the 1 T magnet used for the $\bar{H}$ production.

At this point, the voltage applied to the ultra-cold trap is switched in order to give a (non-linear) accelerating electric field, so that the $\bar{H}$ atoms are "shot" towards the Moiré deflectometer.

[13]The high voltage electrodes are specified up to 20 kV but so far antiprotons were caught at 9 kV.
[14]The positrons are produced by a so-called positron-emitter sodium-22 (^{22}Na) where positrons are released by a radioactive decay.

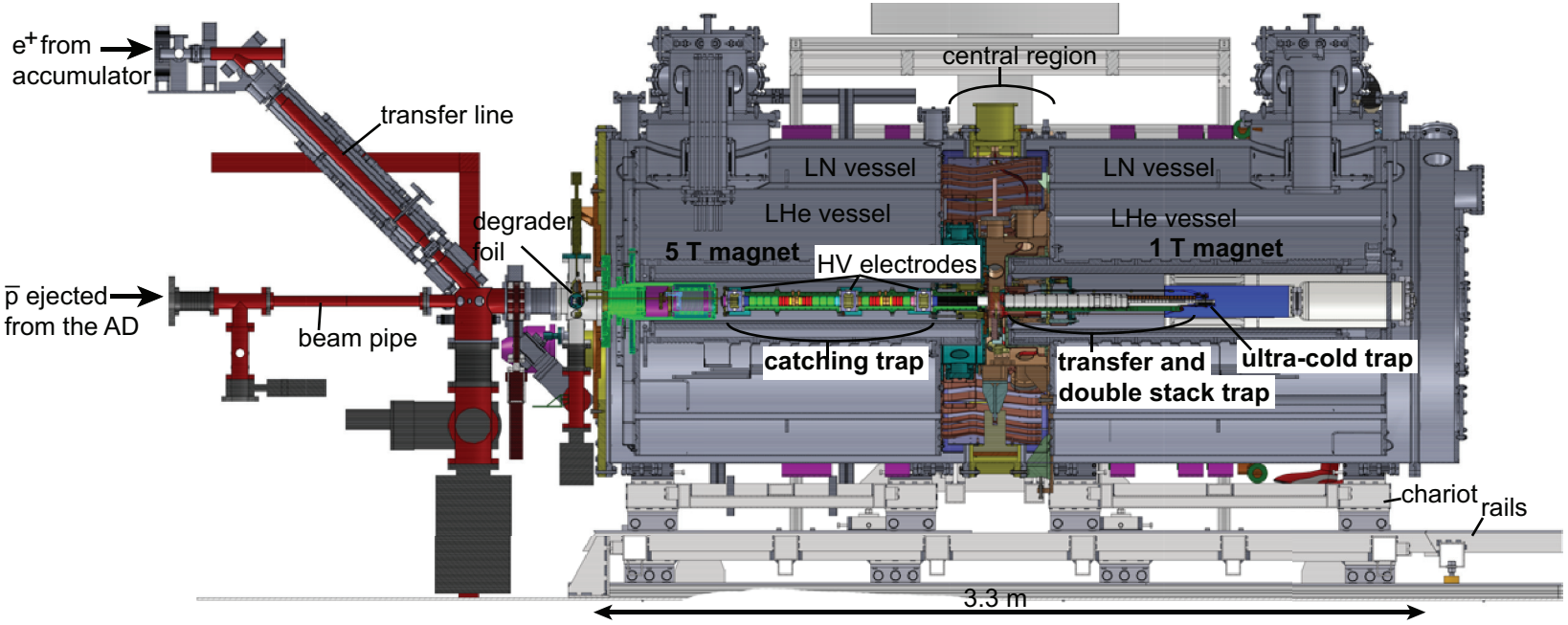

Figure 1.6.: Cross-sectional view of the AEḡIS apparatus consisting of the 5 T and 1 T magnets connected through the central region, the transfer line for e^+ coming from the e^+ accumulator (not shown) and the $\bar{p}$ beam pipe connected to the AD. The whole setup rests on a chariot (wheeled vehicle) which allows to move both magnets independently in horizontal direction on rails. Note that this overview represents the status of the experimental setup in fall 2012 and the Moiré deflectometer with the position-sensitive detector is not shown.

2. Theoretical Basics

2.1. Charged Particles in a Penning Trap

Charged particles can be spatially confined in a stable manner by the superposition of a homogeneous magnetic field **B** in axial direction and a perpendicular electrostatic field **E**. This special field configuration was named "Penning trap" by Hans Dehmelt who received the Nobel Prize for his development of the ion trap technique. Dehmelt was inspired by Frans Penning who refined techniques in order to keep electrons longer in a discharge tube [22]. A charged particle with charge q and velocity $\mathbf{v}$ is pinned to a magnetic field line by means of the Lorenz-force $\mathbf{F} = q(\mathbf{E} + \mathbf{v} \times \mathbf{B})$. This leads to a circular orbit perpendicular to the magnetic field resulting in the cyclotron motion oscillating with the free cyclotron frequency ω_c given by

$$\omega_c = \frac{q}{m}|\mathbf{B}|. \tag{2.1}$$

for a particle with mass m and charge q. The cyclotron motion is small in radius and high in frequency [22]. Due to the electrostatic potential well the stored particle bounces back and forth along the magnetic field (z direction) with the axial frequency ω_z given by

$$\omega_z = \sqrt{\frac{2qdV_0}{m}}. \tag{2.2}$$

V_0 is the amplitude of the trapping potential and d a constant related to the specific trap geometry and is called effective electrode distance. This equation shows that the axial frequency of a trapped particle can be varied by "shaping" the potential well (V_0). The axial frequency of electrons is about $\sim$ 20 MHz for a potential of about 1 kV. Since Protons are much heavier than electrons, their axial frequency for the same V_0 is

$\sim$ 500 kHz. The third eigenmotion of a trapped, charged particle is a slow $\mathbf{E} \times \mathbf{B}$-drift called magnetron oscillation with the magnetron frequency ω_- calculated by

$$\omega_- = \frac{1}{2}\left(\omega_c - \sqrt{\omega_c^2 - \omega_z^2}\right). \tag{2.3}$$

.

Since the magnetron motion interacts with the cyclotron motion, the net result is the so-called modified cyclotron motion with frequency ω_+ given by

$$\omega_+ = \frac{1}{2}\left(\omega_c + \sqrt{\omega_c^2 - \omega_z^2}\right). \tag{2.4}$$

.

Figure 2.1 shows the three superimposed motions of particles in a Penning trap and their respective angular eigenfrequencies.

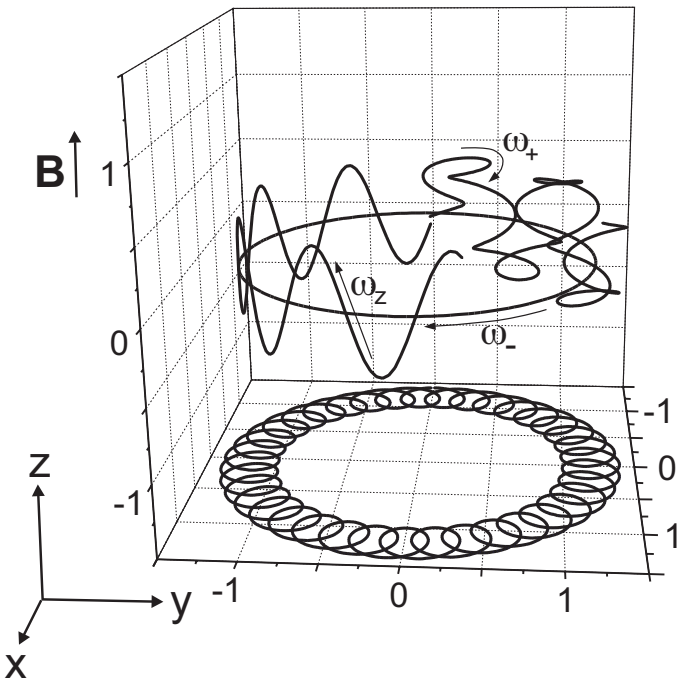

Figure 2.1.: Cartoon of the motion of charged, trapped particles and the projection to the xy plane. (Adapted from [40])

Furthermore, there is an invariance theorem that states

$$\omega_c^2 = \omega_+^2 + \omega_z^2 + \omega_-^2 \tag{2.5}$$

and a frequency hierarchy $\omega_+ \gg \omega_z \gg \omega_-$ [22].

2.2. Smith Chart - A brief Introduction

When it comes to high frequency signals it is meaningful to define electrical quantities as traveling waves rather than static currents and voltages. For this purpose the reflection coefficient $\mathbf{\Gamma}$ is defined as the ratio of the electrical field strength of the reflected wave divided by the forward traveling wave. Another definition for $\mathbf{\Gamma}$ is

$$\mathbf{\Gamma} = \frac{\mathbf{Z} - Z_0}{\mathbf{Z} + Z_0} \tag{2.6}$$

with $\mathbf{Z} = R + jX$ being a general complex impedance and Z_0 as the characteristic impedance (i.e. 50 Ω). For a one-port the reflection coefficient $\mathbf{\Gamma}$ is equal to the scattering parameter (S-parameter) $\mathbf{S}_{11}$. Phillip Smith invented the smith chart as a graphical representation of $\mathbf{\Gamma}$ in order to help to solve problems involving radio frequency (RF) circuits and transmission lines [41]. The smith chart is a bilinear Moebius transformation which is mapping the complex impedance plane ($\mathbf{Z}$-plane) to the complex $\mathbf{\Gamma}$-plane (see Figure 2.2).

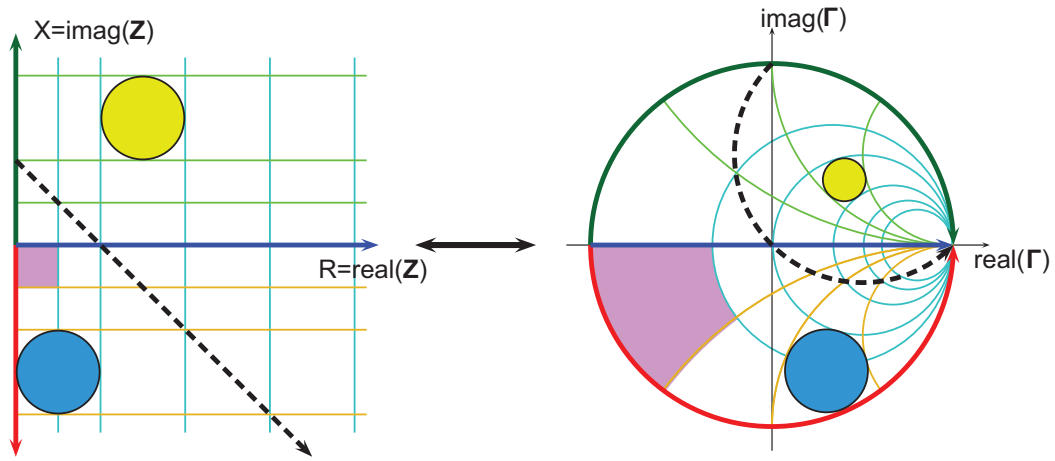

Figure 2.2.: Illustration of the bilinear Moebius transformation of basic shapes from $\mathbf{Z}$-plane to $\mathbf{\Gamma}$-plane. (Adapted from [42])

2.3. Parallel Tuned Circuit and the Quality Factor

Since the terms loaded and unloaded quality factor (Q-factor) are often mixed up with each other it is worthwhile to define these quantities at this point and to show some interesting aspects which make measurements easier. Figure 2.3 shows the equivalent circuit for a parallel tuned circuit. The resistor R_p represents loss mechanisms and is no existing hardware component.

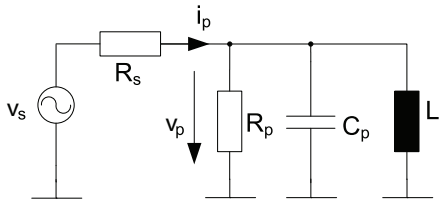

Figure 2.3.: Equivalent electrical circuit of a RLC parallel tuned circuit.

Assuming an ideal signal source ($R_s \to \infty$), the impedance $\mathbf{Z}$ of the equivalent circuit is calculated by

$$\mathbf{Z}(\omega) = \frac{1}{{R_p}^{-1} + j\omega C_p + (j\omega L)^{-1}} \tag{2.7}$$

and its trace is depicted in Figure 2.4. In the complex $\mathbf{Z}$-plane the tuned circuit creates a circle starting in the so-called detuned short position ($\nu = 0$ and $\nu \to \infty$). Resonance occurs when the inductive and capacitive reactance (X_L and X_C) tune each other out $X_L = \omega L = X_C = (\omega C_\mathrm{p})^{-1}$ at the resonance frequency $\nu_0 = \omega_0/(2\pi) = (2\pi\sqrt{LC_p})^{-1}$.

In addition to the resonance frequency the quality factor is a figure of merit of tuned circuits and is calculated by

$$Q = \frac{\nu_0}{\nu^+_{-3dB} - \nu^-_{-3dB}} = \frac{\nu_0}{\Delta\nu} \tag{2.8}$$

where the difference $\nu^+_{-3dB} - \nu^-_{-3dB}$ represents the 3 dB bandwidth which is equivalent to the drop in signal level by a factor of $1/\sqrt{2}$.

There are three different quality factor defined for a tuned circuit [42]:

- Q_0 or unloaded Q: Q-factor of the unperturbed system (i.e. a stand alone resonator)

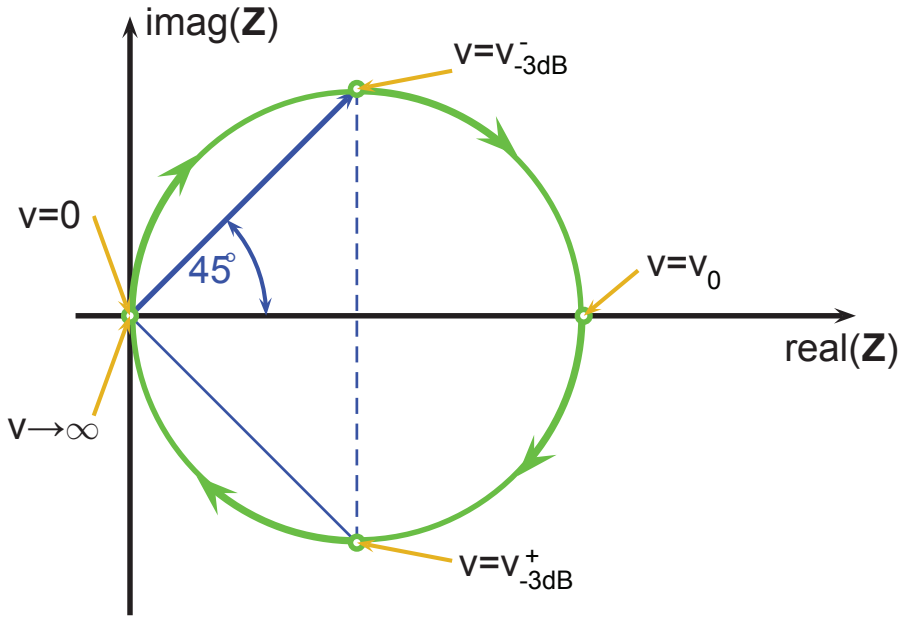

Figure 2.4.: Trace of the parallel tuned circuit in the complex impedance plane. (Adapted from [42])

- Q_L or loaded Q: Q-factor of the resonator when connected to a source (generator) and/or measurement device
- Q_{ext} or external Q: Q-factor that describes the degeneration of the unperturbed resonant circuit when connecting peripheral components (e.g. generator)

The three Q-factors are connected in a parallel manner by

$$Q_L = \frac{1}{Q_0^{-1} + Q_{ext}^{-1}}. \tag{2.9}$$

The coupling coefficient κ is defined by the unloaded Q divided by the external Q ($\kappa = Q_0/Q_{ext}$). Figure 2.5 illustrates the graphical representation of the Q-factor definitions in the Smith chart. This schematic could represent a real measurement result displayed on a network analyzer and one could easily measure the figure of merit of the tuned circuit with markers positioned at the dedicated frequencies. The Q-factor definitions and the corresponding points in the Smith chart are summarized in Table 2.1. Note that the measurement of Q_{ext} and Q_0 is performed in the complex $\mathbf{Z}$-plane and Q_L in contrast is measured in the $\mathbf{\Gamma}$-plane (equivalent to $\mathbf{S}_{11}$ for a one-port).

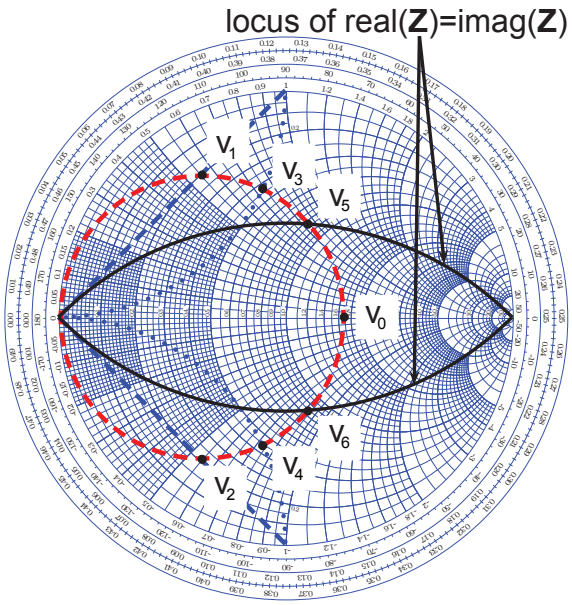

Figure 2.5.: Frequency points in order to determine the Q-factors of a tuned circuit represented in the Smith chart. Note that in case of measuring ν_5, ν_6 to determine Q_0 and ν_3, ν_4 to determine Q_{ext} the data has to represented in the complex $\mathbf{Z}$-plane and for ν_1, ν_2 the data has to be put to the complex $\mathbf{\Gamma}$-plane. (Adapted from [42]).

definition	symbol	condition	corresponding frequencies in Figure 2.5
unloaded Q	Q_0	$real(\mathbf{Z}) = imag(\mathbf{Z})$	ν_5 and ν_6
loaded Q	Q_L	$max(\lvert imag(\mathbf{S}_{11})\rvert)$	ν_1 and ν_2
external Q	Q_{ext}	$\mathbf{Z}/Z_0 = \pm j$	ν_3 and ν_4

Table 2.1.: Summary of Q-factor definitions and their representation in the Smith chart.

3. Cryogenic Filter

Since the AEgIS experiment consists of a cryogenic vacuum environment nested in a high magnetic field, special care has been taken in designing electronic circuits. In order to provide low-noise DC biasing of the Penning trap electrodes , every connected cable has to be low-pass filtered. There is a trade-off between removing as much noise as possible (very low cut-off frequency) and having the possibility to change the electrode potential in short time (high cut-off frequency). For instance, the axial frequency of the trapped particles is dependent on the applied potential. In order to change this parameter within a reasonable time span, the time constant of the electrode bias network[1] should not be larger than 1 ms, which gives in turn the cut-off frequency of 1 kHz.
All electronic components mentioned in this section are surface mounted technology (SMT) devices due to spatial constraints inside the 1 T region of the AEgIS apparatus. Furthermore, when it comes to cryogenic electronics, special care has to be taken when choosing the devices.

3.1. Behaviour of Electronic Components at Cryogenic Temperatures and General Considerations

Generally speaking it is better to use low dielectric constant (low-K) capacitors like NP0/C0G ceramic dielectric capacitors than high-K ones such as BX, X7R and Z5U. Low-K material does not change capacitance significantly at cryogenic temperatures [43–45]. For resistors it is advised to use thin film devices rather than thick film ones and metal film if possible [43]. In some cases where the properties of thick film resistors are appreciated, for instance because of high voltage rating, then the low temperature behavior has to be evaluated. Usually thick film resistors show significant increase of resistance around and below a temperature of 4.2 K [43, 46]. Due to this fact they can even be used as low temperature thermometers [47]. Since cryogenic systems are in general very inaccessible

[1] Gemma Testera, private communication

the reliability of systems operated in such an environment is tremendously important. This leads to another important design rule for cryogenic electronics, which is to use redundancy, if there is space, in order to increase reliability.

3.2. Cryogenic Low-Pass Filter

For the AE$\bar{g}$IS experiment filtering of the cables connected to the recombination trap is crucial. Since any noise pick up could drive the trapped particles, all lines for biasing and signal routing connected to the trap need to be low-pass filtered.

3.2.1. Filter Type and Component Selection

Usually low-pass filters with low cut-off frequencies incorporate inductors with ferrite beads in order to increase the inductance. Such low-pass filters are called LC (inductor-capacitor) filters and show higher filter performance than RC (resistor-capacitor) filters. However, ferrite materials lose their permittivity in high magnetic fields and the inductance is basically the same as the inductance of an air coil. Air coils need to be physically large in order to obtain large inductance values (see chapter 4.1). As described in section 1.2, the cryogenic electronics are operated in a 1 T magnetic field, thus ferrite cores are not an option. Furthermore, the LC combination in bias networks may cause filter performance degradation due to resonance effects.
An additional difficulty is that standard 0603 chip resistors have voltage ratings up to 150 V maximum due to degradation caused by high internal electric fields [48]. This voltage limitation is too low since the electrode bias voltages may be raised up to 200 V and/or fast pulses for $\bar{H}$ acceleration or trap clearing pulses with amplitudes up to 200 V may be applied. Thus there is the need for special high voltage rated chip resistors. A new type of thick film resistors produced by Ohmcraft (a division of Micropen Technologies Corporation) has reduced internal electric fields due to higher trace spacing and thus much higher voltage rating than common chip resistors [48]. The key technology is to implement narrow lines (fine lines) and narrower spacing by means of high speed precision direct write deposition [48]. Table 3.1 outlines the voltage rating improvements for different chip packages.

The high voltage chip resistors are available as HVC series from Ohmcraft and chosen to build a RC low-pass filter. These thick film HVC resistors are typically made of ruthenium dioxide (RuO_2) mixed with powders of glass [49]. Ruthenium dioxide is

chip size	trace dimensions [mils]		voltage rating [V]	
	conventional	fine line	conventional	fine line
0502	15 x 30	4 x 120	30	300
0603	25 x 40	4 x 160	40	400
0805	40 x 50	4 x 240	50	600
1206	50 x 100	4 x 1000	100	1000
2512	50 x 230	4 x 2600	100	2500

Table 3.1.: Overview of Ohmcraft voltage rating improvements for different EIA chip sizes (data taken from [48]). The trace dimensions are in thousands of an inch (1 mil = 25.4 µm).

known to change its electrical resistance significantly [50], which has to be considered in the filter design. References [50, 51] show that RuO_2 thick film resistors increase their resistance value from room temperature to 4.2 K by a factor of two. Chip capacitors in 0603 packages are commonly available with voltage ratings up to 250 V which is high enough for our purposes. If there is in the future the need for higher electrode bias voltages beyond 250 V, there are special high voltage capacitors with NP0 dielectric available from Johanson Dielectrics with 0805 capacitors up to 1 kV [52].

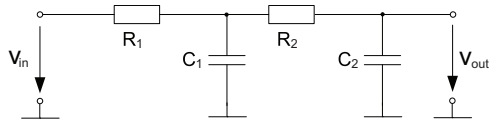

Figure 3.1.: Schematic of second order low-pass filter.

The general transfer function $G(s)$ of a passive second order RC low-pass filter is

$$\frac{V_{\mathrm{out}}(s)}{V_{\mathrm{in}}(s)} =: G(s) = \frac{1}{(1 + s\mathrm{R}_1\mathrm{C}_1)(1 + s\mathrm{R}_2\mathrm{C}_2)}, \tag{3.1}$$

where $s = j\omega$ in order to obtain the transfer function as a function of frequency. Typically the resistance times the capacitance is called time constant $\tau = \mathrm{RC}$ and is linked to the corner frequency by $\omega_c = 1/(2\pi\tau)$. Calculating the absolute value of the transfer function leads to

$$|G(j\omega)| = \sqrt{\frac{1}{(1 + \omega^2 {R_1}^2 {C_1}^2)(1 + \omega^2 {R_2}^2 {C_2}^2)}}. \tag{3.2}$$

3.2.2. Filter Design and Layout

The low-pass filter is directly attached to the Penning trap electrodes which means that the corner frequency should not be too low in order to apply voltage changes within a reasonable time. As mentioned at the beginning of this chapter, a good choice for the time constant of the bias network connected to the ultra-cold trap in the 1 T region is about 1 ms. Hence, the corner frequency ν_c (see Figure 3.6) is set to 1 kHz (angular frequency $\omega_c = 2\pi\nu_c$) and is calculated by

$$\nu_c = \frac{1}{2\pi\sqrt{R_1 R_2 C_1 C_2}} \xrightarrow[C_1=C_2=C]{R_1=R_2=R} \frac{1}{2\pi RC}. \tag{3.3}$$

Note that the corner frequency of the second order low-pass filter is the same as for a first order low-pass filter. Since the second order filter shows steeper fall off after the corner frequency ν_c, the -3 dB cutoff frequency has to be corrected for higher order filters by

$$\nu_{\text{cutoff},-3\text{dB}} = \nu_c\sqrt{2^{\frac{1}{n}} - 1} \tag{3.4}$$

where n denotes the filter order.
The 0603 NP0 capacitor with a voltage rating of 250 V is commercially available with a capacitance of at most 100 pF. Plugging the capacitor value of 100 pF into equation (3.3) for the corner frequency of a second order low-pass filter under the assumption that $R_1 = R_2$ and $C_1 = C_2$, gives a resistance value of $R_1 = R_2 = 1592\,\text{k}\Omega$. As mentioned at the beginning of this chapter, it is advised to use redundant electronic designs in cryogenic environments. In case of the low-pass filter the choice is to implement every component twice in parallel. Furthermore, due to the fact that the RuO_2 thick film resistors double their electrical resistance when cooled from 290 K down to 4.2 K, the effect of putting resistors in parallel is compensated, and the change of the capacitance value over the temperature is negligible. This leads to a final theoretical value for the resistors R_1 and R_2 of 796 kΩ for a corner frequency of 1 kHz and 200 pF capacitance.

However, the chosen resistance is 681 kΩ with 0.5% tolerance (Ohmcraft product identification HVC0603E6813DT) because these resistors were available as samples for prototyping. Plugging the resistor value into equation (3.3) gives a theoretical corner frequency of 1.168 kHz at 4.2 K temperature.

The final filter design is shown in Figure 3.2. The filter PCB layout for two low-pass filters on one board is depicted in Figure 3.3.

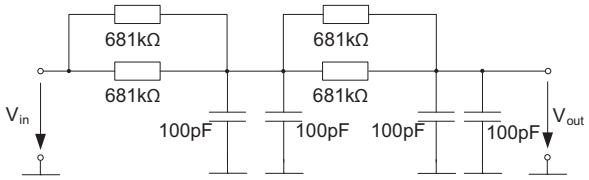

Figure 3.2.: Schematic of the final low-pass filter design.

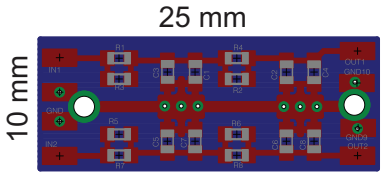

Figure 3.3.: PCB layout of the final low-pass filter design.

3.2.3. Cryogenic Low-Pass Filter Performance Measurement

The first value to verify was the estimate that the 681 kΩ RuO_2 thick film resistor doubles its electrical resistance when cooled from 290 K to 4.2 K. For this purpose the filter PCB shown in Figure 3.2 was assembled with two 681 kΩ in series in order to obtain a closed electrical circuit (compare R_1 and R_2 in Figure 3.1). The PCB was directly cooled by the convection of helium gas in a cryostat. The result of the resistance measurement from room temperature (index 290 K) to 4.2 K is summarized in Table 3.2. The theoretical value for R_1 and R_2 in series is (1362 ±6.81) kΩ at room temperature.

The measured resistance values are in good agreement with the results presented in [50,51] for thick film RuO_2 resistors at cryogenic temperatures. Using the measured increase of the resistance and updating the corner frequency at 4.2 K temperature gives 1.025 kHz.

The filter performance was measured by means of a high impedance vector network analyzer (VNA) Agilent E5061B. Usually the filter transfer characteristics would be measured using a 50 Ω measurement environment. Since the designed filter has more than 1 MΩ impedance this would lead to an immeasurable voltage drop on a 50 Ω input impedance due to the given voltage divider. The network analyzer E5061B has an input impedance of 1 MΩ and can measure signals from 5 Hz to 30 MHz [53]. Figure 3.4 shows

temperature [K]	$R_1 + R_2$ [kΩ]	$(R_1 + R_2)/(R_{1,290K} + R_{2,290K})$
290.0	1361	1.00
12.0	1578	1.16
10.0	1616	1.19
8.0	1690	1.24
6.0	2310	1.70
5.1	2750	2.02
4.9	2846	2.09
4.7	2938	2.16
4.6	2993	2.20
4.5	3037	2.23
4.4	3069	2.25
4.3	3098	2.27
4.2	3104	2.28

Table 3.2.: Summary of resistance measurement of Ohmcraft 681 kΩ RuO_2 resistors (HVC0603E6813DT) as a function of temperature.

the measurement setup and the schematic for the filter transfer function measurement. For this purpose the filter is housed in a metal box and connected via SMA sockets soldered onto it. The ground (GND) connection is realized with two screws. The VNA is running in T/R (transmit/receive) mode in order to measure directly the transfer function of the filter. This is done by using the input T and R as high impedance probes while the output LF OUT is providing the filter input signal (V_{in}). In order to obtain accurate and flat transfer function measurements the signal path has to be thru (transmission) calibrated.

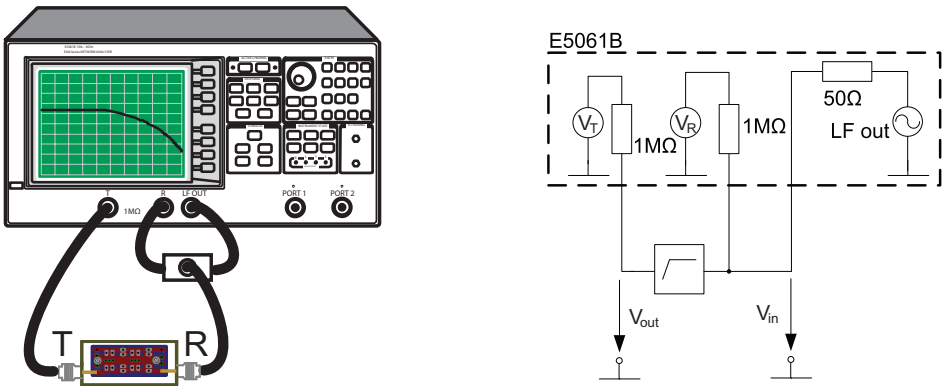

Figure 3.4.: (left) Measurement setup for Network Analyzer in T/R mode. (right) Schematic for filter transfer function measurement with Network Analyzer.

Figure 3.5 shows the measured transfer function (T/R traces) for 290 K and 4.2 K

temperature. Note the offset of more than −8 dB at 4.2 K (and about −4.5 dB at 290 K) temperature is produced by the resistive divider 681 kΩ × 2.28 = 1.552 MΩ (filter impedance between input and output) and 1 MΩ (network analyzer input impedance; compare Figure 3.4). The theoretical value for the offset at 4.2 K is calculated by 1 MΩ/(1 MΩ + 1.552 MΩ) = 0.392 in linear terms and 20 log(0.392) = −8.14 dB on a logarithmic scale. The ripple between 10 and 100 Hz is an artifact of the VNA calibration.

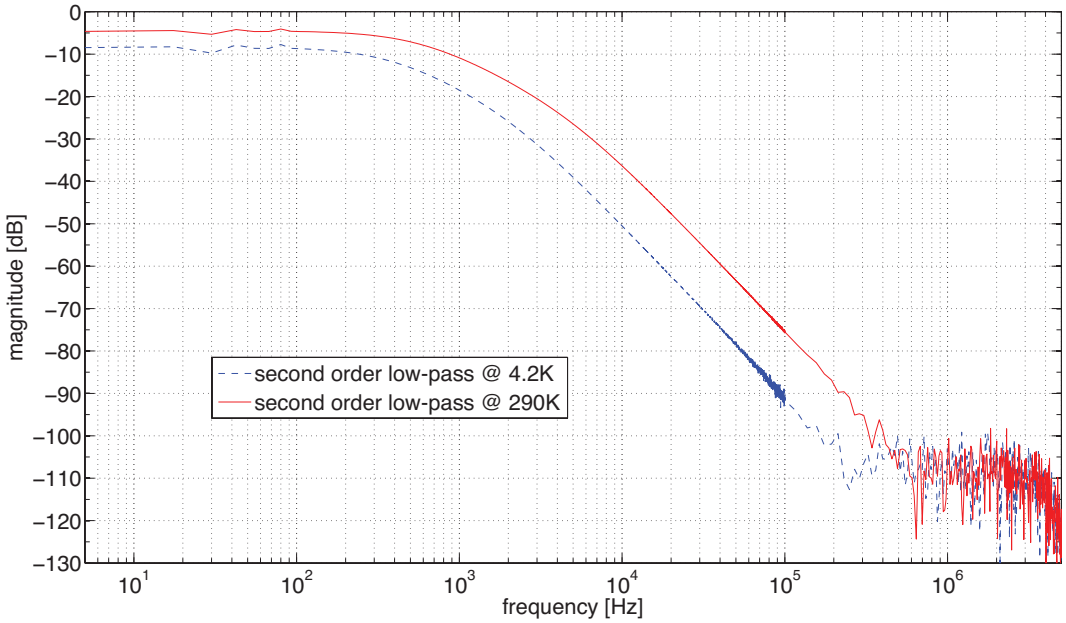

Figure 3.5.: Measured transfer function of the second order low-pass filter at 290 K and 4.2 K temperature.

The offset corrected transfer function as well as the comparison to the theoretical filter curve is illustrated in Figure 3.6. The extrapolated lines are meant to guide the eye to the corner frequencies.

Note that the slope of −40 dB/decade is in perfect agreement with the theory [54]. Table 3.3 summarizes the corner frequency values. The reason for the discrepancy between the theoretical and the measured values is caused by the measurement setup, including the VNA input impedance of 1 MΩ/30 pF [53] and the used coaxial cables. The reader is referred to chapter A.3 for more details on the measurement setup and the filter simulation. The following section describes how the low-pass filter is modified in order to bypass fast voltage pulses or sinusoidal signals.

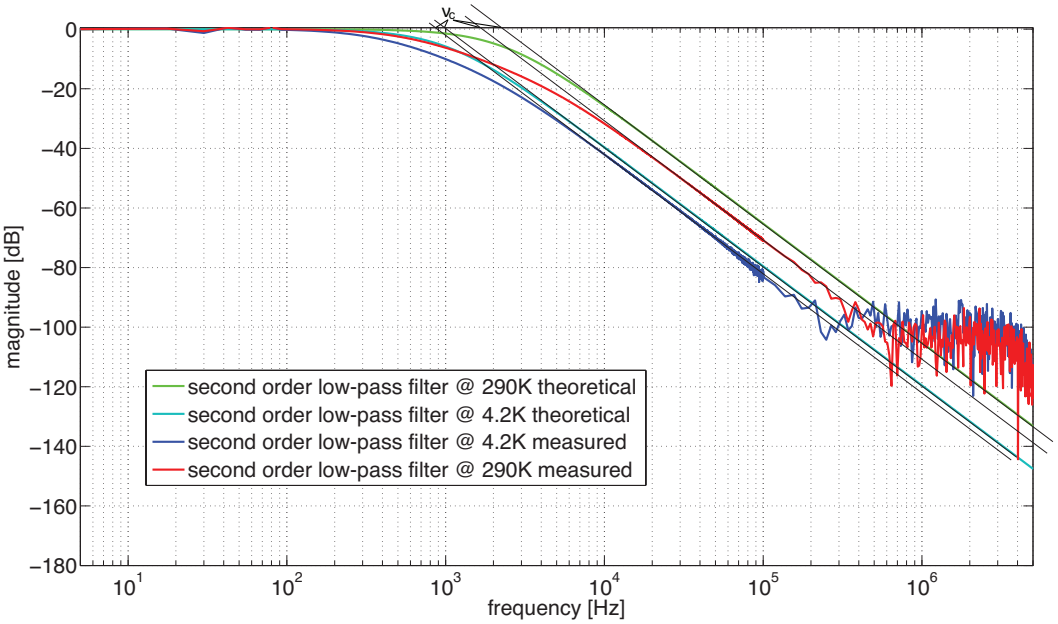

Figure 3.6.: Offset corrected transfer function of the second order low-pass filter at 290 K and 4.2 K temperature shown with theoretical filter curves.

temperature [K]	theorectical ν_c [Hz]	measured ν_c [Hz]
290.0	2337	1667
4.2	1025	867

Table 3.3.: Summary of the characteristic values of the second order low-pass filter.

3.3. Cryogenic Amplitude Dependent Low-Pass Filter

In chapter 2.1 it was mentioned that particles stored in a trap may be manipulated by externally applied electric signals. In general these signals are either fast pulses or of sinusoidal waveform. However, in either case these signals would be rejected by the low-pass filter described in section 3.2.2. In order to overcome this limitation, Schottky diodes in parallel with the low-pass filter (see Figure 3.7) can be used to bypass signals that have a larger amplitude than the threshold voltage of the diodes. These filters are commercially available by Stahl-Electronics [55] for instance, but they were not used since a different filter specification is needed for the AE$\bar{g}$IS experiment. Since diodes exhibit nonlinear current versus voltage behavior or in general nonlinear transfer behavior (see Figure 3.13), the amplitude dependent filter utilizing diodes is also called a nonlinear

filter.

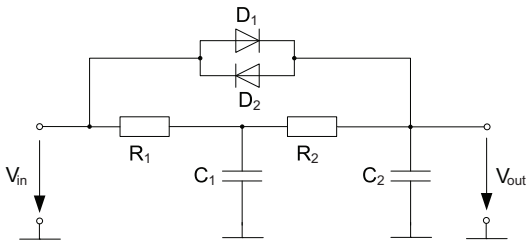

Figure 3.7.: Schematic of the nonlinear low-pass filter design without redundancy.

3.3.1. Component Selection

The low-pass filter design and its components are identical to the one shown in section 3.2.2. The selection of the Schottky diode is done by minimizing its impact on the low-pass filter performance. Usually special semiconductors with a small band gap [56] are chosen for operation at cryogenic temperatures. One of the most common semiconductors for cryogenic electronics is gallium arsenide (GaAs) since it does not suffer from the carrier freeze-out effect like silicon (Si) does [56]. There are GaAs Schottky diodes available, like DGS 20-015A and GS8DI25104 from IXYS company. These devices may work very well at temperatures below 10 K, but their junction capacitance is very large (of the order of 4 to 10 pF at negative biasing voltages of more than 100 V; for details see [57,58]). Since the diodes' junction capacitance is in parallel with the low-pass filter it tremendously reduces its performance by bypassing it permanently. This effect gets even worse at higher frequencies. Thus, the choice of the diode is limited to devices with a small junction capacitance. Fortunately, Si Schottky diodes exhibit very low junction capacitance values of $<$2 pF at zero bias voltage like, for example, the the Infineon BAS70 [59]. The freeze-out of Si below 30 K is not an issue in this case since the device is passive and an increase of the resistance due to reduced charge carrier density does not influence the diode behavior in a negative way. In other words, the Si diode works at 4.2 K temperature.
Another important diode parameter is the maximum forward current, which is 70 mA for the BAS70. The load current i_c for a 200 V pulse with a rise time of about 100 ns into a Penning trap capacitance C_{trap} of 20 pF is approximately given by

$$i_c = \frac{dv}{dt} C_{\mathrm{trap}} \approx 40\,\mathrm{mA}, \tag{3.5}$$

where dv/dt denotes the change of voltage with time. Thus, the Si Schottky diode BAS70 is suitable for the purpose of bypassing the low-pass filter.

3.3.2. Filter Design and Layout

In order to increase reliability by redundancy, the Schottky diodes are implemented threefold which reduces the forward current for each diode and to have more leeway for upcoming more demanding requirements. In this section a pair of Schottky diodes is referred to as one diode since they have to appear for the purpose of bypassing in pairs. The schematic of the nonlinear filter design is shown in Figure 3.8, its PCB layout in Figure 3.9 and Figure 3.10 shows a photograph of the populated filter PCB bolted into a shielded box with two and three diodes.

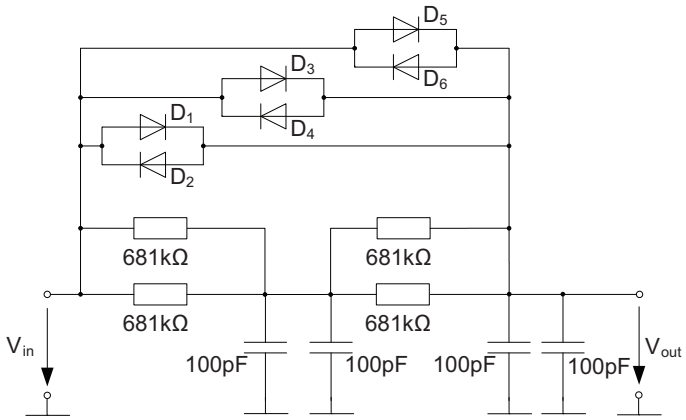

Figure 3.8.: Schematic of the nonlinear low-pass filter design.

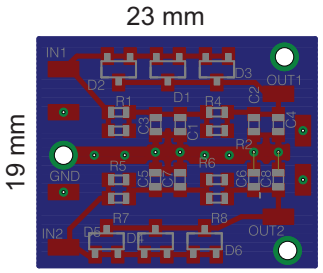

Figure 3.9.: PCB layout for the nonlinear low-pass filter.

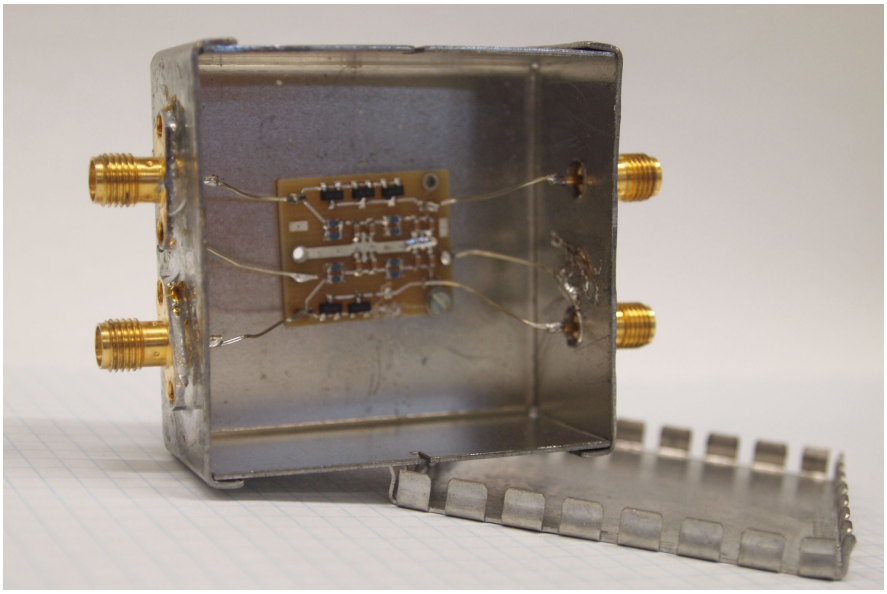

Figure 3.10.: Photograph of the filter PCB mounted in a shielding box.

3.3.3. Filter Performance Measurement

The nonlinear low-pass filter is again housed in a metal box and the transfer function is measured as already described in section 3.2.3. Since the diodes should not bypass any signal for this measurement, the LF OUT source power (see Figure 3.4) was set to −20 dBm (=10 µW). Figure 3.11 shows the nonlinear low-pass filter transfer function at 290 K and 4.2 K temperature with two and three diodes for bypassing. For comparison, the transfer function of the low-pass filter is inserted in the same figure to show the performance degradation in detail. The filter transfer function shows a minimum and then converges to a constant value. This feature is caused by the diode capacitance in parallel to the low-pass.

Table 3.4 summarizes the nonlinear filter performance. While at 290 K one additional diode reduces the filter performance by about 10.8 dB, at 4.2 K the gap is only 3.5 dB. Moreover, the nonlinear filter performance with two diodes is closer to the normal second order low-pass one (see Figure 3.11).

Since the current overhead with two diodes is large enough for a Penning trap with 20 pF capacitance and the nonlinear filter performance is much better than with three diodes, the two diode design is chosen for the experiment.

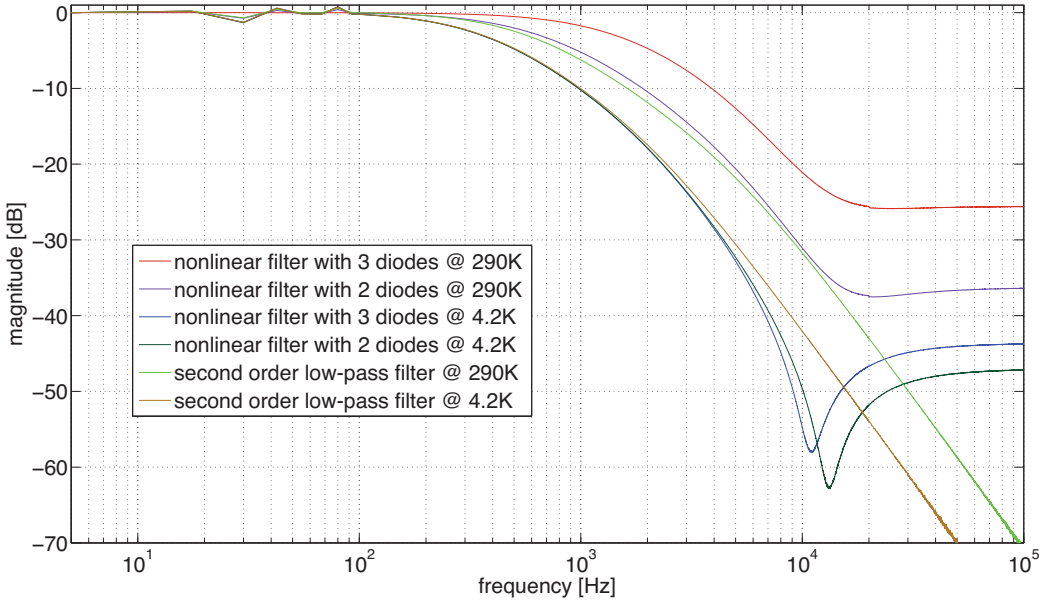

Figure 3.11.: Normalized transfer function of the nonlinear low-pass filter and the second order low-pass filter for comparison.

	magnitude at 100kHz	
temperature [K]	2 diodes [dB]	3 diodes [dB]
290.0	−36.4	−25.6
4.2	−47.2	−43.7

Table 3.4.: Summary of the measured characteristic values of the nonlinear filter.

Another interesting aspect of the nonlinear filter is the bypassing performance in the time domain. For this purpose a signal generator is attached to the filter input and an oscilloscope with 1 MΩ input impedance at the filter output. Figure 3.14 shows the electrical measurement setup. The test signal is a sine wave V_{sig} with 1 MHz frequency and the peak-to-peak amplitude ($V_{\mathrm{in,pp}}$) is swept. Note that for this measurement no pulser was used.

The result of the input voltage sweep versus output voltage measurement is shown in Figure 3.13. The threshold voltage of the diode BAS70 is shifted towards higher voltages upon cooling to 4.2 K temperature which gives higher suppression of spurious signals with amplitudes up to 100 $\mathrm{mV_{pp}}$.

Figure 3.14 shows the filter output signal at 290 K and 4.2 K temperature for a voltage pulse of 20 V amplitude, 400 ns pulse width and 5 ns rise and fall time. The plot depicts

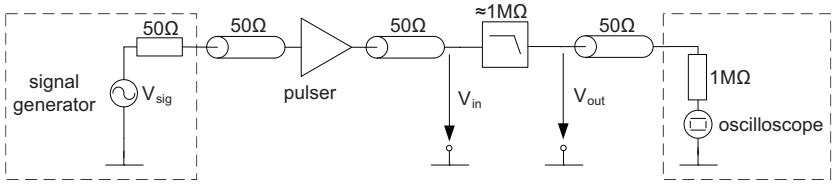

Figure 3.12.: Measurement setup for filter performance measurement in time domain.

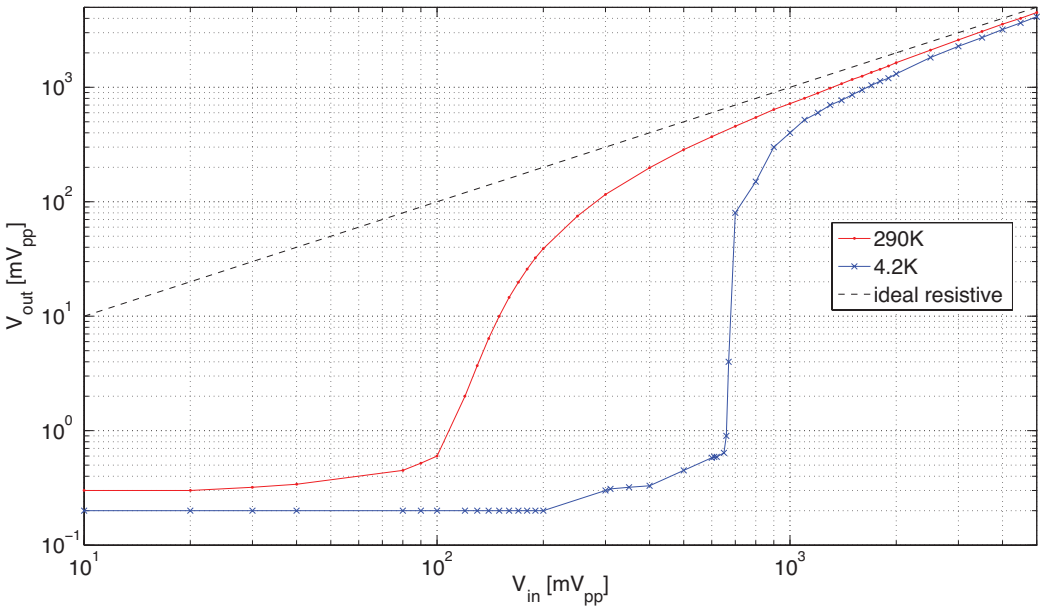

Figure 3.13.: Input voltage sweep versus output voltage for 1MHz sine wave signal.

an average over 50 pulses taken with a repetition rate of 100 Hz. The ripple on the data is due to mismatches in the signal chain, especially between cable and oscilloscope as well as cables and filter (see Figure 3.14). The filter impedance is quoted as approximately 1 MΩ in Figure 3.12 since the resistive part is about 681 kΩ at room temperature and about 1.5 MΩ at 4.2 K. A pulser was used in order to amplify the signal generator output signal to an amplitude of 20 V. Table 3.5 summarizes the rise and fall time measurement results for the nonlinear filter with 2 and 3 diodes. The 20% to 80% rise and fall time definition are chosen in order to reduce the influence of the ripples. The pulse rise and fall time is degraded by the nonlinear filter, but both quantities are significantly well below the specified maximum of 100 ns. Note that there is practically no difference between the timing behavior of the nonlinear filter with two diodes at 290 K and 4.2 K.

condition	temperature [K]	rise time [ns]	fall time [ns]
without filter	290.0	28	30
2 diodes	290.0	67	45
2 diodes	4.2	66	44
3 diodes	290.0	65	59
3 diodes	4.2	65	59

Table 3.5.: Summary of the rise and fall time measurement of the nonlinear filter.

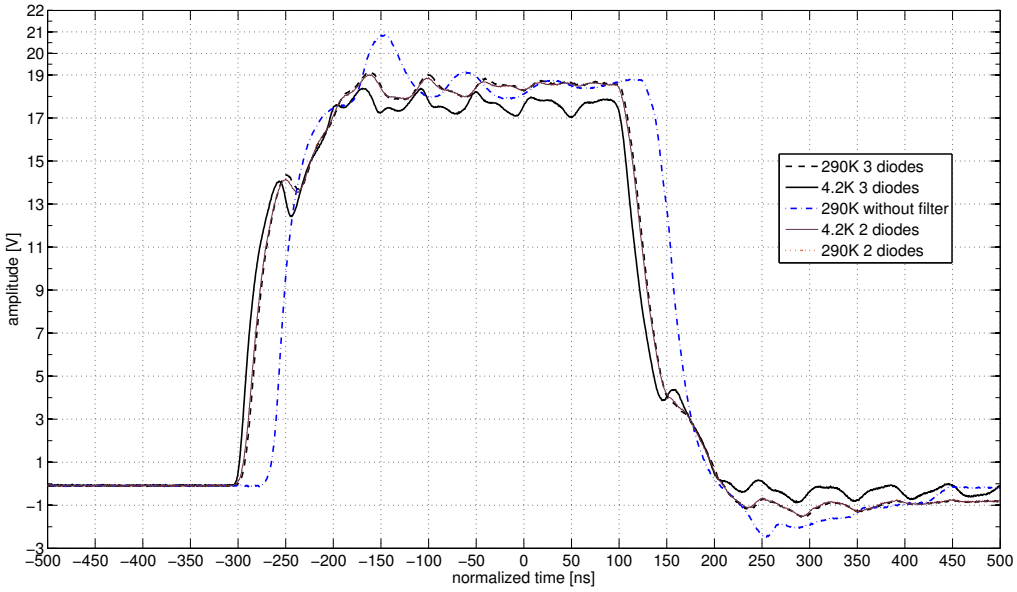

Figure 3.14.: Pulse response of the nonlinear filter for different conditions.

4. Design and Construction of a Tuned Circuit

Tuned circuits connected to a Penning/ion trap may be used to obtain information about the particles confined in the trap. The most important advantages of using a tuned circuit are:

- Narrow bandwidth of noise coming from connected devices.
- High impedance values at relatively high frequencies are possible.
- Trapped particles are strongly coupled to the environment within a narrow bandwidth only.
- Parasitic trap capacitance is tuned out.

A tuned circuit is in general realized as an inductor (L), which gives an RLC parallel resonant circuit. The R component is referred to as effective resistance R_p, and C (here C_p) is denoted as parallel capacitance. Usually C is a parasitic capacitance and should be reduced. Often a tuned circuit connected to the electrodes of a Penning trap is referred to as a tank circuit. The tuned circuit and a simplified cylindrical Penning trap with three stacked electrodes are shown in Figure 4.1. As already described in chapter 2.1, one of the three eigenmodes of trapped particles is the axial motion along the magnetic field (**B**-field).

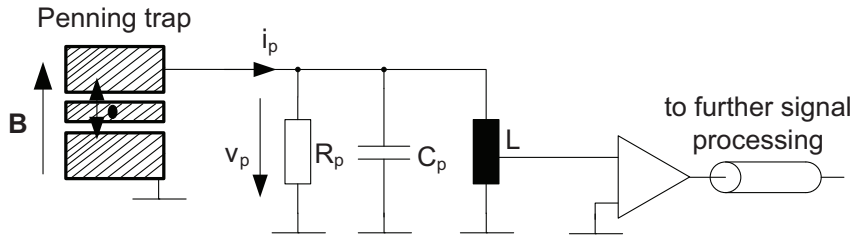

Figure 4.1.: Simplified schematic of the axial detection system with a cylindrical Penning trap.

These particles are confined, moving charges which induce mirror charges on the trap electrodes. The conducting electrodes of the Penning trap can be represented by a parallel-plate capacitor in a simplified manner [60]. A single charged particle between this parallel-plate capacitor induces a current

$$i_p = \frac{qv_z}{d}, \tag{4.1}$$

where q is the particle's charge, v_z stands for the particle's velocity perpendicular to the capacitor plates and d is the separation of the capacitor plates. In general, i_p is a tiny quantity which depends on the trap geometry and the number and charge of the stored particles. However, this induced current i_p produces a voltage drop v_p across the RLC circuit, which is calculated by

$$v_p = i_p R_p = i_p \omega_0 L Q_L \tag{4.2}$$

in this case the particles' axial frequency ω_z and the detector resonance frequency $\omega_0 = 2\pi\nu_0 = 2\pi(LC_p)^{-1}$ are identical. In order to maximize the voltage drop and to obtain high sensitivity, one has to increase the system's loaded quality factor Q_L by means of reducing losses since the Q-factor is defined as the ratio of stored energy to energy loss per cycle. The reader is referred to section 2.3 for details on Q-factor definition.

The differential equations describing ions bound in a Penning trap are identical to an LC circuit (l_p and c_p) [60]. Figure 4.2 shows the equivalent circuit for harmonically bound ions in an ideal Penning trap, where the Penning trap itself (compare Figure 4.1) is represented as a parallel-plate capacitor. The voltage noise source e_{th,R_p} represents the thermal noise of the effective parallel resistor R_p.

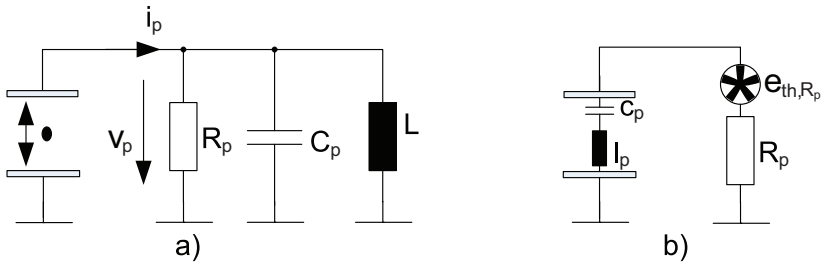

Figure 4.2.: a) Penning trap represented as parallel-plate capacitor with confined ion. b) Equivalent LC circuit for the trapped particle(s) at resonance. Note that R_p in b) is ideal (noiseless).

The detection principle is based on the shorting of the resonant system's thermal noise spectrum in case of matching resonance between resonator and trapped particles ($\nu_0 = \nu_z$). This shorting of the detector's noise spectrum is also referred to as "particle-dip" or "noise-dip". Figure 4.3 shows examples for such noise spectra for different numbers of trapped particles. Without particles stored in the Penning trap, the noise spectrum exhibits a Lorentzian shape. Already a single confined particle shorts the noise spectrum [61]. The separation of the two newly created maxima is a function of the number of particles n stored in the trap. For few particles the separation of the peaks is directly proportional to the number of particles stored in the trap [62]. Thus, the use of a detection system gives information about the number of the stored particles and whether they are in thermal equilibrium with the ambient temperature.

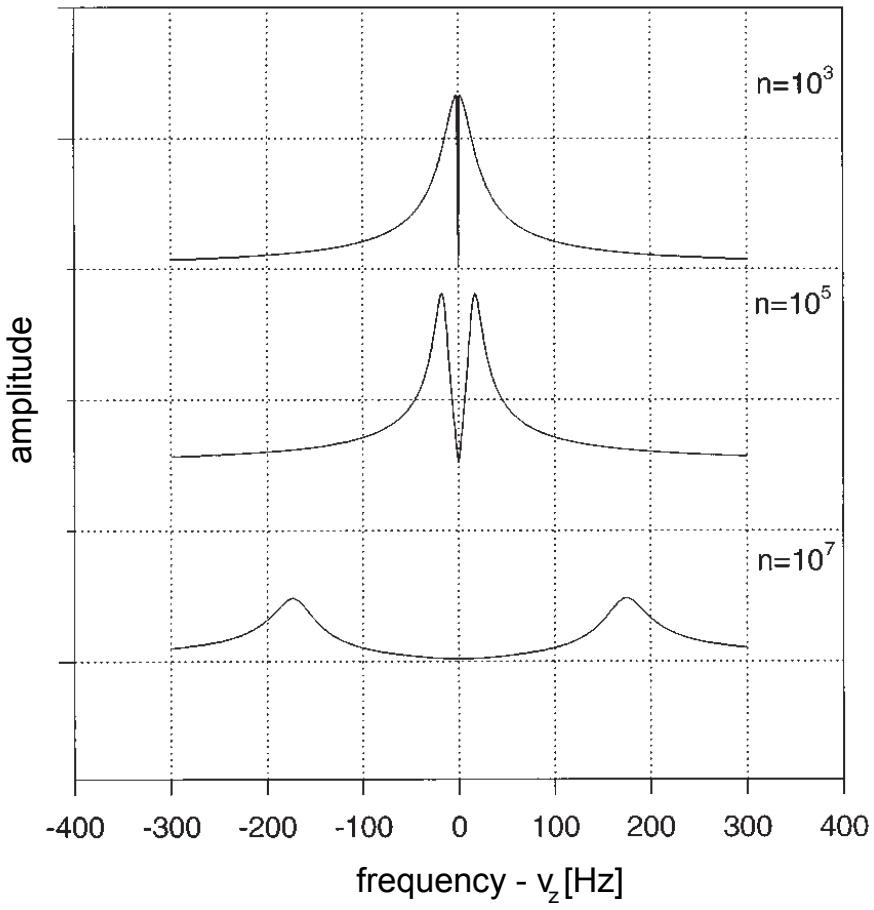

Figure 4.3.: Shorted noise spectra for different particle numbers n. The x-axis is normalized to the particle's axial frequency ν_z. (Adapted from [62])

In addition to detecting trapped particles, a high-Q detection system performs so-called resistive cooling on them. The ions' kinetic energy E_{kin} is dissipated in the tuned circuit effective parallel resistance R_p by means of $P_{\text{diss}} = i_p^2 R_p$. The damping is proportional to the velocity of the ion motion, and the energy in this mode decays exponentially by [63]

$$E_{\text{kin}} = E_0 e^{-\gamma t} \text{ with } \gamma = \frac{q^2}{m}\frac{R_p}{d^2}, \tag{4.3}$$

where E_0 stands for the initial energy before cooling, γ is the cooling time constant, d denotes the effective Penning trap diameter, m the ion mass and q the ion charge.

At low temperatures a dense cloud of charged particles will form a plasma with the Debye length λ_D and the interparticle spacing ${n_0}^{-1/3}$ which is much smaller than the size of the plasma [64]. The Debye length gives the scale over which charged particles screen out an external electric field and is calculated by

$$\lambda_D = \sqrt{\frac{\epsilon_0 kT}{q^2 n_0}} \tag{4.4}$$

where q is the particle charge and T its temperature, n_0 stands for the particle density, ϵ_0 is the vacuum permittivity and k is the Boltzmann constant. In a Penning trap such a non-neutral plasma has a spheroidal shape (see Figure 4.4) and it performs oscillating motions which are called plasma modes. The observation of these plasma modes is used as a nondestructive method for obtaining information on the plasma density and shape (aspect ratio) [65].

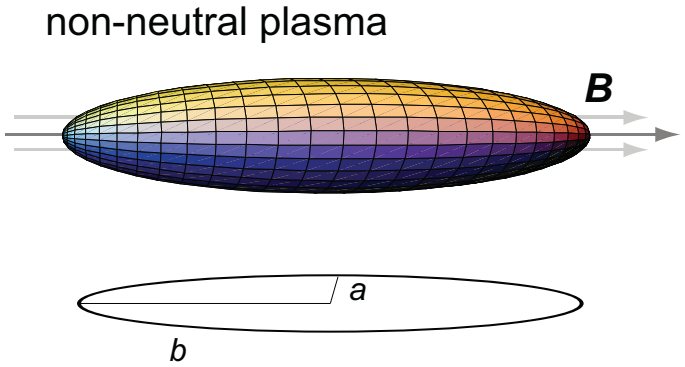

Figure 4.4.: Schematic of an ion cloud and its spatial dimension (aspect ratio $\alpha = b/a$). (Reprinted from [66])

4.1. Resonator with Superconducting Coil

The resonator specification for AEḡIS for detection and cooling are: a resonance frequency 20 MHz, a loaded quality factor Q_L larger than 2000 and a trap capacitance C_T of about[1] 20 pF. These values already give the coils' inductance $L \approx 3\mu H$ and thus its ideal geometry for a high Q-factor (high-Q), since

$$\frac{b}{d} \approx 1.5,\ B \approx b + \frac{D}{2},\ Q_0 \approx 2D\sqrt{\nu_0} \text{ and } \frac{d}{D} \approx 0.55, \tag{4.5}$$

where D is the diameter of the resonator (inner shield diameter) and B the inner shield length, d the inner coil diameter and b the coil length. The geometric dimensions are in mm and the resonance frequency ν_0 is given in MHz. The rule of thumb equations for an ideal high-Q helical resonator are taken from [67]. These equations were empirically developed for a single-layer copper coils, housed in a copper shield and supported by means of a low-loss material. Figure 4.5 shows a sketch of a helical resonator.

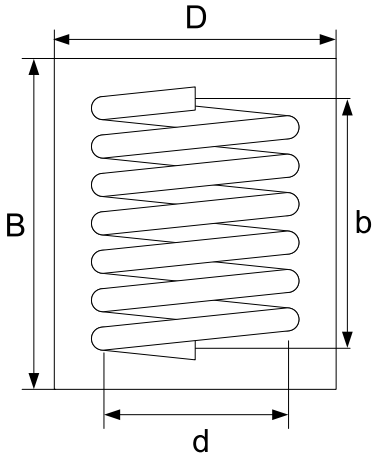

Figure 4.5.: Outline sketch of a helical resonator.

In order to show why it is meaningful to use superconducting (SC) wire for the helical resonator, the aforementioned values ($Q_0 = 2000$ and $\nu_0 = 20$ MHz) are plugged into equation (4.6) and an inner shield diameter $D \approx 227$ mm is obtained. The resonator Q-factor is clearly a geometrical factor and the larger the resonator, the larger its Q-factor. Moreover, it is not feasible to increase the resonator's parallel resistance by means of a ferrite core since the resonator will be embedded in a 1T magnetic field. In such an

[1] Gemma Testera, private communication

environment a ferrite core would saturate, and the coil's inductance would be too large in order to maintain a resonance frequency of 20 MHz. The ultra-cold region of the AE$\bar{g}$IS experiment is very limited in space. For that reason the coil inner diameter was chosen as $d \approx 10$ mm. Table 4.1 summarizes the design parameters of the superconducting helical resonator. The design rule of $d/D \approx 0.55$ was modified to 0.5 in order to allow for more space for the coil cabling inside the shield.

The number n of turns needed in order to obtain an inductance of 3 µH is about 24, when using the equation for air coils taken from [68]:

$$L[\mu\mathrm{H}] = \frac{\pi^2 n^2 d^2}{b + 0.45d} 10^{-4}. \tag{4.6}$$

Since a metallic shield is used to complete the resonator, the effective resonator inductance is reduced due to the mutual inductance of the shield, which is expressed as a correction term [69]:

$$L_{\mathrm{eff}}[\mu\mathrm{H}] = \frac{\pi^2 n^2 d^2}{b + 0.45d} 10^{-4} \left(1 - \left(\frac{d}{D}\right)^3\right) \left(1 - \left(\frac{b}{2B}\right)^2\right). \tag{4.7}$$

The effective inductance is about 20% smaller than the theoretical inductance of an air coil, thus the number of turns has to be increased to about 29 in order to obtain the specified inductance of 3 µH.

parameter	value
inductance	$\approx 3\mu$H
resonance frequency	20 MHz
trap capacitance to tune out	20 pF
coil inner diameter	10 mm
coil length	≈ 15 mm
coil turns	≈ 29
shield inner diameter	20 mm
shield inner length	26.5 mm

Table 4.1.: Summary of resonator's design parameters.

There are other groups [61–63,70,71] who have developed tuned circuits with high quality factors in order to incorporate them into a cryogenic detection system. Unfortunately none of them matches in size, resonance frequency and material used for a direct comparison. Some of them are made of copper wire since it is believed that there is no

higher Q-factor achievable when using a superconducting (SC) wire [70]. This opinion is motivated by the fact that the increased surface resistance of a type II superconductor, e.g. niobium-titanium (NbTi), will not allow higher Q-values than using a highly pure copper wire with a high residual resistivity ratio (RRR = $\rho(4.2\,\mathrm{K})/\rho(300\,\mathrm{K})$; ρ stands for the electrical conductivity) value. The surface resistance of NbTi is a function of temperature, frequency and magnetic field [70], and it is not clear from the literature which material could lead to an increased Q-factor at higher frequencies. However, in order to reduce the size of the resonator, a polytetrafluoroethylene (PTFE) insulated NbTi wire with a metal diameter of 250 µm (GVLZ012 from GVL Cryoengineering company) was chosen. PTFE (brand name teflon) is a very useful material for a resonator due to its very small dielectric loss tangent $\tan(\delta) \approx 10^{-6}$ at 4.2 K and 90 MHz [72]. Furthermore, teflon is machinable and cheap. That is why every non-metal part of the resonator like the coil body was made out of teflon. However, the amount of teflon used in a resonator has to be minimized since it has been shown that dielectric losses scale with the teflon volume [73].

Figure 4.6 shows the exploded view of the resonator with the shield and the bottom made of oxygen free (OFE) copper. The screw connecting the coil to the copper support at the bottom and the coil body are made of teflon. Note that the connection wires and the SMA socket are not shown. Furthermore four screws are needed to complete the resonator by screwing the copper can to the support. A photograph of the resonator is shown in Figure 4.7. The copper shield was polished in order to reduce surface roughness and remove impurities. The NbTi wire is fixed with a PTFE adhesive tape since the wire is quite stiff and it would be almost impossible form a coil without fixing the wire additionally.

4.2. Characterization of the Superconducting Resonator

Since the tuned circuit has to be evaluated at 4.2 K temperature, the measurements necessary for the characterization of the superconducting resonator were conducted in a liquid-helium cryostat. The sketch in Figure 4.8 shows the cryogenic measurement setup to obtain the characteristic values of the resonator. Note that the network analyzer Agilent E8358A is coupled capacitively to the resonator by means of a low-loss coupling capacitor (Johanson Technology) $C_c = 0.2$ pF and that there is only one cable connected since the measurement is done in reflection mode. Details of the cryogenic measurement setup are shown in section A.1.1.

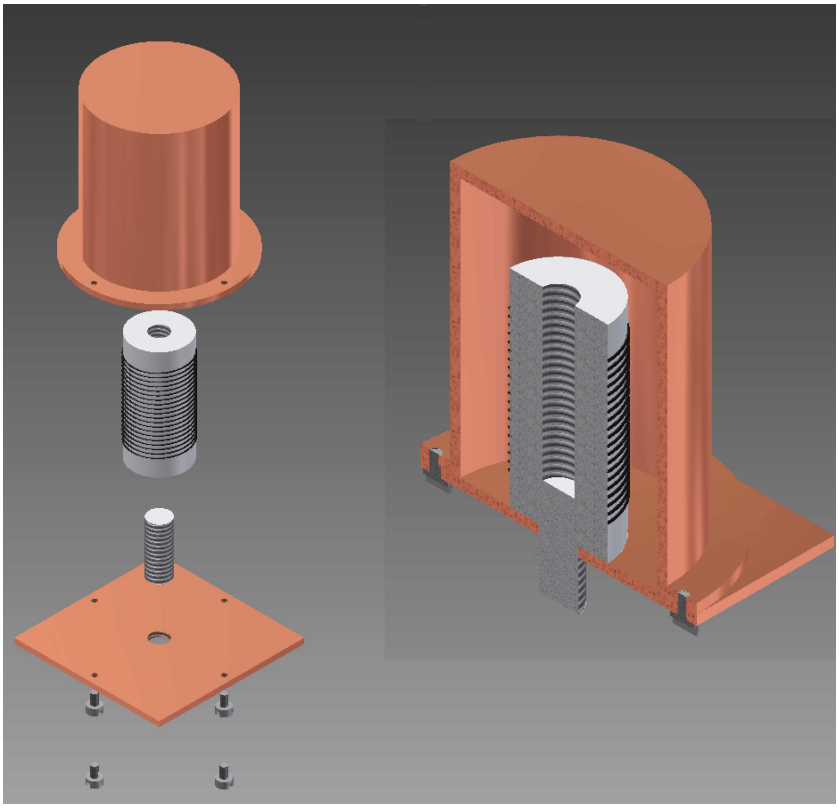

Figure 4.6.: Exploded (left) and cross-sectional view (right) of the resonator with copper shield.

In this way, the network analyzer reads the complex reflection coefficient $\mathbf{\Gamma}$ of the connected device, and its complex impedance is calculated by $\mathbf{\Gamma} = (\mathbf{Z} - Z_0)/(\mathbf{Z} + Z_0)$. The measurement system has a characteristic impedance $Z_0 = 50\,\Omega$ thus the complex impedance $\mathbf{Z}$ can be deduced and all three Q-factors are obtained as described in chapter 2.3. In order to measure the unknown coil inductance L and its self-capacitance C_s the resonator was operated at its self-resonance ν_s and then tuned to $\nu_0 \approx 20$ MHz by means of a known parallel capacitance C_p. Thus, the two equations

$$\nu_s = \frac{1}{2\pi\sqrt{LC_s}} \quad \text{and} \quad \nu_0 = \frac{1}{2\pi\sqrt{L(C_s + C_p)}} \tag{4.8}$$

with the two unknown values L and C_s can be solved by

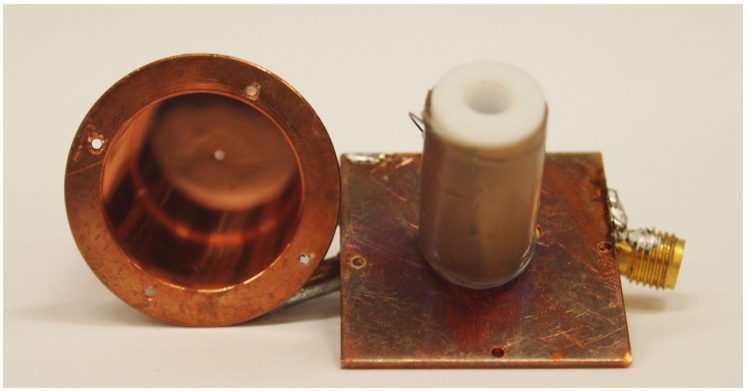

Figure 4.7.: Photograph of the resonator with copper shield.

$$L = \left(\left(\frac{1}{2\pi\nu_0} \right)^2 - \left(\frac{1}{2\pi\nu_s} \right)^2 \right) \frac{1}{C_p} \text{ and } C_s = \frac{C_p}{\left(\frac{\nu_s}{\nu_p} \right)^2 - 1}. \tag{4.9}$$

After having characterized the resonator, the Q-factors were measured. Note that there is not only the advantage of having only one measurement cable when characterizing the resonator by means of reflection measurement, it also allows to measure the loaded and unloaded Q (Q_L and Q_0) at the same time. The alternative would be to measure either the loaded Q or unloaded Q in transfer mode by using two measurement cables. Moreover, the coupling capacitance C_c would have to be changed for either measurement, which is quite time consuming since the device under test (DUT) is placed in a 4.2 K environment. For the reflection measurement and the calculation of the Q-factors the following measurement protocol was applied:

1. Calibrate the whole signal path of the cryogenic measurement setup including cables, feedthroughs and connectors at room temperature.

2. Measure the complex reflection coefficient $\mathbf{\Gamma}$ and represent the data as complex impedance $\mathbf{Z}$ with the DUT connected at 4.2 K.

3. Correct the positive offset due to reduced loss, thus normalize the measured trace to 0 dB. In the Smith chart this normalization is equal to the shrinkage of the circular trace in order not to exceed the chart which is impossible for passive devices.

4. Rotate the $\mathbf{Z}$ trace by Φ to the detuned short position. Note that this operation is not an electrical delay but a rotation by means of $\mathbf{Z}_{rot} = \mathbf{Z}e^{j\Phi}$ since an electrical delay changes the parametrization of the $\mathbf{Z}$ trace.

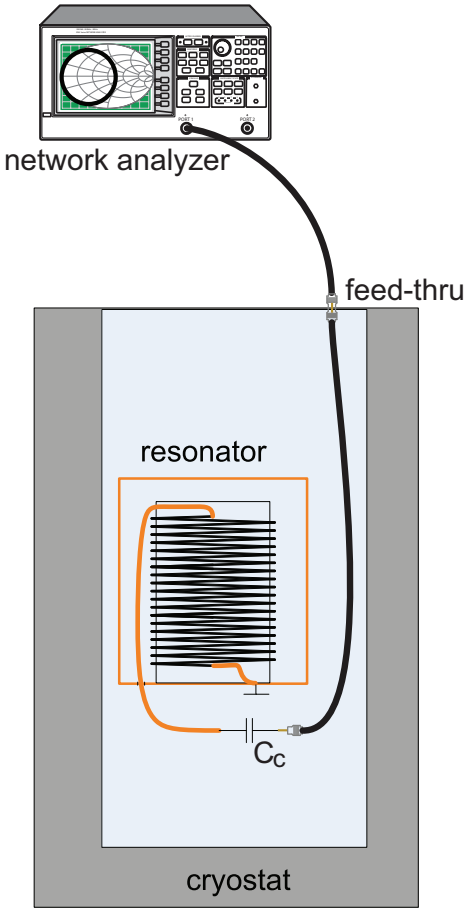

Figure 4.8.: Sketch of the cryogenic measurement setup to obtain the resonator's characteristics. Note that support structures are not indicated.

5. Identify the frequencies points that satisfy the conditions shown in Table 2.1 to obtain Q_0 and Q_L.

The measurement protocol was implemented in Matlab (MathWorks) and verified with synthetic data generated with Advanced Design System (ADS) from Agilent (see section A.4 for details). Figure 4.9 shows the result of the amplitude normalization step 3 in the Smith chart and the magnitude mapped on linear frequency axis normalized to resonance frequency ν_0. Note that the amplitude is normalized so that it would reach 0 dB asymptotically.

The trace of $\mathbf{Z}$, rotated to the detuned short position in the Smith chart, as well as its real and imaginary part are shown in Figure 4.10. At the two points where the difference between real($|\mathbf{Z}|$) and imag($|\mathbf{Z}|$) equals zero, the condition for unloaded Q_0 is given.

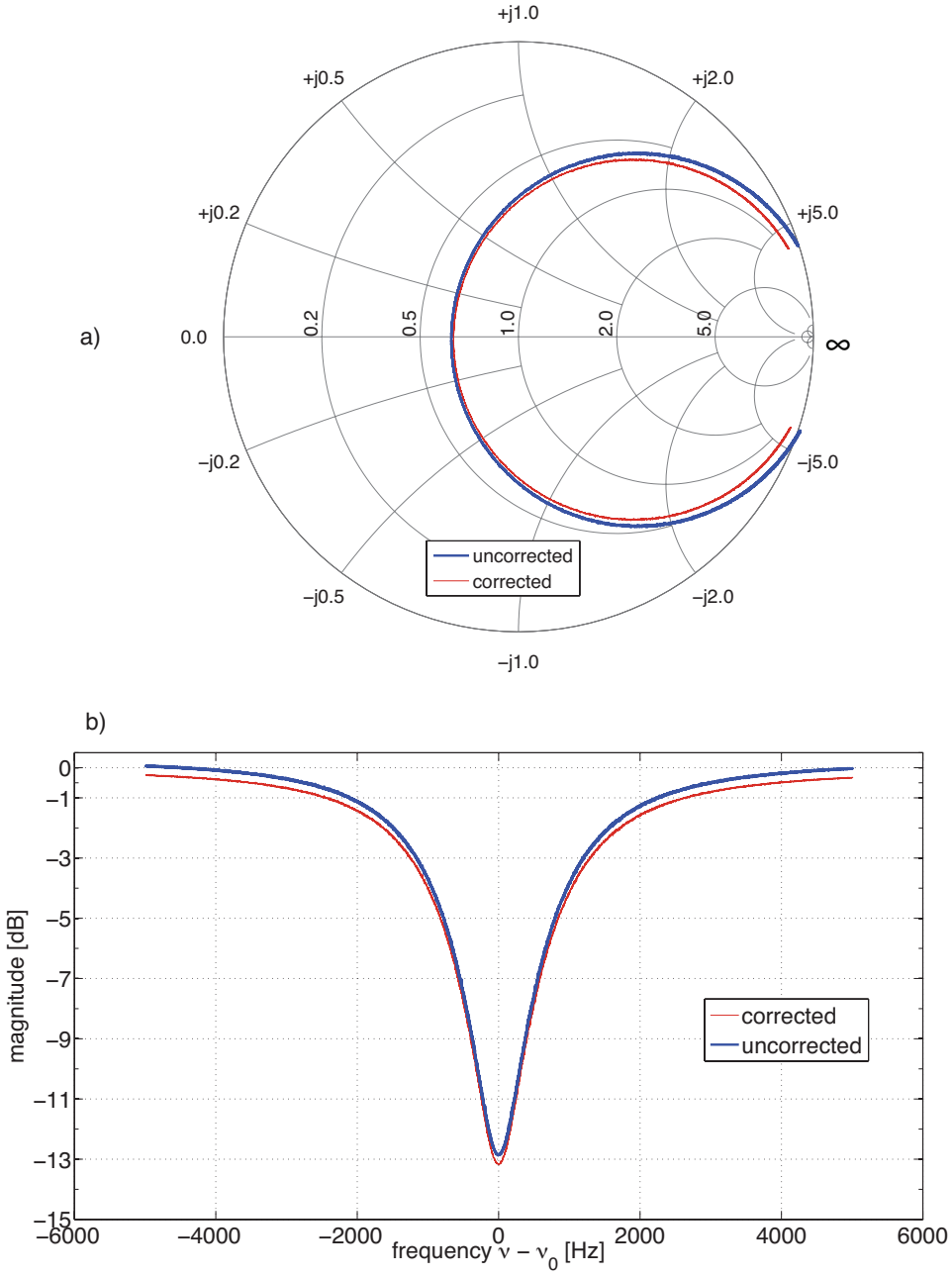

Figure 4.9.: Amplitude normalization of the **Z** trace a) shown in the Smith chart and b) shown as magnitude mapped to linear frequency axis (step 3).

The measurement result for two resonators (# 7 and # 10) is summarized in Table 4.2 and 4.3.

The measured factor of ~ 0.82 of the reduced inductance due to the presence of the copper

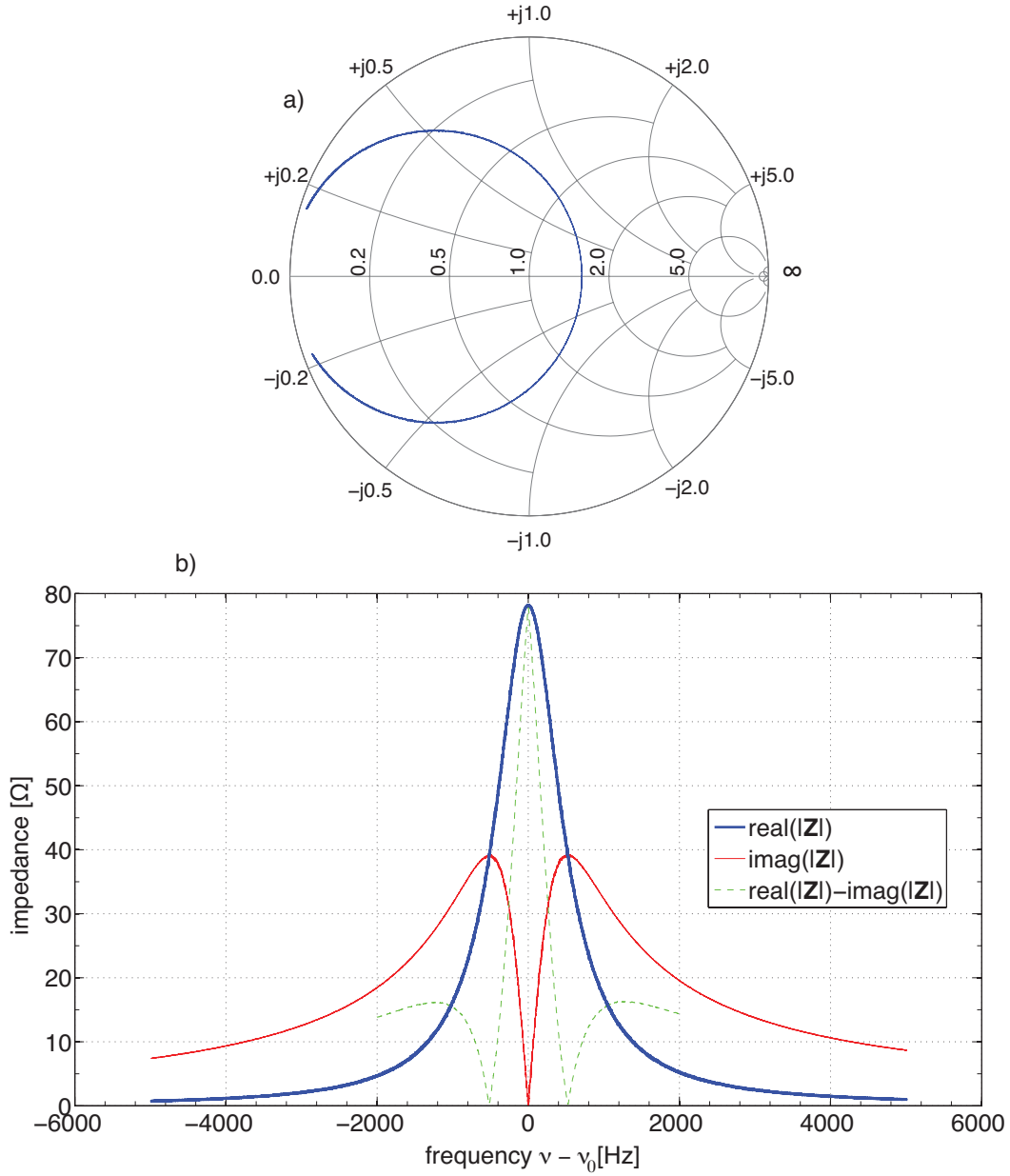

Figure 4.10.: a) Rotation of $\mathbf{Z}$ to the detuned short position. b) Absolute values of real($\mathbf{Z}$), imag($\mathbf{Z}$) and real($\mathbf{Z}$) − imag($\mathbf{Z}$) (step 5).

shield is in good agreement with the calculated value of 0.8 using equation (4.7).

Mounting the resonator, made of a superconducting coil, in a high magnetic field may lead to a reduction of the quality factor by about 20% at 1 T external magnetic field due to dissipative losses caused by the perturbed superconductor [70].

parameter	value
without copper shield	
inductance	2.82 µH
self-capacitance	2.9 pF
equivalent parallel resistance	2.2 MΩ
tuned resonance frequency	20.102 MHz
unloaded Q	19310
loaded Q	7660
self-resonance frequency	55.621 MHz
unloaded Q	3020
loaded Q	1330

Table 4.2.: Summary of resonator # 7 properties on teflon support without copper shield.

	without copper shield	with copper shield
inductance [µH]	2.2	1.8
self-capacitance [pF]	1.6	2.2
tuned resonance frequency [MHz]	23.304	25.230
unloaded Q	3614	8426
self-resonance frequency [MHz]	84.422	80.545

Table 4.3.: Summary of resonator # 10 properties on teflon support without and with copper shield.

4.3. Crystal Resonator

As described in more detail in [74] it is proposed to connect a crystal resonator to the Penning trap instead of the aforementioned LC circuit. This leads to several advantages, such as smaller physical dimensions for the same or higher Q-values, and no Q-factor degradation when mounted in high magnetic fields. Furthermore, the quartz resonator can be operated continuously over temperature, which gives the possibility to perform upfront measurements/optimization at room temperature . Crystals are widely used as oscillators because of their precise resonating frequencies. A crystal resonator exhibits a very high Q-factor due to the mechanical resonance of a vibrating piezoelectric material. Quartz materials are the most commonly used crystals. The orientation of their cuts from a natural crystal results in different piezoelectric properties, e.g. resonance frequency and temperature coefficient [75]. Figure 4.11 shows the orientation of such crystal cuts. The most common crystal cuts are single rotation (so-called AT-cut; $\phi = 0°$ and $\Theta = 34°$) and the double rotation (so-called SC-cut; $\phi = 22°$ and $\Theta = 34°$) [75].

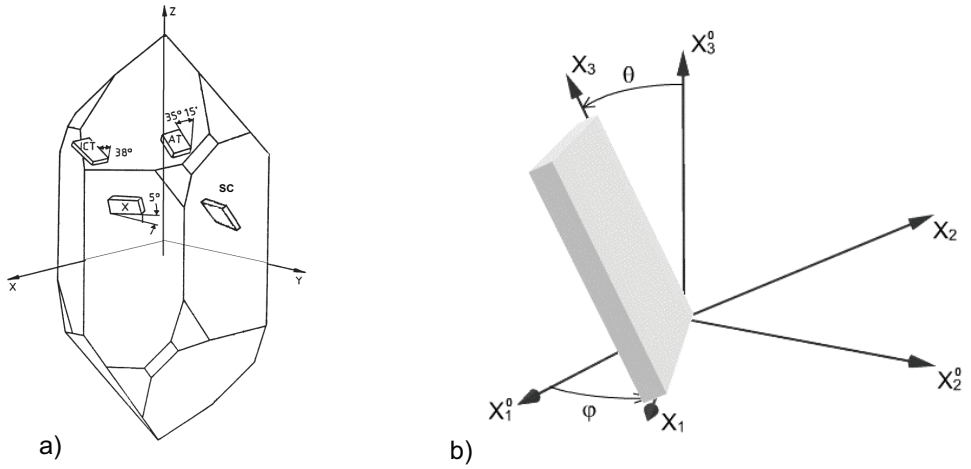

Figure 4.11.: a) Orientation of different cuts in natural quartz crystal. b) Definition of the crystal cuts by two rotation angles ϕ and Θ with respect to the crystallographic axes. (Figures adapted from [75]).

Once the quartz crystal is cut with respect to its crystallographic axes (see Figure 4.11), the crystal element is mounted on a holder which also provides the electrical connection to the electrodes plated on the quartz as shown in Figure 4.12 a).

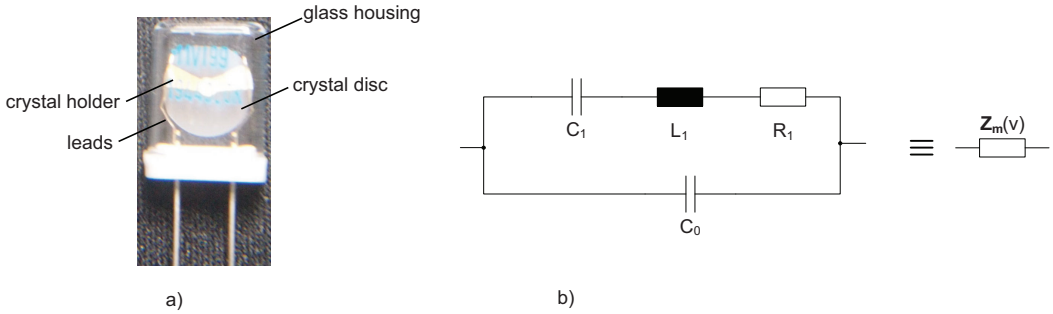

Figure 4.12.: a) Quartz resonator in evacuated glass housing. b) Equivalent electrical circuit of a crystal resonator.

The electrical equivalent circuit (so-called Butterworth Van-Dyke model) of a crystal resonator including the holder is shown in Figure 4.12 b). Its components are:

- C_0 is the shunt capacitance - parasitic capacitance including capacitance between electrodes, crystal holder, leads and enclosure.
- C_1 represents the motional capacitance which originates from mechanical elasticity.
- L_1 stands for the motional inductance caused by mechanical inertia.

- R_1 is the motional resistance which represents the mechanical losses of the resonating system.

The definition of a frequency-dependent complex impedance $\mathbf{Z}_m(\nu)$ is used later on in order to simplify electrical schematics and is calculated by

$$\mathbf{Z}_m(s) = \frac{\left[(sC_1)^{-1} + sL_1 + R_1\right](sC_0)^{-1}}{(sC_1)^{-1} + sL_1 + R_1 + (sC_0)^{-1}} \tag{4.10}$$

for $s = j\omega = j2\pi\nu$. This equivalent circuit represents a series and a parallel tuned circuit with the respective resonance frequencies

$$\nu_s = \frac{1}{2\pi\sqrt{L_1 C_1}} \text{ and } \nu_p = \nu_s\sqrt{1 + \frac{C_1}{C_0}}. \tag{4.11}$$

The parallel resonance, also called anti-resonance, occurs when the inductance L_1 tunes out the parallel combination of C_0 and C_1. Note that the equivalent circuit only describes one pair of resonance frequencies (ν_s and ν_p). Since the aim is to obtain high impedances, the series resonance is not interesting for this purpose. Quartz resonators may exhibit higher-order spurious modes which are described by different equivalent component values. Usually crystal resonators are sealed within an inert gas atmosphere e.g. nitrogen (N). This would lead to a problem when used at environmental temperatures below the freezing point of the gas. Hence, a quartz resonator operated at 4.2 K has to be sealed under vacuum. The resonator 404-29/231 produced by KVG Quartz Crystal Technology is a vacuum sealed, AT-cut quartz which resonates at 19.44 MHz (see Figure 4.12). It has been shown that quartz crystals are operable at cryogenic temperatures and in high magnetic field [76,77]. Typical values for equivalent components of the 19.44 MHz quartz are given in Table 4.4. The nominal load capacitance of this quartz is 25 pF in order to obtain the nominal series resonance frequency of 19.44 MHz.

equivalent component	value
L_1	13 mH ±20%
R_1	max. 40 Ω
C_1	5.15 fF ±20%
C_0	max. 2.5 pF

Table 4.4.: Typical values for the KVG quartz resonator 404-29/231. Values are taken from the datasheet.

Moreover, the parallel resonance frequency of the quartz resonator can be tuned by means of an additional parallel capacitance. In order to allow for dynamic tuning, a varactor diode is used. Figure 4.13 shows the schematic of the whole tuned circuit setup including quartz resonator, varactor diode and signal sources.

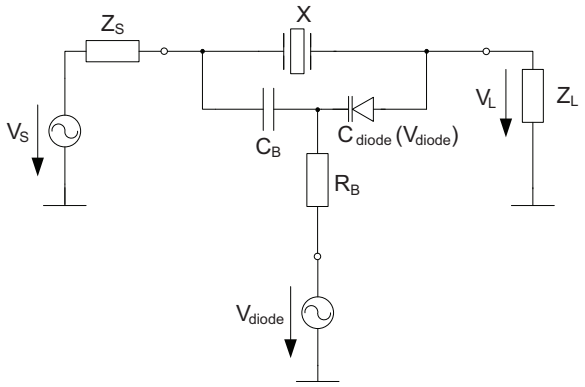

Figure 4.13.: Quartz resonator schematic with varactor diode for tuning the parallel resonance frequency. See text for the component values.

The tunability of the resonating circuit is calculated by inserting the additional parallel capacitance C_p into equation (4.11), yielding

$$\text{with } \xi := \sqrt{\frac{C_0 + C_1 + C_p}{C_0 + C_p}} \text{ to } \nu_p = \nu_s \xi. \tag{4.12}$$

C_p represents the series combination of the DC blocking capacitance C_b and the varactor diode capacitance C_{diode} and is calculated by

$$C_p = \frac{C_b C_{\text{diode}}}{C_b + C_{\text{diode}}}. \tag{4.13}$$

ξ is defined as tunability factor (see equation (4.12)) which gives $\xi \approx 1.00103$ for $C_p \to 0$ at the nominal parallel resonance frequency ν_p (for the case without parallel tuning capacitance) and $\xi = 1$ for $C_p \to \infty$ at the nominal series resonance frequency ν_s. In other words, the tunability span theoretically ranges from $\nu_s = 19.44$ MHz to $1.00103 \times \nu_s = 19.46$ MHz. Thus, the theoretical tuning span is about 20 kHz (see Figure 4.14). The diode capacitance is a function of the applied voltage $C_{\text{diode}}(V_{\text{diode}})$. In order to achieve a tunability of the quartz resonator comparable to the bandwidth of the LC circuit shown in Table 4.2, the parallel capacitance C_p has to be chosen in order to change the

parallel resonance frequency by at least 3 kHz. Moreover, the blocking capacitor C_b has to be larger than the minimal diode capacitance $C_{\text{diode,min}}$ since the lower capacitance dominates in a series configuration. However, the theoretical frequency change versus the added C_p is shown in Figure 4.14 . This leads to the specification of C_p to lie between 0 pF and 3 pF. Since no varactor diode provides a $C_{\text{diode,min}}$ equal to 0 pF, a diode with a very small $C_{\text{diode,min}}$ and a wide tuning range (large $C_{\text{diode,max}}/C_{\text{diode,min}}$) has to be chosen. A wide tuning range also allows to operate the varactor diode in its low-loss states without compromising the minimal bandwidth of 3 kHz. Moreover, the diode should be operable at 4.2 K without major changes in the tunability, thus devices based on silicon have to be avoided [78, 79]. The GaAs varactor diode MA46461 from M/A-COM Technology Solutions Inc. was chosen because it has a high total capacitance ratio of $C_{\text{diode,max}}/C_{\text{diode,min}} = C_{\text{diode,2V}}/C_{\text{diode,20V}} \approx 5.6$ with a $C_{\text{diode,min}} = C_{\text{diode,20V}} \approx 1.3$ pF (see Table 4.5), it is a low-loss device and since it is made of GaAs it is expected not to substantially change its properties when cooled to 4.2 K [78].

capacitance [pF]	diode voltage [V]
7.12	2
4.54	4
1.27	20

Table 4.5.: Specification of the M/A-COM varactor diode MA46461 given in the datasheet.

The blocking capacitor was chosen as $C_b \approx 2$ pF since $C_b > C_{\text{diode,min}}$, and the tuning range in terms of frequency should be more than 3 kHz (see Figure 4.14).

Plugging the specification of the MA46461 diode into equation (4.13) gives a capacitance range of the parallel capacitance from $C_{p,\text{min}} = 0.78$ pF to $C_{p,\text{max}} = 1.56$ pF.

4.4. Characterization of the Crystal Resonator

The cryogenic measurement setup described in chapter A.1.1 was used for the characterization of the quartz resonator. In order to measure the high impedance behavior of the crystal resonator at its parallel resonance frequency, the quartz including the blocking capacitor and tuning varactor diode or varicap (see Figure 4.13) was measured in transmission mode within the 50 Ω environment of the highly sensitive vector network analyzer (VNA) E5071C from Agilent. Figure 4.15 shows the electrical equivalent circuit of the measurement system. Note that the DUT is shown as a 2-port and the source ($\mathbf{V}_0$

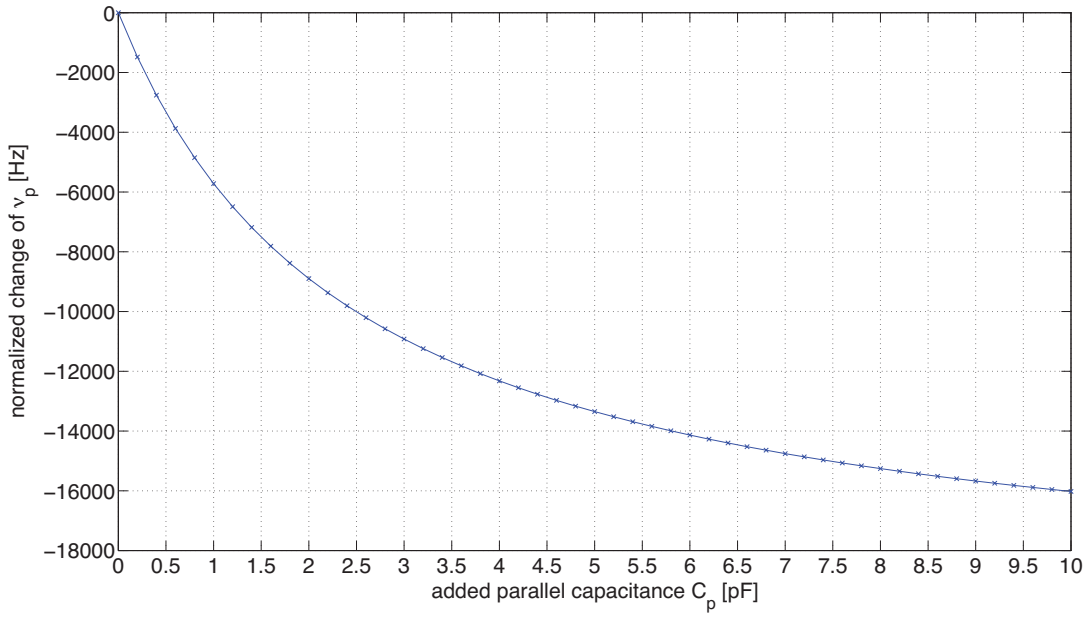

Figure 4.14.: Theoretical tuning range of the parallel resonance frequency ν_p by means of a parallel capacitance C_p. Note that the y-axis is normalized to the maximum ν_p for $C_p = 0$ pF

ans Z_s) and load (Z_L) are inside the VNA. Port 1 and 2 designate the two measurement ports of the VNA.

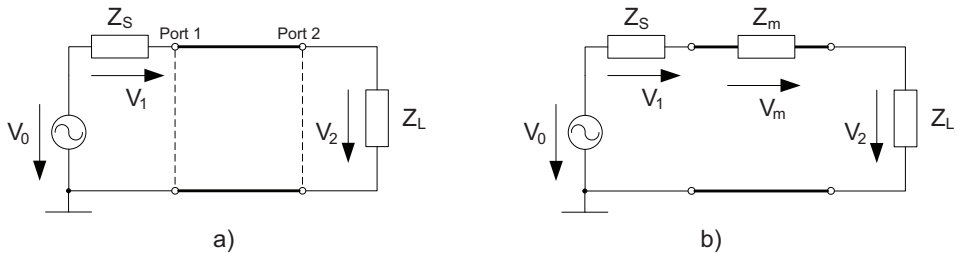

Figure 4.15.: a) Equivalent electrical circuit of the measurement system without DUT. b) Measurement system with the DUT represented as complex impedance $\mathbf{Z}_m$.

The output voltage $\mathbf{V_2}$ is a complex quantity and is calculated by

$$\mathbf{V_2} = \mathbf{V}_0 \frac{Z_L}{Z_S + Z_L}, \tag{4.14}$$

where Z_L and Z_S are real numbers and without DUT. Since the VNA provides a 50 Ω source and load impedance ($Z_L = Z_S = 50\,\Omega$), the output voltage $\mathbf{V_2} = \mathbf{V_0}/2 =: \mathbf{V}_{\text{ref}}$. Using the reference voltage in order to normalize the measured potential, the transmission scatter parameter is expressed by

$$\mathbf{S_{21}} = \frac{\mathbf{V}_2}{\mathbf{V}_{\text{ref}}} = \frac{2Z_L}{Z_S + Z_L + \mathbf{Z}_m}. \tag{4.15}$$

Thus, the crystal resonator impedance $\mathbf{Z}_m$ (see Figure 4.12) is calculated by

$$\mathbf{Z}_m = \left(\frac{1}{\mathbf{S}_{21}} - 1\right) \times 100 \tag{4.16}$$

for $Z_L = Z_S = 50\,\Omega$.

Table 4.6 gives an overview about the measured series and parallel resonance frequencies of the quartz resonator for room temperature and 4.2 K as well as the magnitude of the impedance at parallel resonance. Note that ν_s is not exactly 19.44 MHz because the load capacitance was lower than 25 pF and that ν_s changes by a factor of about two more than ν_p when cooled. A possible explanation for the reduced resonance frequency is the crystal's frequency-temperature dependence which is primarily determined by the cut angle [75]. Below the so-called lower turnover point (see Figure 4.16) of the crystal's frequency-temperature dependence[2], the relative frequency change is negative [80]. Furthermore, the magnitude of the impedance at parallel resonance doubles from 290 K to 4.2 K (see Figure 4.17).

condition	ν_s [MHz]	ν_p [MHz]	$max(\lvert\mathbf{Z}_m\rvert)$[MΩ]@$\nu_p$
290 K	19.438128	19.480148	6.0
4.2 K	19.383062	19.455524	12.4
abs. change 290 K to 4.2 K	0.055066	0.024624	6.4

Table 4.6.: Overview of the measured characteristic frequencies of the crystal resonator without tuning capacitance.

Since the measured parallel resonance frequency differs from the theoretical one by $\sim$ 2 kHz, the crystal shunt capacitance C_0 has to be corrected. Thus, the maximal datasheet value of $C_0 = 2.5$ pF is reduced to $C_0 = 1.2$ pF using the measured ν_p at room temperature and solving equation (4.11). Taking the measured parallel resonance

[2]The frequency-temperature dependence is described by a third order parabola.

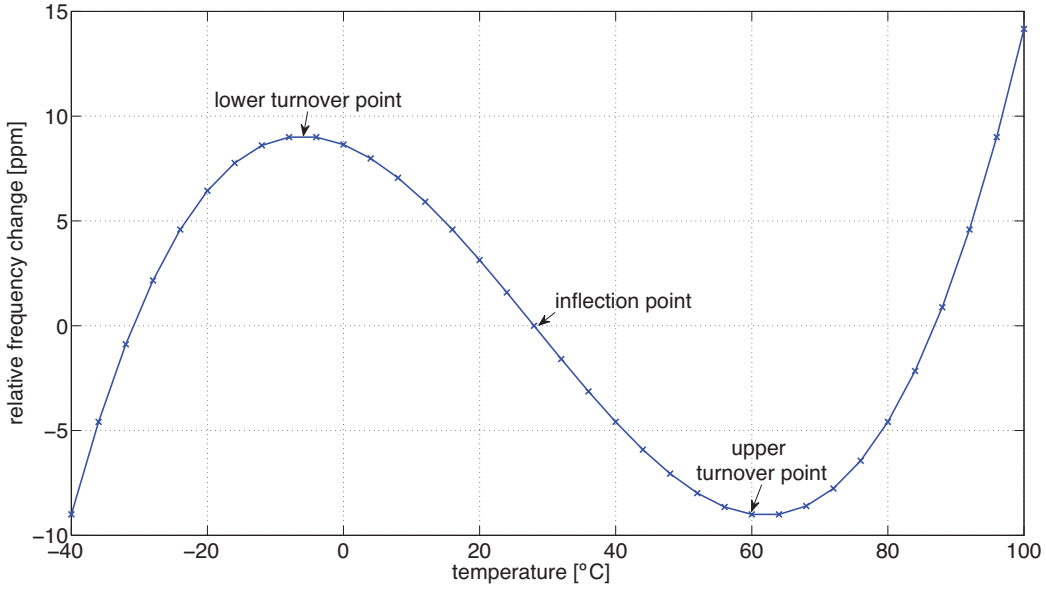

Figure 4.16.: Typical frequency-temperature characteristic of an AT-cut crystal near room temperature. The unit of the relative frequency change is parts per million (ppm).

values (see Figure 4.18) at 290 K, and solving equation (4.12) for C_p, gives a parallel capacitance of $C_{p,2V} = 1.82$ pF for 2 V diode bias and $C_{p,20V} = 0.91$ pF for 20 V, respectively. These deduced parallel capacitance values for 2 and 20 V bias voltage are in good agreement with the calculated values of 1.56 pF and 0.78 pF respectively. The difference may be due to the tolerance of the blocking capacitance and the setup. The measured tunability of the crystal resonator is given by the difference between parallel and series resonance frequency. Using the measured values in Table 4.6 for room temperature, the tuning range is about 40 kHz, which is about twice the theoretical expected value (see Figure 4.14). The reason for this discrepancy is the reduction of the shunt capacitance ($C_0 = 1.2$ pF instead of $C_0 = 2.5$ pF). Plugging the reduced C_0 value into equation (4.12), the theoretical tunability at room temperature is ∼7.2 kHz. This value is in excellent agreement with the measurement (see Figure 4.20 between $V_{\text{diode}} = 2$ V and $V_{\text{diode}} = 20$ V).

Figure 4.18 shows the quartz resonator impedance for different tuning voltages at 290 K and Figure 4.19 at 4.2 K, respectively. In order to directly compare the two before mentioned plots, Figure 4.20 depicts the tunability as a function of the tuning voltage in a normalized manner. The figure is created by taking the parallel resonance frequency

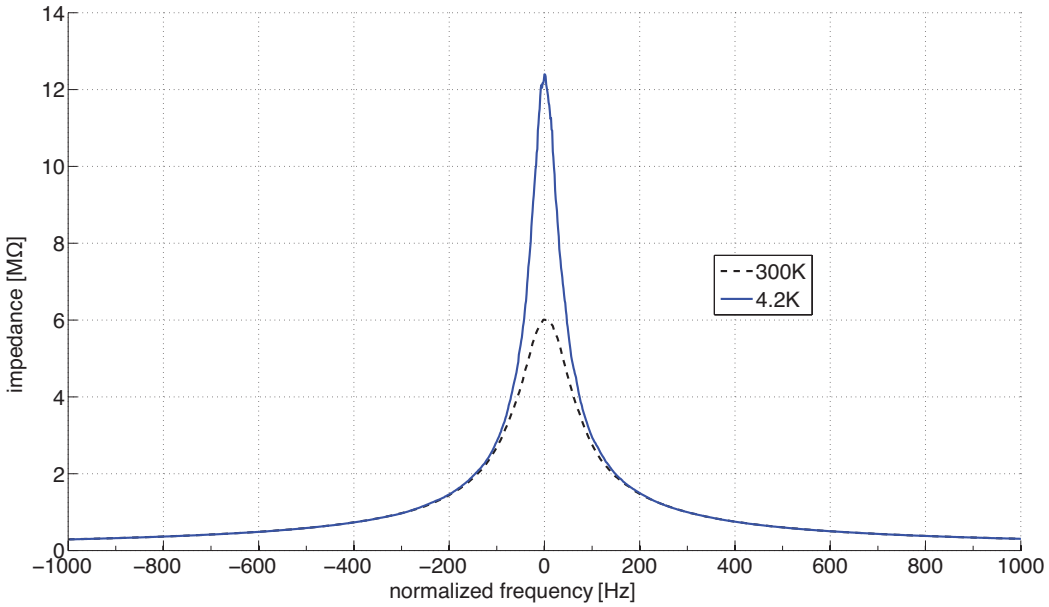

Figure 4.17.: Magnitude of the crystal resonator impedance at parallel resonance at 290 K and 4.2 K. Note that the frequency is normalized to the respective parallel resonance frequency ν_p for each temperature and that there was no parallel capacitance connected.

points from Figure 4.18 and 4.19 and plotting them against V_{diode}.

As already indicated in Figure 4.17, the impedance is significantly increased when cooling the quartz resonator to 4.2 K. Compared to room temperature, the GaAs varactor diode shows at 4.2 K almost the same frequency tuning behavior up to a diode voltage of $V_{\text{diode}} = 15$ V. Furthermore, the absolute difference of ν_p when cooling is preserved since the frequency shift of about 24.62 kHz (see Table 4.6) is measured between 24.38 kHz and 24.58 kHz for $V_{\text{diode}} = 0$ V to $V_{\text{diode}} = 10$ V. This allows to draw the conclusion, that there is no significant capacitance change of the varactor diode at cryogenic temperature. However, a slight reduction of the capacitance occurs and the parallel capacitance at 4.2 K is quantified as 1.01 pF for $V_{\text{diode}} = 0$ V and 0.57 pF for V_{diode} =20 V. This result is in agreement with the data presented in ref. [79] and [81] where the decrease in capacitance at low temperatures was found to originate from the depletion width increase. The parallel capacitance values are summarized in Table 4.7. Above 15 V diode bias voltage, the saturation effect becomes apparent because of the fully depleted diode junction.

The measured quality factors of the crystal resonator were larger than 10^5 (see details in

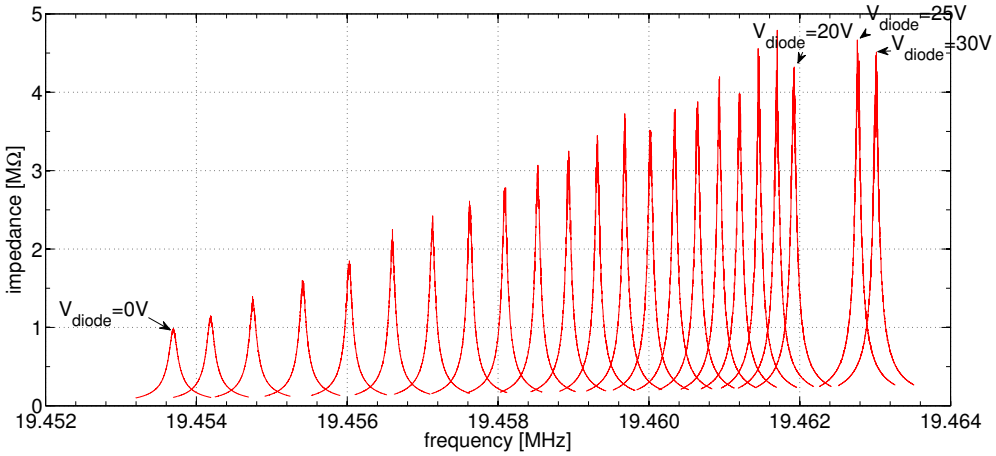

Figure 4.18.: Magnitude of the crystal impedance at 290 K for different tuning voltages V_{diode} at 4.2 K. Note that V_{diode} is increased in 1 V steps until 20 V and then in 5 V steps.

	C_p [pF]	
V_{diode} [V]	4.2 [K]	300 [K]
0	1.01	1.82
20	0.57	0.91

Table 4.7.: Overview of the deduced parallel tuning capacitance values C_p.

ref. [74]) at 4.2 K. However, the more important figure of merit is the peak impedance ($max(|\mathbf{Z}_m|)$) at parallel resonance (see Table 4.6), which are higher than those measured for the superconducting coil.

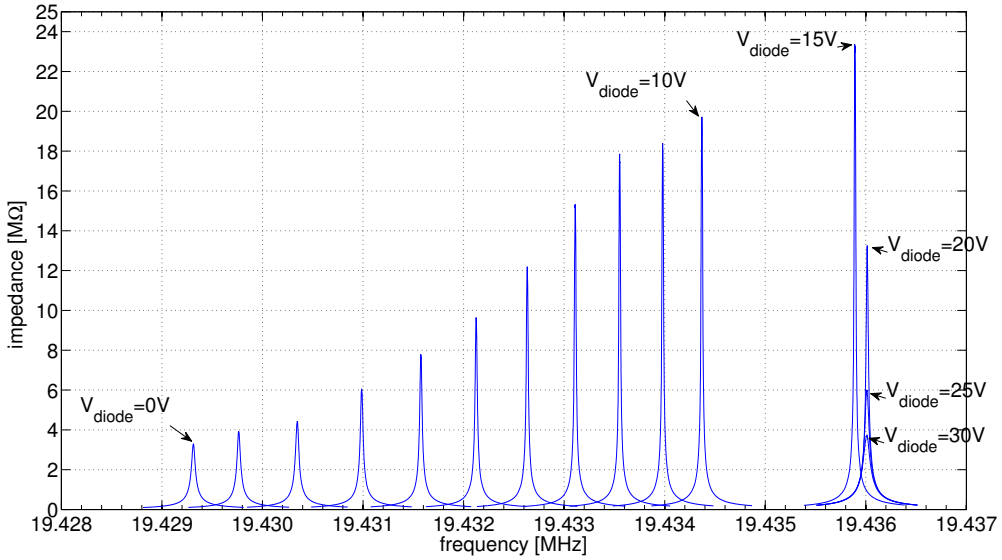

Figure 4.19.: Magnitude of the crystal impedance at 4.2 K for different tuning voltages V_{diode} at 4.2 K. Note that V_{diode} is increased in 1 V steps until 10 V and then in 5 V steps.

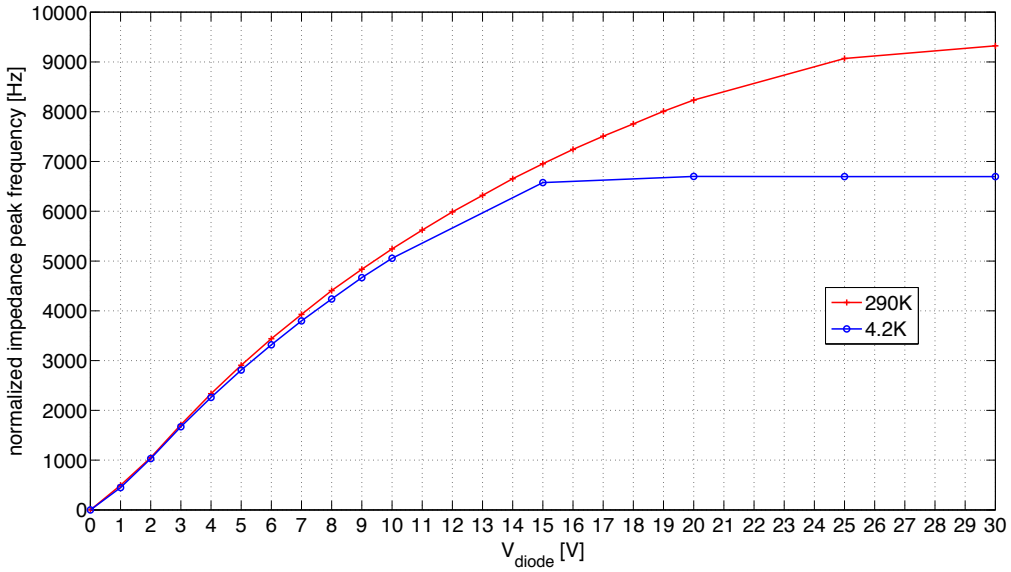

Figure 4.20.: Quartz resonator tunability as function of the tuning voltage. The line is meant to guide the eye. Note that the y-axis is normalized to the lowest parallel resonance frequency $\nu_{p,0V}$ at zero diode voltage.

5. Cryogenic Switch

In low temperature environments there is often the need to switch signals. A typical application is shown in Figure 5.1 where a Penning trap should be connected and disconnected to/from readout electronics. One use case could be to disconnect the whole readout electronics with switch $sw1$ in order to measure the resistive cooling effect of the tuned circuit. Another application could be to disconnect the cryogenic amplifier with switch $sw2$ in order to see if there is amplifier noise driving the trapped particles.

The straightforward solution for signal switching at cryogenic temperatures is to use, for instance, evacuated relays such as the Teledyne RF180 series or special cryogenic microelectromechanical systems (MEMS) switches [82].

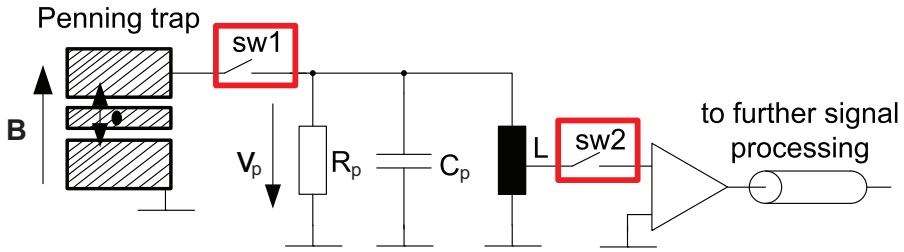

Figure 5.1.: Typical application for a switch that electrically connects/disconnects the whole readout electronic chain (sw1) or the cryogenic amplifier only (sw2).

It is important that the switch is not sealed with an inert gas atmosphere which could freeze when cooled below its freezing point. An additional difficulty occurs when operating such switches in a cryogenic environment and a high magnetic field. Relays, which are in general switched by means of electromagnetic actuation, cannot operate in high magnetic field environments. MEMS switches are operable if the used materials are non-magnetic and the activation takes place by electrostatic potentials. Another technology, suitable for low temperature application and high magnetic field, are GaAs monolithic microwave integrated circuit (MMIC) switches. The disadvantage of MMIC switches is that their on-resistance is several ohm. An example is the GaAs switch SW-

239 (M/A-COM Technology Solutions Inc.) which has an on-resistance of about[1] 2 Ω at 290 K. In the following section the performance of DC contact MEMS switches at 4.2 K is presented.

5.1. Microelectromechanical Switch

Microelectromechanical systems have been studied for more than a decade because of their small size, superior radio frequency (RF) performance and low power consumption over a broad band of frequencies. There are MEMS switches commercially available from two manufacturers, Omron (e.g. 2SMES-01) and RadantMEMS (e.g. RMSW101). Both producers use hermetically sealed switches within a nitrogen atmosphere. The nitrogen freezes out at temperatures below 77 K, thus these switches are not suitable for operation at 4.2 K. Since there is no commercial product available which would work at 4.2 K, switches from a research institution were obtained. The DC performance of RF MEMS switches, designed and manufactured by the Micro System Components Section, CEA-LETI, Grenoble, France [83], was evaluated. Furthermore, the on-resistance R_{on} was chosen as a figure of merit since the switches are designed to operate at GHz frequencies and the frequency range of interest is up to about 30 MHz. Moreover, the on-resistance gives very useful information about the switch state. Figure 5.2 shows the DC-60GHz RF-MEMS switch. The switch contact is made of ruthenium (Ru) and is held by a silicon nitride (SiN) membrane which is fixed at two points forming a bridge (see Figure 5.2 a)). Underneath the contact there is a coplanar waveguide. The two waveguide segments are shorted by the metallic contact when an actuation voltage of $V_{\mathrm{cc}} = 50$ V is applied between the two electrodes (electrode 1 and 2) and the ground plane due to the pulled-down membrane [83]. The switch is released when the actuation voltage turns to $V_{\mathrm{cc}} = 0$ V since the membrane returns to its original position.

Since the switch is a mechanically moving part, it has to be protected from contamination by a cap made of silicon. The silicon cap is attached to the surface by means of a polymer glue (see Figure 5.2 a) and c)). This glue seals the switch within a nitrogen atmosphere but it is not hermetic. The switch dice (see Figure 5.2 c)) was glued with Stycast 2850FT (by Emerson & Cuming Inc.) into a 8-lead small outline integrated circuit (SOIC) surface mount package SOIC150-08-OP-01 produced by Sempac Inc. (see Figure 5.3). Stycast 2850FT (round shaped black spot in Figure 5.3) is a black resin which is commonly used in cryogenic applications because of its good thermal conduction and stability at low

[1] Holger Kracke, private communication

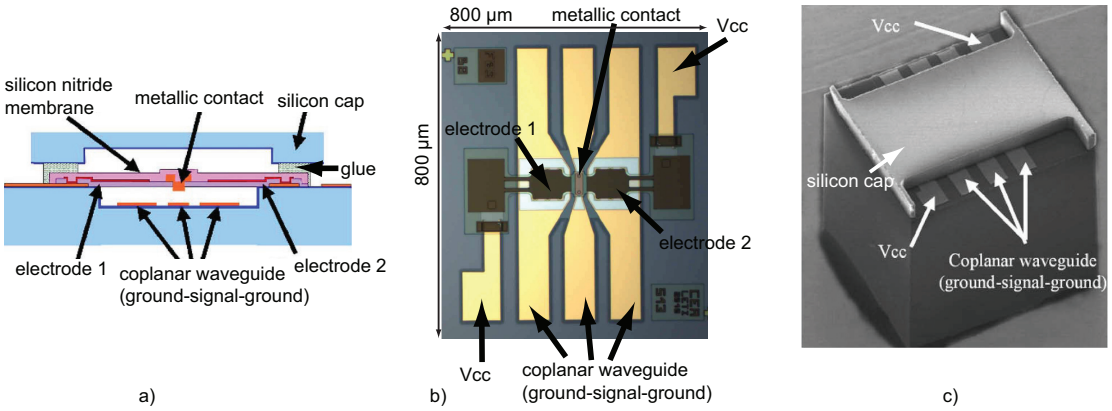

Figure 5.2.: CEA-Leti MEMS switch. a) Schematic in cross section view. b) Top view photograph. c) Photograph of the silicon dice. (Figures adapted from [83])

temperatures [84]. Since the MEMS switches are equipped with gold pads, gold ball bonding was chosen to connect the switch to the package in order to match the material. The bonding was done at the EPFL[2] in Lausanne, Switzerland, because there is only aluminum wedge bonding available in the bonding lab at CERN.

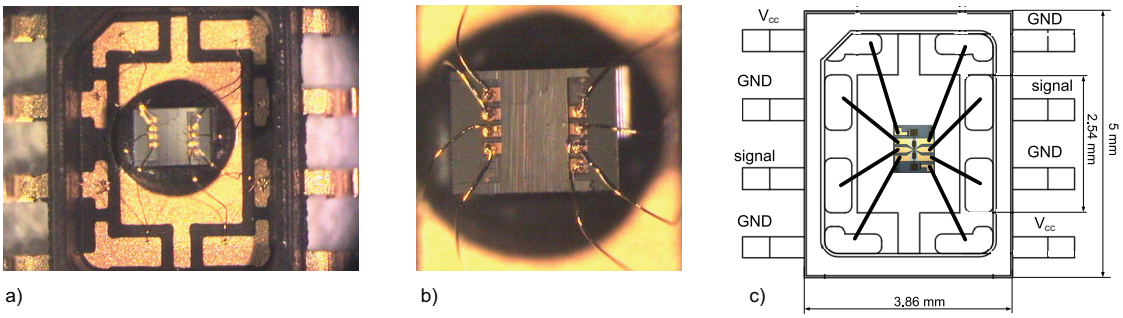

Figure 5.3.: Bonding of the CEA-Leti MEMS switch into an 8-lead package. a) Photograph of the package and the bonded MEMS dice. b) Close-up of MEMS switch and its gold ball bonded leads. c) MEMS switch bonding scheme.

Note that the MEMS switch is rotationally symmetric and therefore there is no need to use signal in and out nomenclature of the wave guide pads enclosed by the signal ground (GND). The SOIC package is slightly magnetic due to its 0.76 μm thick nickel plating on the copper leadframe and underneath the top gold layer[3]. Moreover, the package body is made of a semiconductor grade plastic and it is therefore not expected to outgas sub-

[2]Dr. Pavel Kejik from Electronics and Signal Processing Laboratory performed the gold ball bonding.
[3]Information taken from Sempac product data sheet - SSOP/SOIC (Document # MKT-SOIC-DS-01-R2)

stantially[4]. Outgassing properties of similar chip packages made of plastic is summarized in [85] where these packages are referred to as plastic encapsulated microcircuit (PEM).

Five MEMS switches (labeled I16, J16, K16, L16 and O16) were tested at 290 K and 4.2 K. The cryogenic measurement setup (described in section A.1.1) was used for the room temperature and cryogenic measurement. In order to ease the changing of the device under test (DUT) - the MEMS switch - a 14-pin SOIC adapter socket LEW903 (Lewmax programming) was used. This socket was soldered with its vertical through holes onto a printed circuit board (PCB), which was used for the wiring and mounting (see Figure 5.4).

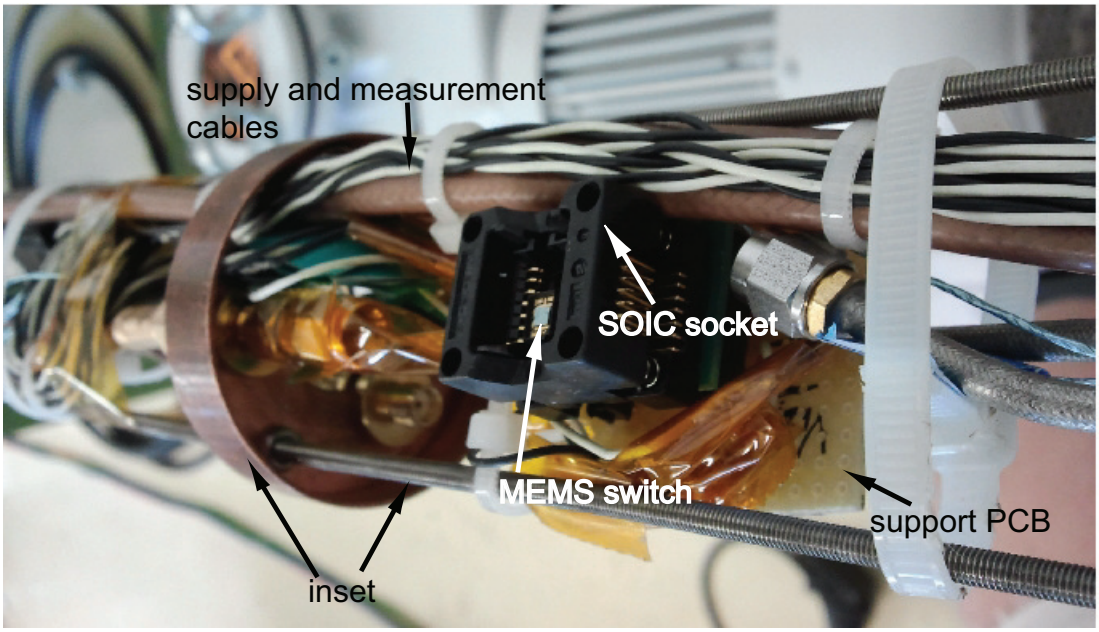

Figure 5.4.: Inset for the MEMS switch measurement. The SOIC adapter is mounted on the inset which in turn was inserted into a cryostat. (Details about the cryogenic measurement setup are given in section A.1.1)

The on-resistance of the switches was measured with a Keithley 2000 multimeter in 4-wire configuration. Since the switch measurement setup, including the SOIC socket and cabling, is smaller than the inset diameter of about 50 mm, the cryostat was kept at 4.2 K and the inset with the DUT was pulled out. Doing so, a lot of time was saved because the cryostat was not warmed up when changing the DUT. Usually it takes about 12 hours to boil away the liquid helium and to warm up the cryostat with a heater mounted on

[4]http://outgassing.nasa.gov/

the inset. Care was taken when reinserting the inset into the cold cryostat in order not to thermally shock the switches too much.

	at 290 K		at 4.2 K	
switch	R_{on} [Ω]	V_{cc} [V]	R_{on} [Ω]	V_{cc} [V]
I16	3.0	40	11.0	70
J16	2.8	40	4	60
K16	3.3	30	13.8	50
L16	3.3	50	4.8	50
O16	3.6	40	8.0	40

Table 5.1.: Overview of the measured on-resistance (R_{on}) values at 290 K and 4.2 K.

The on-resistance results of the MEMS switches are summarized in Table 5.1. Note that the different activation voltages V_{cc} were chosen in order to read a stable R_{on} since some switches showed fluctuations at 290 K and 4.2 K. As a consequence of cooling, there is in general the need to apply higher activation voltages due to the stiffer membrane in order to maintain the force for pulling down the contact. Looking at the measured R_{on} values, the higher activation voltage cannot fully compensate the reduced force. Since the conductivity of ruthenium increases when cooled [86], the increased R_{on} results from less contact force. Another finding is the increase of the on-resistance over time[5] due to contamination of the contact since the switch is not sealed hermetically. One can compensate this effect by applying even higher activation voltages. After the R_{on} evaluation at cryogenic temperatures, the next measurement was to study the switch performance in a high magnetic (**B**) field. Since there was no measurement setup available for measurements in high **B**-field *and* cryogenic temperatures, the evaluation was conducted at room temperature. The measurement setup for the switch evaluation in a **B**-field is described in section A.2. At the time the switches were evaluated in the **B**-field, there was only one switch (L16) out of five working reliably. The activation voltage was increased to 130 V in order to obtain reliable switching behavior at room temperature. First, the switch was positioned in the fringe field of the magnet in order to test its function. Already at this point, the on-resistance was fluctuating due to the presence of a **B**-field of about 14 mT. The switch was then moved into the magnet bore and the **B**-field was ramped up to about 200 mT. At a field strength of about 50 mT, the switch snapped on and was stopped working. Some two hours later, the switch was operable again and the same test was repeated. This time, the switch was operable up to 250 mT and the R_{on} was

[5]The time span between the evaluation of the switch at cryogenic temperature and in high magnetic field was more than one year.

reduced from about 9 Ω without **B**-field to 5.4 Ω at 239 mT. The dependence of the switching behavior and hence the on-resistance may be caused by the magnetization of the contacts since ruthenium is paramagnetic. However, due to the fact that the tested MEMS switch demonstrated unreliable switching behavior in a high **B**-field, a different device has to be chosen for signal switching.

5.2. Piezoelectric Switch

A single pole single throw (SPST) switch (see Figure 5.5 b)) made of a piezoelectric (piezo) activated bender (see Figure 5.5 a)), designed for cryogenic temperature and high magnetic field has been characterized. The piezo bender PL140.10 is made of the ceramic material - lead zirconate titanate (PZT) - and is produced by Physik Instrumente (PI) GmbH & Co. In [87] the low temperature properties of this piezo bender made of two different ceramic materials (PI nomenclature: PIC251 and PIC255) were evaluated and it was shown that they work at 4.2 K with reduced deflection performance. Taking the nominal deflection of ±1 mm at room temperature as reference, this deflection is reduced by a factor between 6.4 (PIC255) and 16.6 (PIC251) when cooled to 4.2 K [87].

The switch contact is realized by a 150 nm gold layer sputtered on the piezo bender (see Figure 5.5 a)) and the two permanent contacts of a Teledyne magnetic-latching radio frequency (RF) relay (RF180 series (see Figure 5.5 b)). The piezo bender and the relay contacts are mounted on an aluminum support. Since the RF relay is fixed directly on the aluminum surface, the leads have to be insulated by means of a kapton foil. The piezo bender is held by two screws and an aluminum bar (bottom right in Figure 5.5 b)).

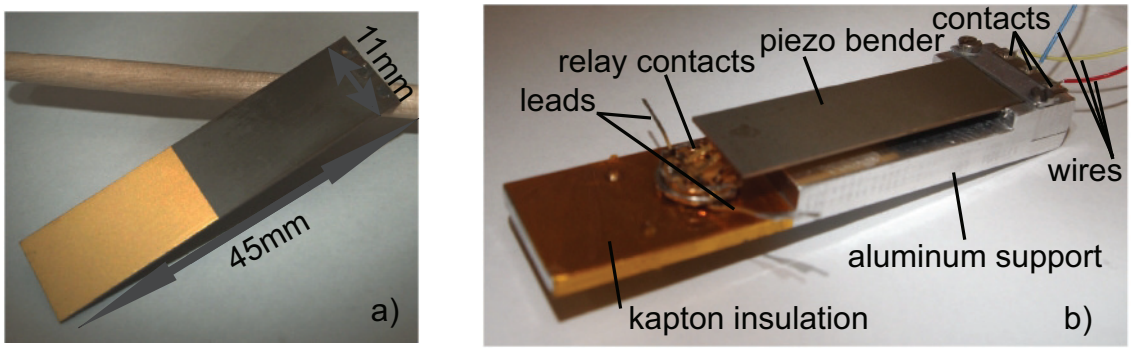

Figure 5.5.: a) Photograph of the piezo bender with the gold sputtered area. b) Photograph of the assembled piezo switch.

Note that there was the need for an additional insulation layer - spacer - (see Figure 5.6) of about 0.34 mm thickness between the piezo bender surface and the gold contact since the ceramic material introduces additional loss and the switch RF performance deteriorates (see Figure 5.7 a)). The spacer material is standard printed circuit board (PCB) laminate (FR-4) and it provides sufficient decoupling between the gold surface and the lossy piezo bender. In order to deflect the piezo bender, two DC voltages (V_{bias} and V_{switch}) have to be applied in the range of $0\,V \leq V_{\text{switch}} \leq V_{\text{bias}}$. Taking the piezo bender orientation in Figure 5.6 a), the electrical configuration of $V_{\text{switch}} = 0\,V$ and $V_{\text{bias}} = 40\,V$ deflects the piezo bender vertically downward and closes the electrical connection by touching the relay contacts. Applying $V_{\text{switch}} = V_{\text{bias}} = 40\,V$ moves the piezo element up, and the switch opens. The switch default position is $V_{\text{switch}} = V_{\text{bias}} = 0\,V$. In this case the bender is not polarized and its mechanical setup determines whether the switch is "normally closed" or "open". Note that all measurements presented in this chapter were taken with a default closed switch.

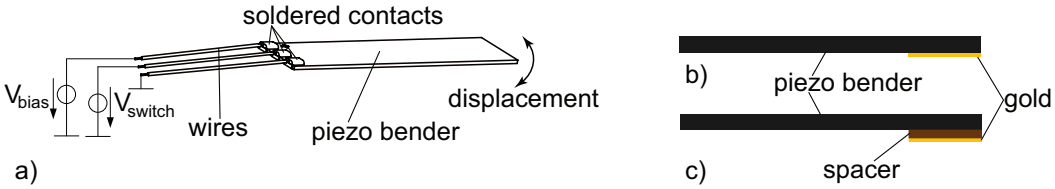

Figure 5.6.: a) Electrical connection of the piezo bender in order to perform vertical displacement. b) Schematic of the piezo bender with sputtered gold surface on the bottom. c) Piezo bender with spacer glued to the bottom with gold surface on the spacer. Note that the spacer and the gold surface dimension is not to scale with respect to the piezo bender.

Figure 5.7 shows the piezo switch RF performance with spacer at room temperature for open and closed positions. The insertion loss (IL) of the switch is below 0.2 dB within a bandwidth of about 100 MHz and the isolation performance in this frequency band is limited by the capacitive coupling of the relay contacts (see Figure 5.7 b)). The switch is suitable for DC switching applications as well as for RF signals and it has a DC on-resistance at 4.2 K of 0.13 Ω and 0.21 Ω at room temperature. Due to the galvanic isolation and low switch capacitance, the switch has a high insulation. Note that the on-resistance was measured with the relay leads, thus the contact resistance is smaller than the aforementioned values.

The switch performance at cryogenic temperature is shown in Figure 5.8. Since the piezo bender has reduced deflection at 4.2 K there is the need to apply higher switching voltages

compared to 290 K in order to get the excellent isolation performance. While applying $V_{\text{switch}} = V_{\text{bias}} = 40\,V$ leads to an isolation of about -67 dB at room temperature and 20 MHz frequency (see Figure 5.7 b)) one has to apply $V_{\text{switch}} = V_{\text{bias}} = 100$ V at 4.2 K (see Figure 5.8 b)) to reach the same isolation value.

The RF performance of the piezo switch was measured with the Agilent vector network analyzer (VNA) E8358A which had been full 2-port calibrated with the female SMA calibration kit 85033D. Since the system (VNA and cables) was calibrated at room temperature, the insertion loss trace is shifted to about +0.5 dB when cooled to 4.2 K (red trace in Figure 5.8 a)) due to the reduced loss. The shifted trace was obtained by replacing the switch by a short. This offset is used in order to correct the measured insertion loss data of the switch at 4.2 K. The result shows an insertion loss of less than -0.1 dB within a 100 MHz bandwidth. The switch performance at low temperature was evaluated using the cryo-cooler measurement setup (detail are provided in Section A.1.2). Furthermore, the switch was evaluated in high magnetic field of about 0.5 T without performance degeneration. Details about this measurement are shown in chapter A.2.

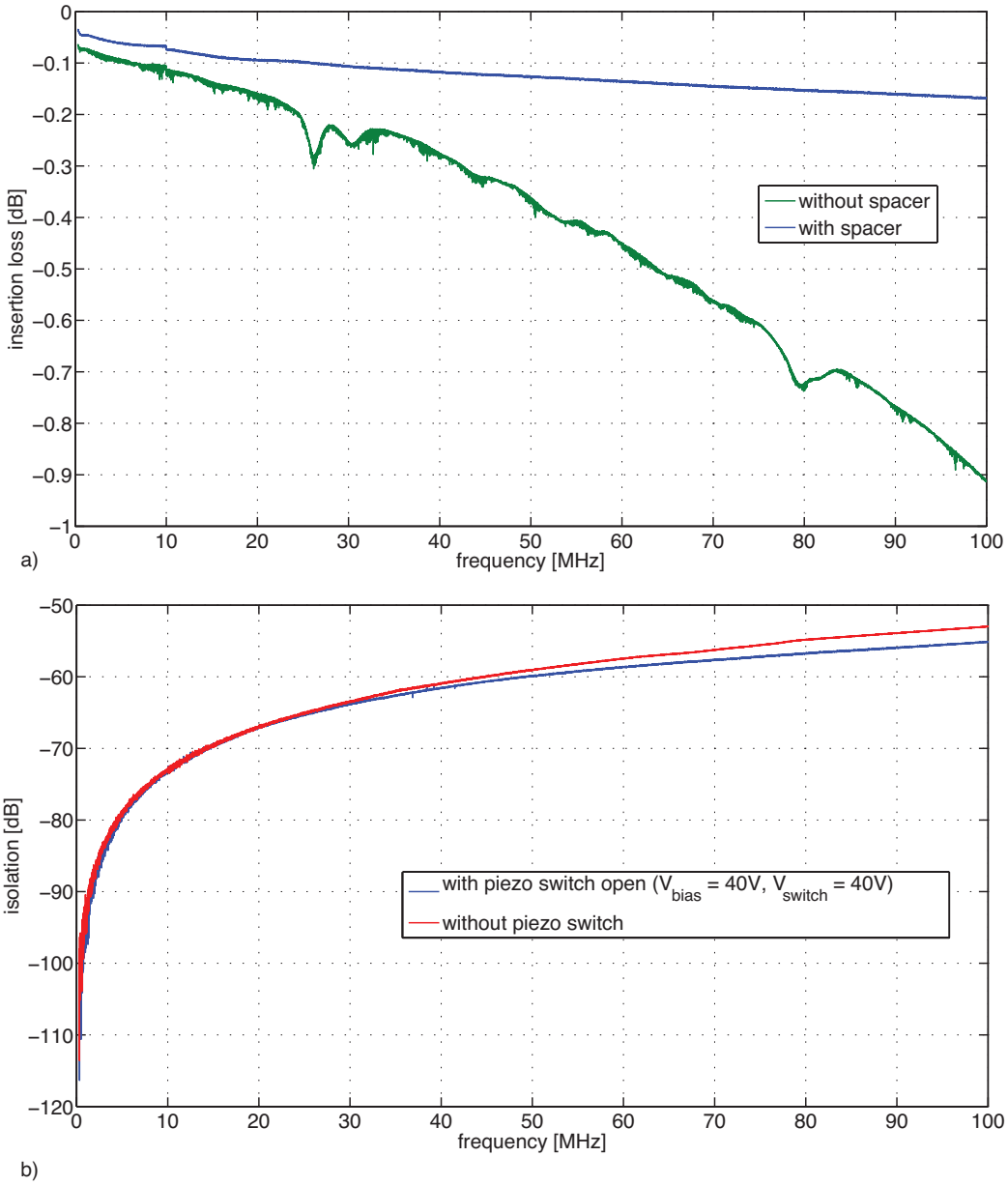

Figure 5.7.: Piezo switch RF performance at 290 K. a) Switch in closed position with and without spacer. b) Switch in open position (blue) and switch contacts without piezo bender.

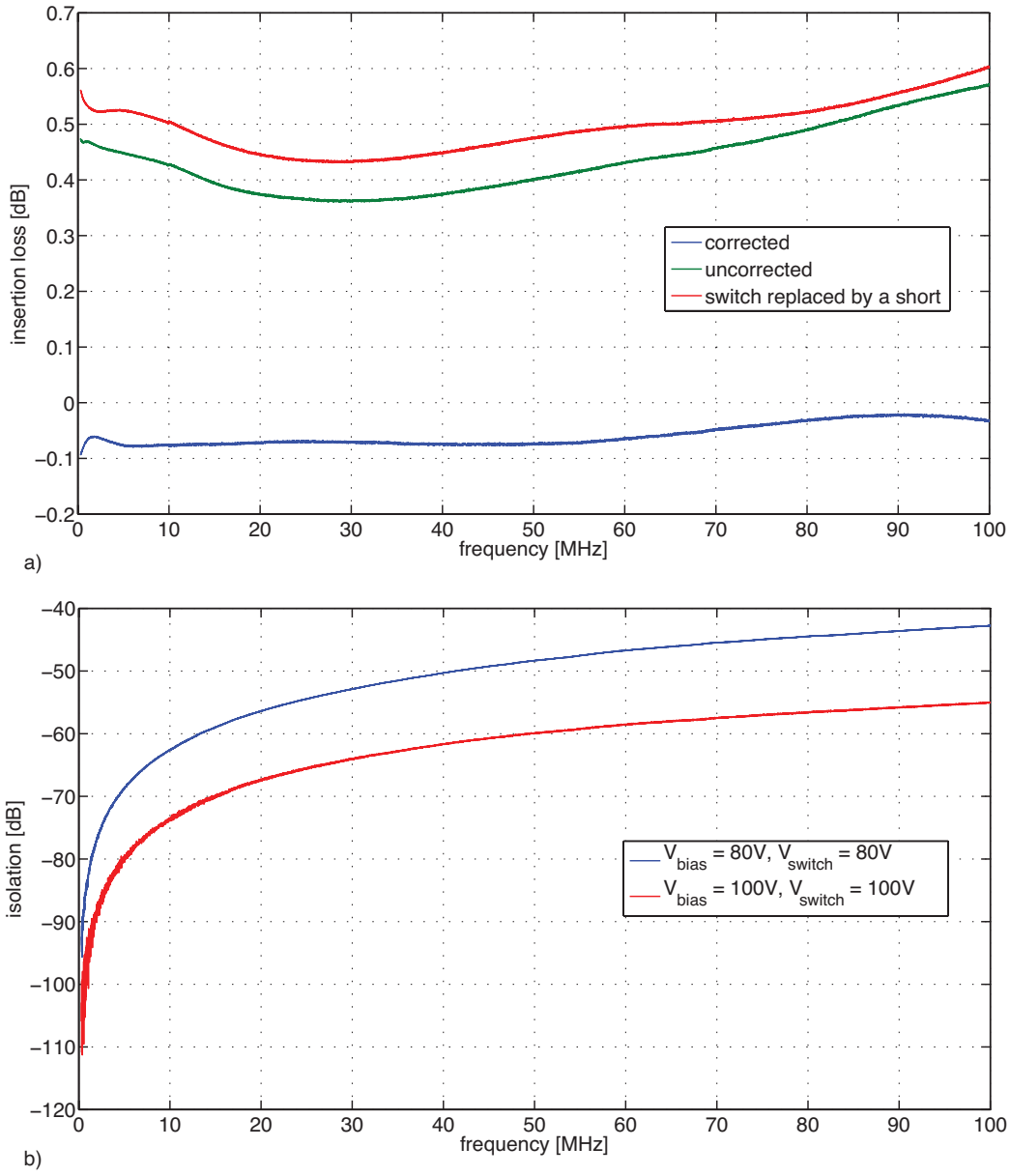

Figure 5.8.: Piezo switch RF performance at 4.2 K. a) Switch in default closed position $V_{\text{switch}} = V_{\text{bias}} = 0\,V$ with and without correction as well as the reference trace (red) in order to correct the measured insertion loss (green). b) Switch in open position for $V_{\text{switch}} = V_{\text{bias}} = 80$ V and 100 V.

6. Cryogenic Detection System

6.1. Cryogenic Amplifier Design and Component Selection

This section describes the design and implementation of a cryogenic low-noise amplifier which together with a tuned circuit gives a non-destructive particle detection system for ions confined in a Penning trap (see chapter 4). The amplifier design requirements are:

- high input impedance in order not to degenerate the quality factor;
- low-noise in order not to heat the stored particles;
- low power consumption[1] of about 10 mW and small in size;
- compatibility with ultra-high vacuum and cryogenic temperatures.

Figure 6.1 shows the equivalent circuit of the detection system including the resonator and the amplifier with its noise sources. The equivalent input noise of the amplifier is modeled as voltage noise source (e_n) and current noise source (i_n), and the input impedance is represented by R_{in} and C_{in}.

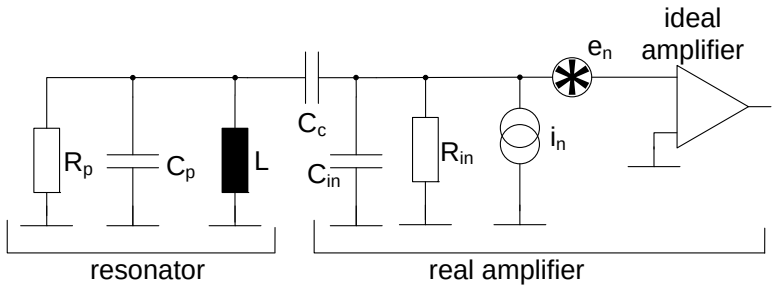

Figure 6.1.: Simplified equivalent circuit of the detection system operated at 4.2 K.

[1] The total power dissipation in the 4.2 K environment of the AEgIS experimental setup is about 100 mW and 10 % are accounted for the amplifier.

As a consequence of the first point in the list, there is no chance to use bipolar transistors for high input impedance amplifiers in the range of at least several MΩ. The next limitation is given by the ambient temperature of 4.2 K or below, since most semiconductors are silicon (Si) based and they are not operable at such low temperatures. Si is known to experience insufficient amounts of available charge carriers – so-called freeze-out effect – when cooled below 40 K [56]. The reason for the (charge carrier) freeze-out of Si is a high band-gap (at low temperatures) in combination with the reduced thermal energy for dopant ionization. Thus, "good" transistor candidates for the amplifier input stage are field field effect transistors (FETs) based on material with a low band-gap at cryogenic temperatures. Gallium arsenide (GaAs), for instance, is a material with a low band-gap and it was shown that GaAs FETs[2] are operable at 4.2 K and below [56]. Using a FET as an impedance transformer leads to a common-source amplifier design. This invokes two additional parameters concerning the choice of the transistor which is a low input capacitance C_{gs} in order not to put additional capacitive load to the tuned circuit (along with detuning) and a low feed-back capacitance C_{dg} in order not to feed back noise to the Penning trap. The first transistors tested in amplifier prototypes were single gate GaAs FETs ATF 35143 (Avago). These transistors are known to work well at cryogenic temperatures and their performance is promising to build an amplifier satisfying the above mentioned requirements [88]. The ATF 3x143 series transistors are microwave devices working at several GHz frequency. Furthermore, they are extremely electrostatic discharge (ESD) sensitive and already small feed-back loops lead to auto-oscillation. For instance, simple DC current-voltage (IV) measurements on standard RF-4 PCBs lead to auto-oscillation. Hence, special care has to be taken in the design of PCBs to provide short paths without loops to ground (GND) for HF signals. Another important design rule is to minimize the inductance connected to the source lead of the transistor. A systematic analysis of how to prevent oscillation of HF semiconductor devices is given in reference [89]. The ATF 35143 turned out not to be suitable for a transimpedance amplification stage directly coupled to the tuned circuit due to high input capacitance (Miller effect). Eventually, two less ESD sensitive dual-gate GaAs FETs were chosen, namely the NE25139 (NEC) and the CF739 (Siemens). Both transistors are operable at cryogenic temperatures and suitable for low-noise applications [56]. The transconductance g_m of the device was chosen as a figure of merit in order to find a suitable operation point and is defined as the ratio of the drain-to-source current (I_{ds}) change to the gate-to-source voltage (V_{gs}) change (see Figure 6.2):

[2]The term FET is used in this thesis generically, also for heterostructure FETs (HEMTs or MODFETs).

$$g_m = \frac{\Delta I_{ds}}{\Delta V_{gs}}. \tag{6.1}$$

Figure 6.3 shows the transconductance (calculated from the IV-curves) of the two transistors for 290 K and 4.2 K. The positive threshold voltage shift (see Figure 6.2) of the GaAs HEMTs (CF739 shows this effect more significantly) at low temperature is typical and involves several effects including charge trapping and the piezoelectric effect [56]. Furthermore, g_m of the GaAs FETs is either slightly increased (NE25139) or decreased (CF739) upon cooling. The IV-curves were measured with source monitor units (SMUs, Keithley 2400) connected to the cryogenic measurement setup described in A.1.2. In order to estimate the input impedance of the transistors, simple DC resistance measurements at room temperature are sufficient. Systematic measurements of equivalent input noise voltage (e_n), DC input impedance ($R_{\mathrm{in,DC}}$) and input capacitance (C_{in}) and the feed-back capacitance (C_{gd}) were carried out in [40] and the result is that the NE25139 transistor is slightly better (see Table 6.1) than the CF739 as an amplification stage directly coupled to the resonator. Another reason for the choice of the NE25139 is the higher gain at lower power consumption when operated at 4.2 K (see Figure 6.4).

transistor	C_{in} [pF]	$R_{\mathrm{in,DC}}$ [MΩ]	C_{gd} [pF]	e_n [nV/Hz$^{0.5}$]
NE25139	0.95	48	0.03	0.83
CF739	1.1	52	0.055	0.85

Table 6.1.: Overview of transistor parameters measured at 290 K. For details see text. (data taken from [40])

A two stage amplifier design was selected in order to have a first high input impedance stage with high gain and a second (buffer) stage for matching to 50 Ω. The amplification stage was chosen as a common source topology with the second gate of the transistor in cascode. The cascode amplifier provides improved electrical decoupling (very small C_{gd}) and higher input to output isolation than an amplifier without cascode [90]. Moreover, the cascode eliminates the Miller effect and the amplifier stage has higher stability due to the reduced back-action from the drain to the gate. The buffer stage was implemented as source follower (common drain amplifier) to provide unity gain and about 50 Ω output impedance. Figure 6.5 shows the electrical circuit diagram of the two amplifier stages including the component values. The coupling capacitance C_c plays a very important role since it is the interface between the tuned circuit and the amplifier and its value determines the coupling strength between them. Therefore, the coupling capacitor has to be a low-loss device (also called high-Q), thus a multi-layer ceramic capacitor from

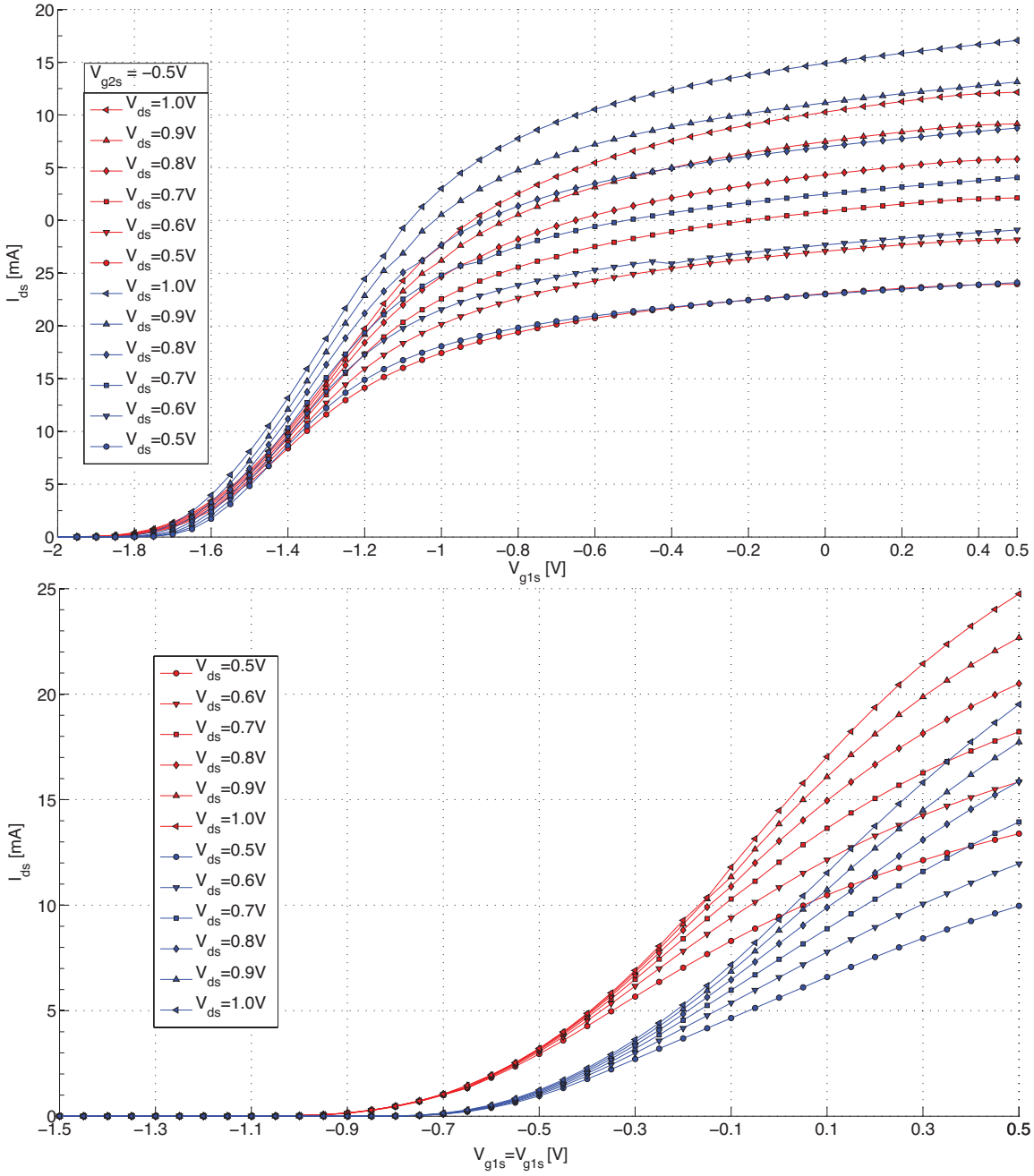

Figure 6.2.: IV-curves of the GaAs FETs NE25739 (top) and CF737 (bottom) at 290 K (red) and 4.2 K (blue).

Johanson-Techchnology (S-Series) with NP0 temperature characteristic was chosen. For the evaluation of the amplifier performance, C_c = 10 nF was chosen in order provide

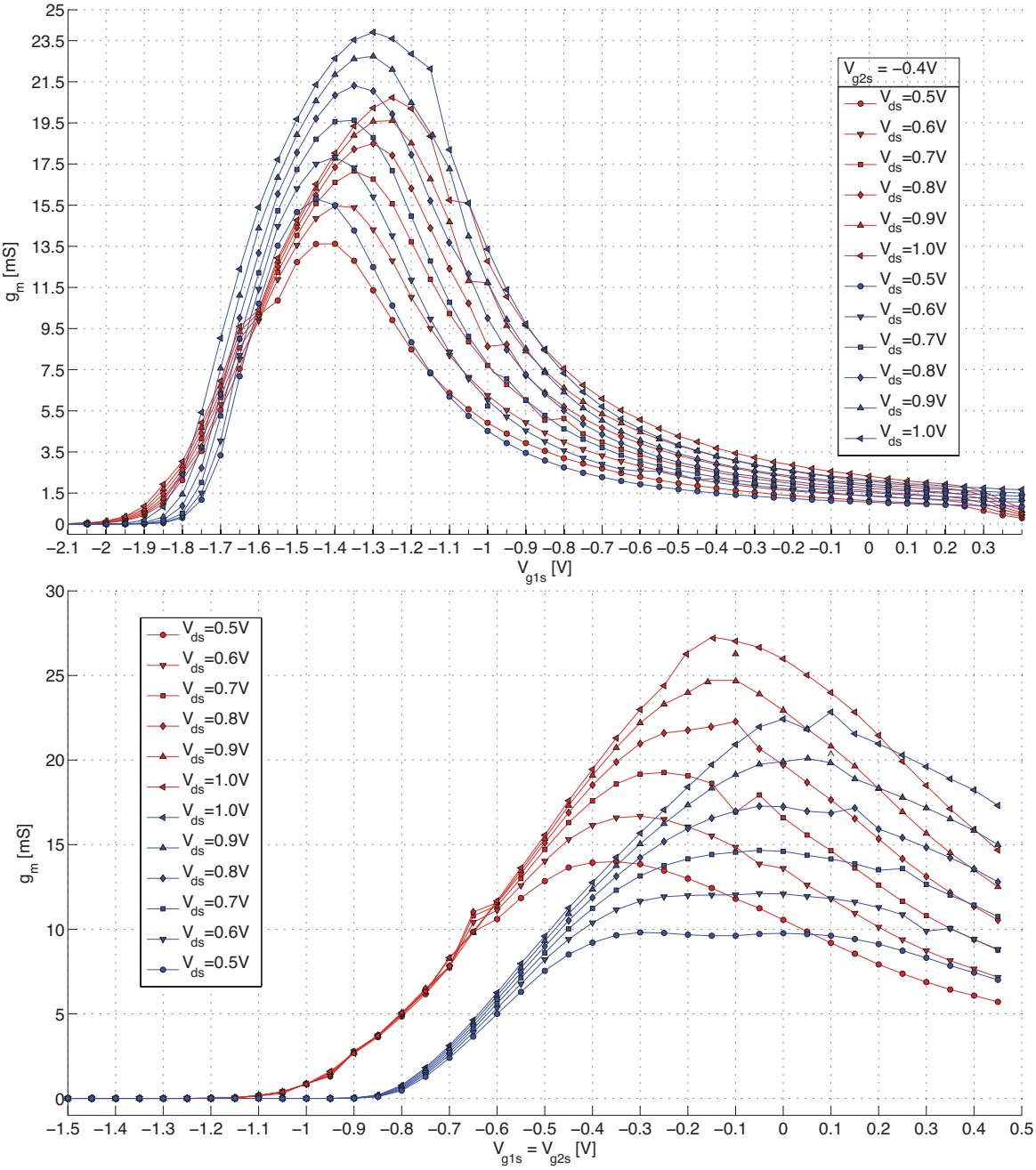

Figure 6.3.: Transconductance g_m as a function of the gate-to-source voltage (V_{gs} of GaAs FETs NE25139 (top) and CF739 (bottom) at 290 K (red) and 4.2 K (blue).

a low impedance path at 20 MHz. The amplifier input was 50 Ω terminated to avoid reflections within the 50 Ω measurement environment, hence the measured voltage gain

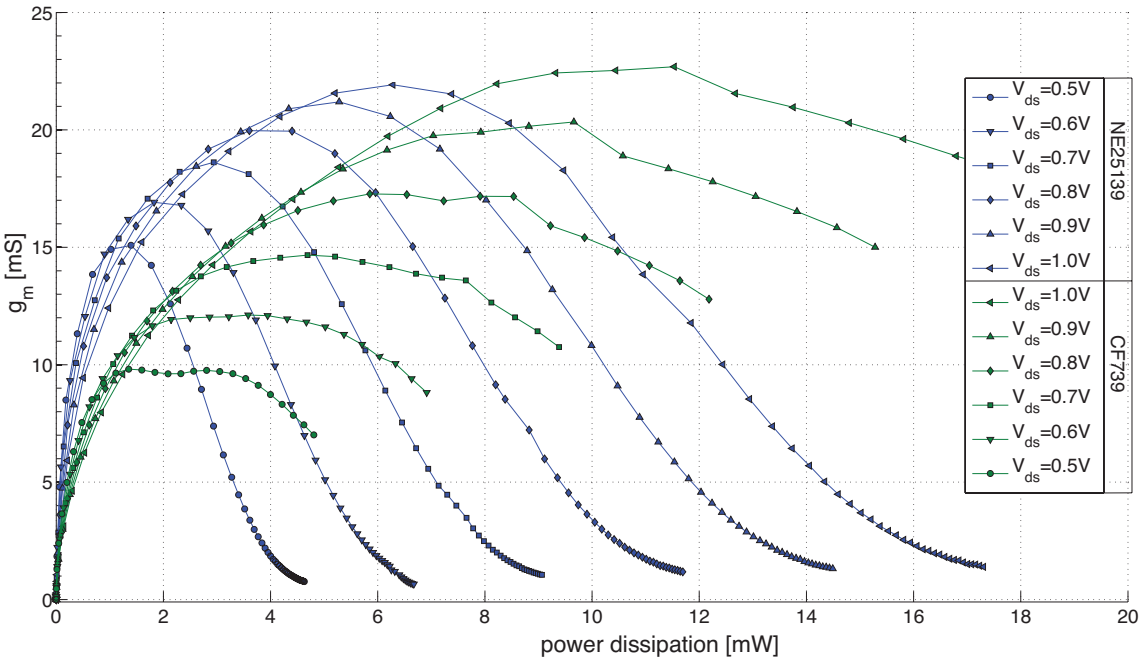

Figure 6.4.: Transconductance g_m as a function of the power dissipation for GaAs FET NE25139 (blue) and CF739 (green) at 4.2 K.

values have to be corrected by +6 dB. The theoretical voltage gain $G_{v,1}$[3] of the first stage is given by

$$|G_{v,1}| \approx g_m \left(\frac{R_d r_{ds}}{R_d + r_{ds}} \right) \tag{6.2}$$

with R_d being the drain resistor and r_{ds} for the differential drain-to-source resistor. Choosing $R_d = 910\,\Omega$ and deducing r_{ds} from the IV-curves (drain voltage sweep at constant gate bias; not shown) the theoretical voltage gain is obtained $|G_{v,1}| \approx 13.65 = 22.7$ dB. The buffer stage gain with drain resistor $R_d = 16\,\Omega$ and source resistor $R_s = 620\,\Omega$ is calculated by

$$|G_{v,2}| \approx \frac{g_m R_L}{g_m R_L + 1} \text{ with } R_L = \frac{R_s(R_d + r_{ds})}{R_d + r_{ds} + R_s} \tag{6.3}$$

[3]The common-source amplifier is inverts the input signal ($G_{v,1} < 0$), hence only the absolute value is written.

and results in $G_{v,2} = 0.85 = -1.4$ dB. Hence, the theoretical overall voltage gain ($G_{\text{cryo-amp}}$) of the cryogenic amplifier is about 20 dB at an adequate operating point. The amplifier is housed in a metal shield, and commercial feed-through filters (FF1 to FF5; Tusonix) are connected to every biasing pin in order to reduce HF noise. The low frequency (LF) noise is reduced by using 1 µF foil capacitors (ECPU[4], Panasonic) in the biasing network.

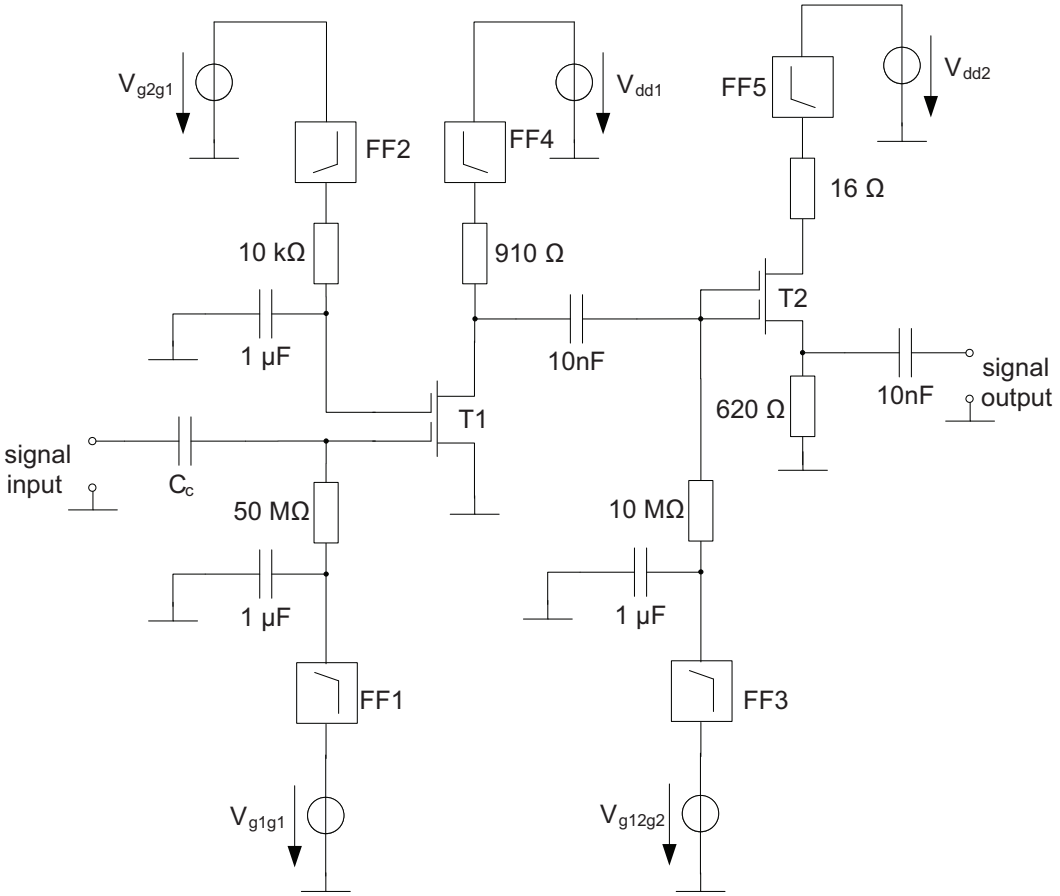

Figure 6.5.: Electrical circuit diagram of the two stage cryogenic amplifier including feed-through filter (FF1 to FF5) on every bias lead. T1 is a NE25139 and T2 a CF739 transistor.

Since the amplifier is coupled to the high quality factor tuned circuit, the same loss reduction considerations apply for the amplifier design. Thus, the printed circuit board (PCB) of the amplifier has to have low dielectric loss. A good choice of the base material is a high-performance RF laminate, therefore Arlon DiClad880 teflon (PTFE) laminate

[4]Foil capacitors as ECPU, ECHU and PPS are known not to degenerate significantly the capacitance at cryogenic temperatures [45].

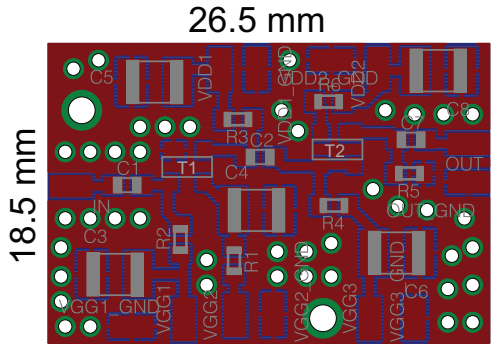

Figure 6.6.: PCB layout of the cryogenic amplifier.

was chosen. The laminate is 1.52 mm thick with a top and bottom layer of 70 µm copper. It has a dielectric constant of 2.17 and a dielectric loss tangent[5] $\delta_{\mathrm{DiClad880}} = 0.0008$ at 1 MHz. Figure 6.7 shows a photograph of the amplifier housed in a metal box. The PCB was made by milling (ProtoMat S63, LPKF Laser & Electronics AG) the copper surface of the low-loss laminate in order to avoid possible chemical residuals from etching which could reduce the RF performance. Numerous vias for a proper ground connection on the board were inserted (see Figure 6.6) manually (LPKF EasyContac). Special care had to be taken while populating the PCB with components since the very thin copper structures tend to detach[6] from the surface especially when heated during the solder process.

Different operation points (op) of the low-temperature amplifier are shown in Table 6.2. They are used to identify specific properties, such as high-Q, low noise or high gain. Figure 6.8 shows the amplification in dB as a function of the frequency for the op 1 condition shown in Table 6.2. The amplifier power dissipation is less than 10 mW for a voltage gain of about 18.4 dB at 20 MHz. These values are within the specifications and in agreement with the theoretical value.

The noise spectrum of the cryogenic amplifier taken in op 2 condition is shown in Figure 6.9. In order to obtain the equivalent input noise voltage (e_n) the amplifier input is shorted (compare Figure 6.1) and the noise at the output is measured with a spectrum analyzer (SA; Agilent N9010A). The measured output noise is given by

[5]The dielectric loss tangent is a quantity which describes the RF quality of a material and is defined as $\tan(\delta) = 2\pi C_s R_s$ being the ratio of reactive power (in C_s) to dissipative power (R_s). This expression defines the loss tangent for a series equivalent circuit.
[6]Traces on the PCB were disconnected upon cooling.

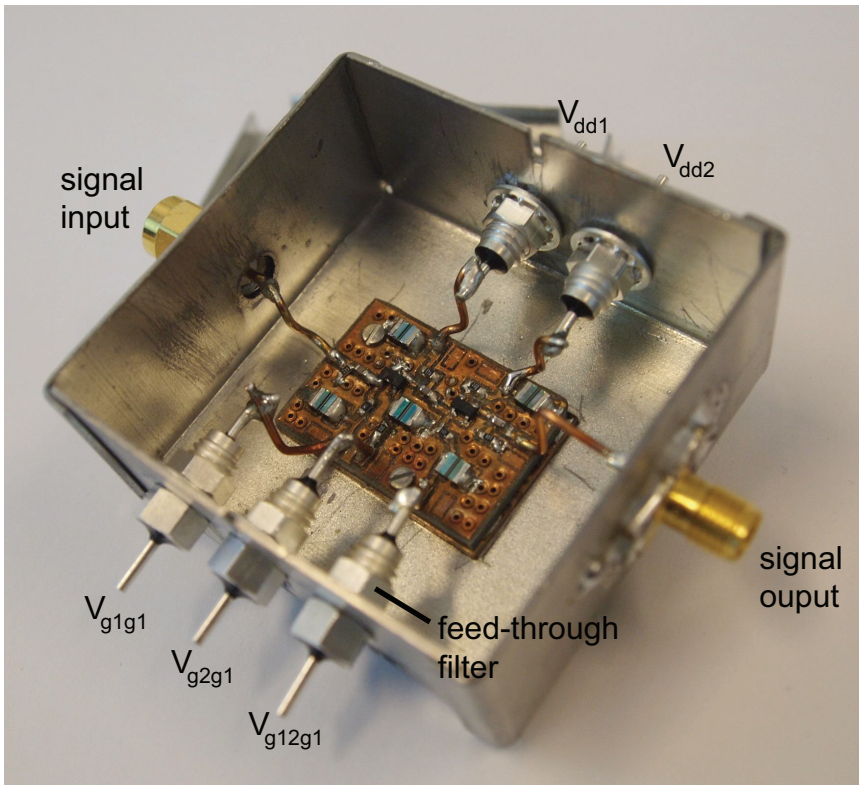

Figure 6.7.: Photograph of the cryogenic amplifier in a shielding box.

$$e^2_{\text{meas,out}} = (e_n G_{\text{cryo-amp}})^2 + e^2_{\text{SA}} \tag{6.4}$$

assuming independent noise sources where e_{SA} is the SA noise and $G_{\text{cryo-amp}}$ the total cryogenic amplifier gain. Since $G_{\text{cryo-amp}}$ and e_{SA} were measured, the equivalent input noise was calculated by solving equation (6.4) for e_n. Note that there was no current noise i_n measurement done, since the contribution to the amplifier noise is marginal [91].

6.2. Measurement Results of the Cryogenic Detection System

The detection system, consisting of the cryogenic amplifier connected to the high quality factor tuned circuit, has to be stable. Therefore, the superconducting resonator (including coil # 10) described in Section 4.1 was connected by means of a coupling capacitor

op ID	V_{g1g1} [V]	V_{g2g1} [V]	V_{g12g2} [V]	I_{dd1} [mA]	$G_{\text{cryo-amp}}$ [dB] @20 MHz
op 1	-1.45 V	-0.45	1.2	1.22	18.4
op 2	-1.54 V	-0.7	1.2	1.47	18.8
op 3	-1.34 V	-0.7	1.2	2.64	16.3
op 4	-1.80 V	-0.7	1.2	0.12	-

Table 6.2.: Cyogenic amplifier bias configuration (operation point; op) at 4.2 K. $V_{dd1} = 3$ V and $V_{dd2} = 2.5$ V and the resulting $I_{dd2} = 2.29$ mA were constant in all operation points.

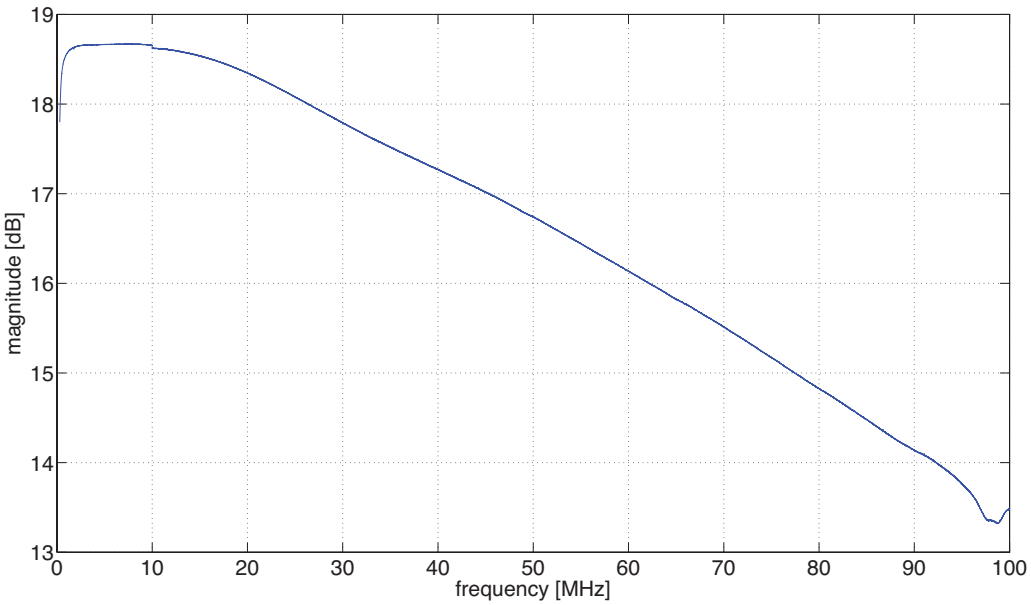

Figure 6.8.: Cryogenic amplifier voltage gain spectrum measured at 4.2 K.

$C_c = 1$ pF to the cryogenic amplifier described in the last section. At this point, the system may tend to oscillate due to small feed-back loops. During the operation of the detection system at 4.2 K no stability problem was identified. Figure 6.10 shows the spectrum of the detection system at 4.2 K with -20 dBm excitation loosely coupled to the resonator. The amplifier was in op 3 (see Table 6.2) condition during this measurement and the spectrum was evaluated with a vector network analyzer (VNA; Agilent E5061B).

The next step was to evaluate the quality factor of the resonator and its dependence on the amplifier bias. Therefore, the gate 1 voltage of the input stage V_{g1g1} (see Figure 6.5) was chosen as the parameter to vary since many other important parameters, such as

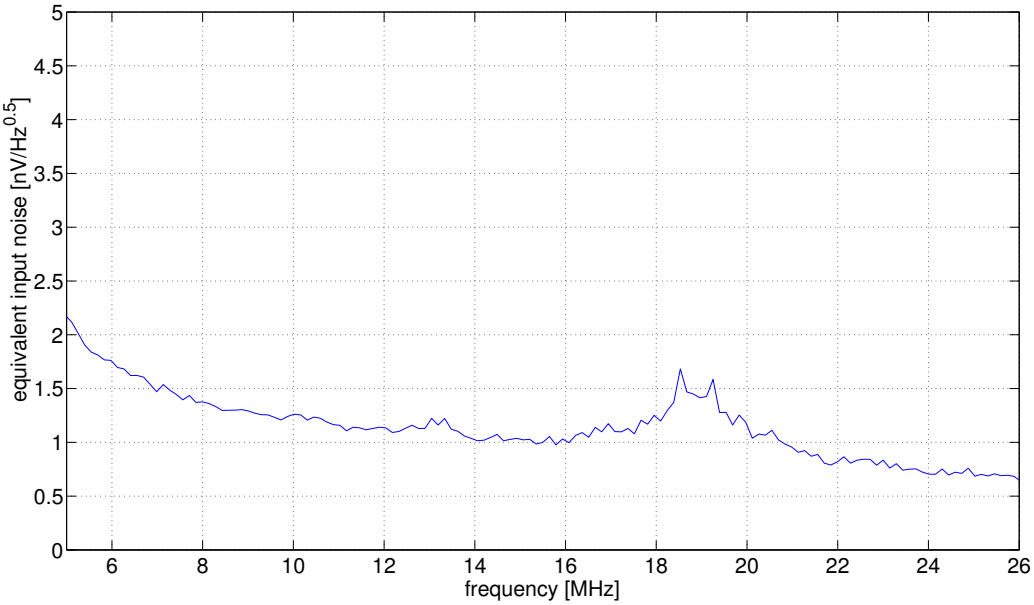

Figure 6.9.: Equivalent input noise spectrum in the frequency range of interest. Note that the noise peak between 18 and 20 MHz is a spurious signal coupled to the measurement setup. The same peak was measured with an antenna in the laboratory.

amplification and input capacitance, are directly influenced. A second order effect is the influence on the quality factor of the resonator. The effective parallel resistance R_p of the tuned circuit at resonance is defined as

$$R_p = 2\pi\nu_0 L Q_L \quad \text{with} \quad Q_L = \frac{\nu_0}{\Delta\nu} \tag{6.5}$$

where $2\pi\nu_0$ denotes the angular resonance frequency, $\Delta\nu$ the 3 dB bandwidth and Q_L the loaded (effective) quality factor of the resonator. Figure 6.11 shows Q_L and the corresponding R_p as a function of V_{g1g1}. The measured data can be explained by coupling negative feed-back to the resonator [92]. The feed-back loop is given by the drain-to-source resistance (R_{ds}) by means of the drain-to-gate C_{gd} capacitance. This feed-back, although tiny, reduces the effective quality factor of the tuned circuit by reducing the input impedance of the amplifier.

Since the resonator contains a superconducting coil, its quality factor is strongly dependent on temperature, especially around the so-called critical temperature where the

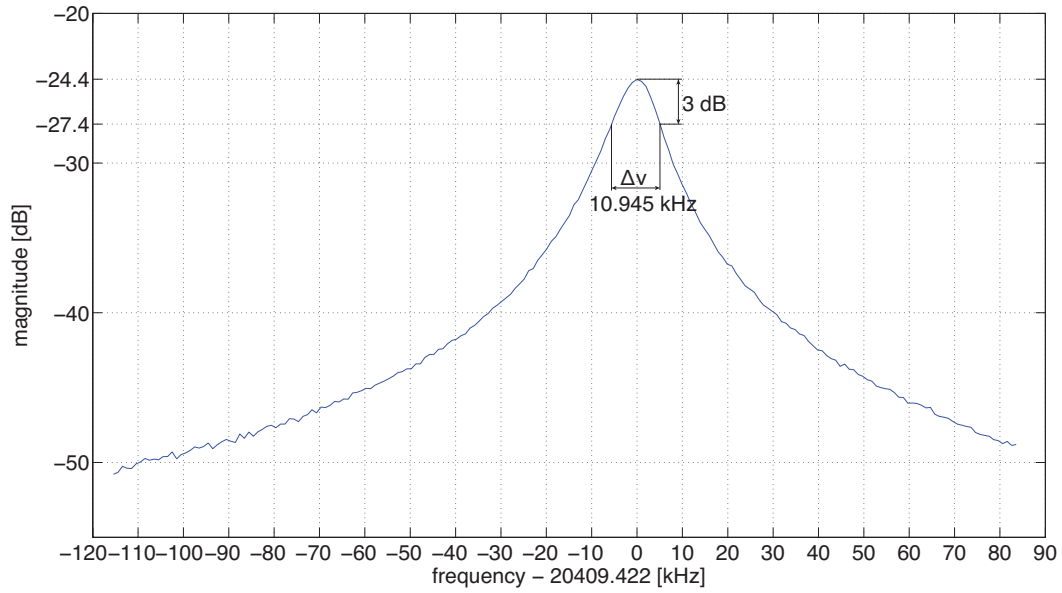

Figure 6.10.: Spectrum of the detection system. The x-axis is normalized to the resonance frequency ν_0. The arrows show the measurement of the (loaded) quality factor ($Q_L = 20409.422\,\text{kHz}/10.945\,\text{kHz} \approx 1864$).

niobium-titanium (NbTi) wire becomes superconducting. Figure 6.12 shows the effective quality factor Q_L and the corresponding effective parallel resistance R_p as a function of temperature. The amplifier was operated in op 4 condition (see Table 6.2), hence there should not be a heating effect of the amplifier on the tuned circuit. However, there is a temperature gradient between the superconducting coil and the measured temperature due to the difference of roughly 1 K between the measured and the theoretical critical temperature of NbTi, which is 9.2 K.

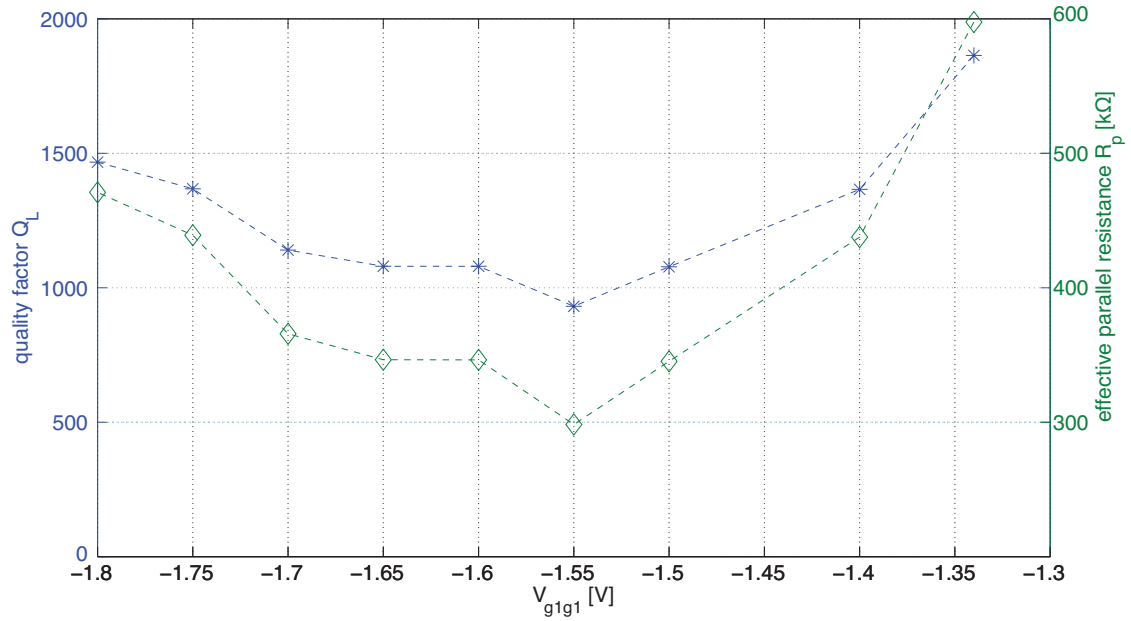

Figure 6.11.: Quality factor and equivalent parallel resistance of the detection system as function of the gate 1 voltage V_{g1g1} of the amplification stage.

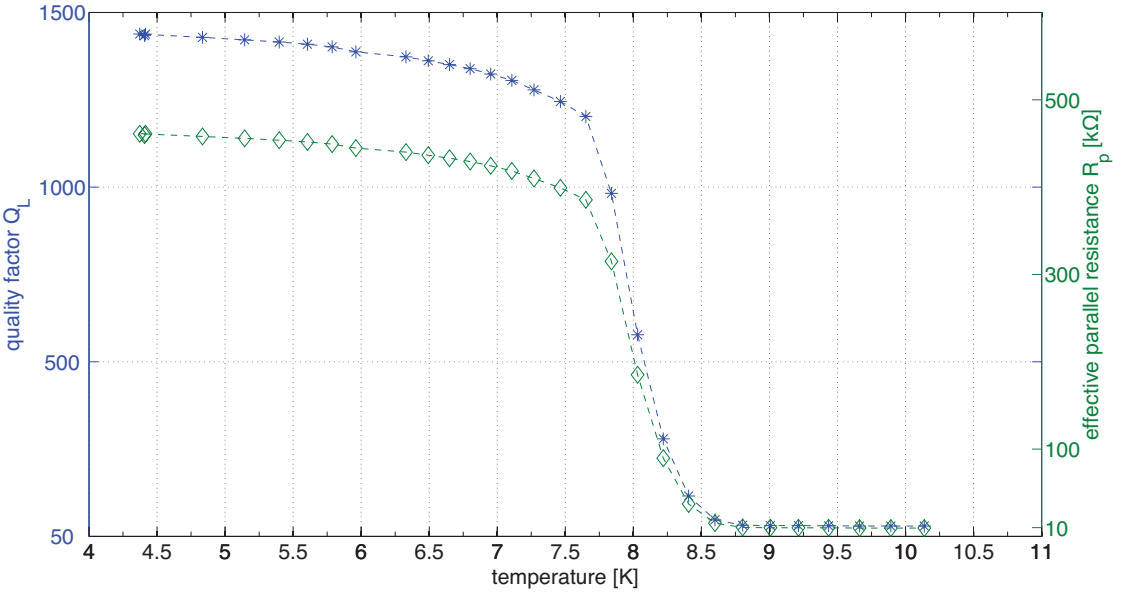

Figure 6.12.: Quality factor and equivalent parallel resistance of the detection system as a function of temperature.

7. Summary and Outlook

In this thesis, research on electronic devices operable at 4.2 K temperature and in high magnetic field was presented. The design, implementation and performance of a highly sensitive, non-destructive particle detection system was shown. The equivalent input voltage noise of the amplifier contained in the detection system was ~ 1 nV/Hz$^{0.5}$ at 20 MHz. The resonator on top of this system develops a quality factor of almost 2000 with the connected amplifier.

A new possibility of replacing the resonator made of a superconducting coil with a crystal resonator was demonstrated and the system's performance was presented. The crystal resonator shows higher quality factor values than the coil, hence this option is promising for further research concerning resistive cooling of charged particles in Penning traps.

The development of a new piezoelectric switch was presented since there is no satisfying commercial low-resistance DC-contact RF switch available which is operable at 4.2 K and in a magnetic field of at least 0.5 T. This piezo switch showed very low insertion loss of less than -0.1 dB within a bandwidth of 100 MHz when operated at 4.2 K. This type of switch could also be used to mechanically disconnect and connect parts from one another. Furthermore, the switch was designed in such a way that even biasing networks e.g. for amplifiers may be switched.

Cryogenic low-pass filters were designed and their low temperature performance was shown. These filters offer the possibility of bypassing fast voltage pulses when needed and their filter performance is better compared to a commercial product [55].

Every electronics prototype presented in this thesis has the potential for further improvement. The equivalent input noise of the detection system could be reduced through noise matching between the resonator and the cryogenic amplifier. Furthermore, the buffer stage consumes in access of 50% more power than the amplification stage. This could be improved by replacing the GaAs FET CF739 with a NE25139 or a voltage follower using bipolar transistors since they have higher gain and lower output impedance [90]. In the future, when the AEgIS apparatus is going to be extended by a dilution refrigerator in

order to reduce the base temperature of the ultra-cold trap to 100 mK, the cryogenic amplifier may be split into two parts. The first one could be a buffer, made of GaAs JFETs with a very high input impedance and dissipating less than 10 μW[1]. The second part could be the same cryogenic amplifier as shown in this thesis, being thermalized to an intermediate temperature stage at 1.5 K or directly at 4.2 K. The buffer and the amplifier could be connected by means of a superconductor in order to reduce the heat load at the 100 mK stage.

The piezoelectric switch may be further miniaturized by using a small piezo bender made of different material in order not to reduce substantially the deflection at low temperature. The switch presented in this thesis was made of PIC251 which has a factor of about 6 less deflection than PIC255 at 4.2 K. Hence, an improved switch could be made smaller by using PIC255 material without reducing its deflection.

The cryogenic low-pass filter is rated for electrode bias voltages of up to 250 V. If necessary, the filter could be redesigned by using components rated for much higher voltages, in the range of kV, have to be used[2]. Since the axial frequency of electrons stored in a Penning trap is less than 10 MHz using an electrode bias of 250 V, the detection system could be tuned to lower frequencies by means of additional capacitance connected to the tuned circuit. In order not to degrade the quality factor of the resonatore, it is important to use low-loss capacitors or even semi-rigid coaxial cables made of highly conductive copper with teflon insulation. Since the amplifier incorporates GaAs FETs, the noise floor is not expected to increase significantly down to ∼1 MHz [40, 93, 94]. Below this frequency 1/f noise may degrade the performance of the detection system and different transistors have to be used. The aforementioned GaAs JFETs could serve as low-noise input stage at low frequencies because they were designed for 1/f corner frequencies below 1 kHz [95].

[1] The estimated total power dissipation of the dilution refrigerator is about 100 μW, and 10% are allocated for the amplification/buffer stage.

[2] There are SMD capacitors available which are rated up to several kV (e.g. 3 kV Kemet GRM Series). The same applies for SMD resisitors (e.g. 1.5 kV ohmcraft HVC Series)

A. Appendix

A.1. Cryogenic Measurement Setup

A.1.1. Cryogenic Measurement Setup with LHe

All cryogenic measurements within this thesis were performed with the same setup which consists of a cryostat, a pressurized helium bottle, a transfer line, the rack with instrumentation and measurement devices, and an inset where the device under test (DUT) was mounted (see Figure A.1) except the piezo switch measurement and the detection system performance. The measurements were conducted in the cryo lab facility at CERN.

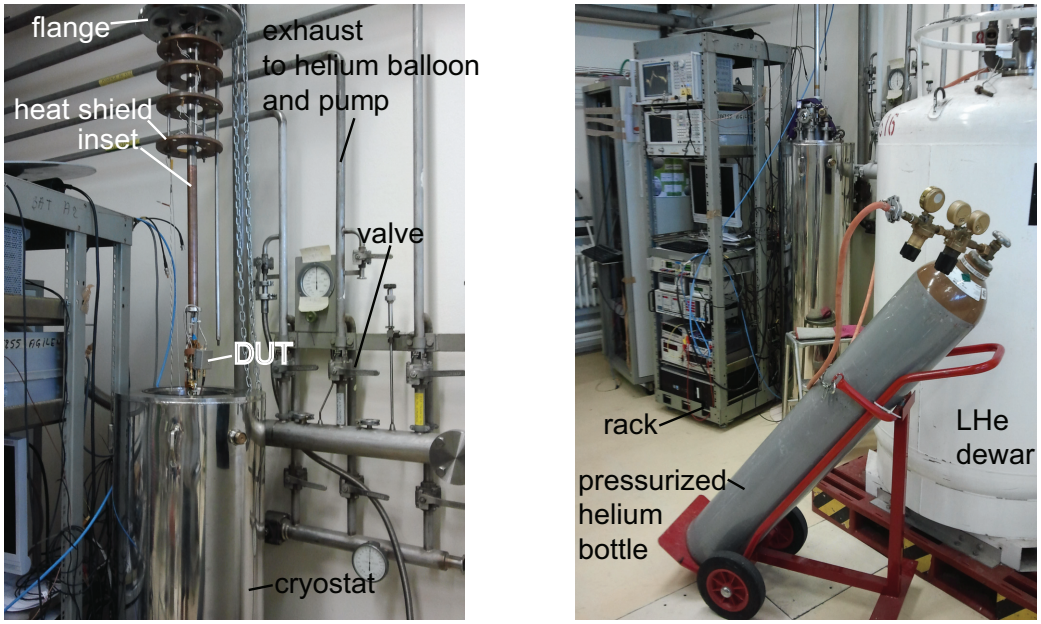

Figure A.1.: a) Close-up of the inset. b) Photograph of the cryogenic measurement setup.

A typical measurement scenario starts with the mounting of the device under test (DUT) onto the inset and connecting its wires and cables to the measurement equipment in the

rack. Note that the inset is fixed in a movable manner to the flange which seals the cryostat. The next step is to insert the inset into the cryostat and to close the cryostat by bolting the flange onto it. Now, the cryostat has to be evacuated by means of a rotary pump and flushed with helium gas coming from a balloon[1]. Valves, shown in Figure A.1 a), are used to connect/disconnect the croyostat to/from the balloon and pump. After the flushing of the cryostat with helium gas, the setup is ready for the liquid helium (LHe) transfer. Figure A.2 shows a sketch of the setup including its main parts for providing the cryogenic measurement environment.

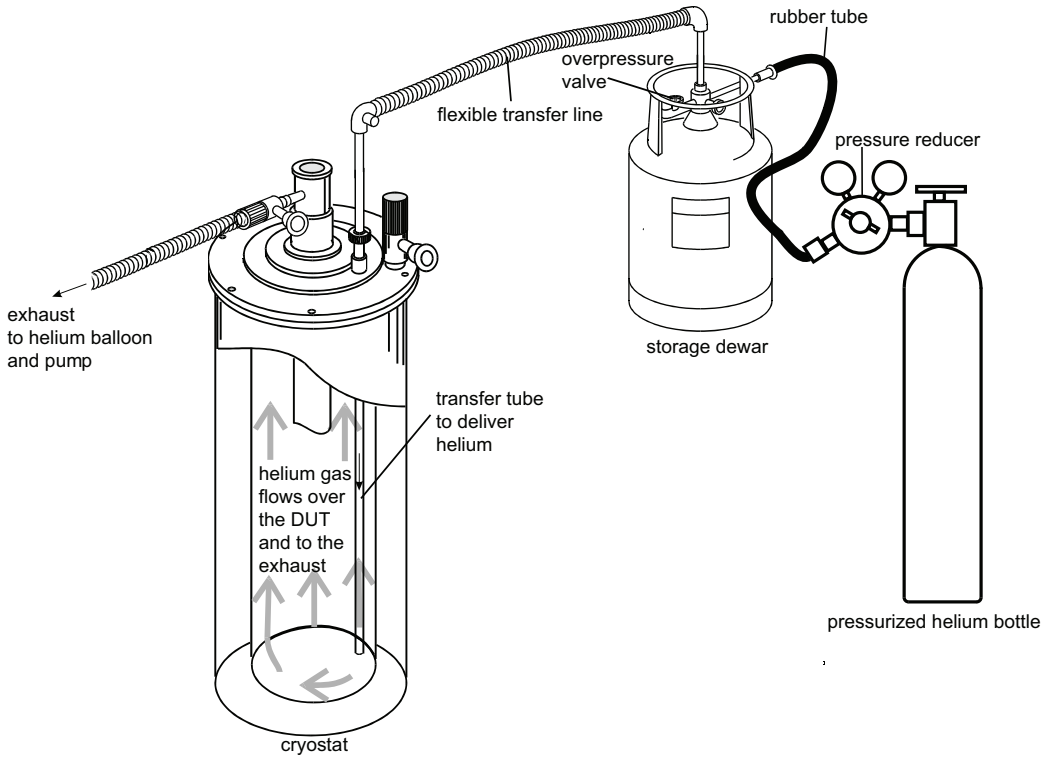

Figure A.2.: Schematic of the cryogenic setup.(Figure adapted from [96])

In order to do a LHe transfer, the cryostat is connected with a flexible transfer line to the storage dewar, which contains the LHe. To start the LHe transfer, the storage dewar is pressurized by means of a helium bottle containing highly compressed helium gas at room temperature. The pressurized helium gas pushes then the LHe through the transfer

[1]The balloon for helium recuperation has a volume of several m^3 and is placed in a separate building outside of the cryo lab.

line into the cryostat. The gas and LHe flow are symbolized by arrows in Figure A.2 during the transfer. The transfer speed is regulated by the pressure reducer connected to the helium bottle. An overpressure of about 150 mbar was the typical setting at the pressure reducer. After having reached the desired LHe level inside the cryostat, the transfer is interrupted by disconnecting the helium bottle and removing the transfer line. The inset and the DUT mounted on it are now thermalized to 4.2 K and the setup is ready for measurements. Note that the temperature inside the cryostat was monitored by means of a Lakeshore thermocoupler (CERNOX) and the LHe level was measured with a level gauge. The entire read-out and measurement equipment was housed in a rack and it was remote-controlled by a personal computer (PC) (see Figure A.1 b) at the bottom of the rack) via the general purpose interface bus (GPIB). Matlab was used for the data acquisition and data post processing and plotting.

A.1.2. Cryogenic Measurement Setup using a Cryo-Cooler

In the above mentioned cryogenic measurement setup the thermalization of the DUTs was not important since they were immersed in LHe. The measurement of the piezo switch and the detection system was performed using a cryocooler system (SRDK Series; Sumitomo Heavy Industries, Ltd.) in order to reach LHe temperature. The cryo-cooler consists of two main components: a compressor unit (F-50 Series) and a two stage cold head (RDK-408D2), connected to a copper rod for each stage, inside a vacuum chamber. The cryo-refrigeration is based on a Gifford-McMahon cooler, which compresses helium and through the variation of valves in the cold head, between high-pressure and low-pressure helium, a cooling effect takes place. Note that the helium gas in the closed cycle is always at room temperature. Figure A.3 a) shows the measurement setup including the cold head mounted on a 6-way cross connected to the compressor (not shown) with flexible lines (bottom and top left). Figure A.3 b) shows a more detailed view of the parts inside the vacuum chamber (not shown). The vacuum chamber is a stainless steel pipe which is sealed on the bottom with a copper gasket and a DN200 flange and whose top is bolted onto the 6-way cross. In order to reduce the heat load on the second stage, there is an aluminum heat shield (not shown) thermalized to the first stage copper rod. The cryo-cooler is specified for a power load of 40 W at 43 K (first stage) and 1 W at 4.2 K (second stage). Before cool down, the chamber has to be evacuated to a level of about 10^{-4} mbar by means of turbo pump (isolation vacuum). Afterwards, the water cooled compressor is switched on and after about 90 minutes the second stage of the cold head reaches 4.2 K. The pressure is measured by means of a full range pressure gauge (Peiffer)

and is about 5×10^{-8} mbar inside the chamber at this temperature. The DUTs are directly bolted onto the copper body of the second stage and thermal conducting grease is used to avoid temperature gradients between them. The temperature is measured by means of diode temperature sensors (DT-670; LakeShore).

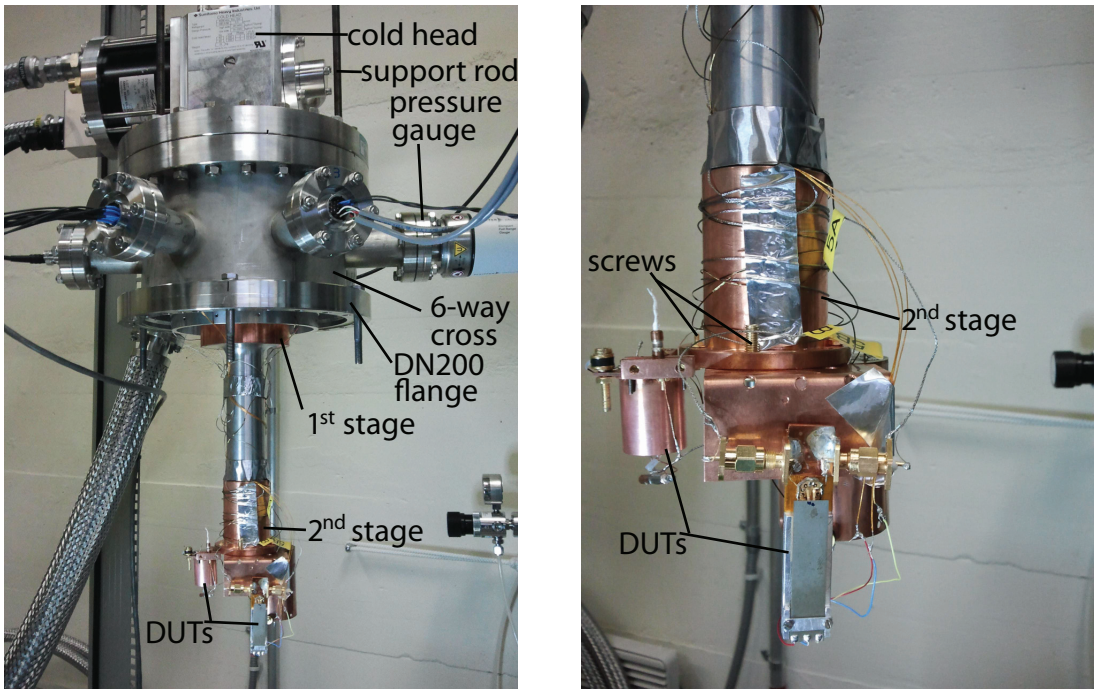

Figure A.3.: a) Photograph of the cryo-cooler measurement setup in order to evaluate device under test (DUT) at 4.2 K. b) Close-up of the photograph of the cryo-cooler measurement setup.

A.2. Setup for Measurements in High Magnetic Fields

In this thesis, results are shown from electronics parts operated in high magnetic field. Unfortunately, these measurements were done at room temperature only, since there was no facility available for cryogenic temperature and high magnetic field. However, the two available room temperature magnets provide a magnetic field strength of about 1 T and 0.5 T respectively. Figure A.4 shows a photograph of the 0.5 T magnet and the measurement setup for the piezo switch. The magnetic field was measured with a gauss/tesla meter (F.W. Bell Model 4048). Multimeter, source monitor units (SMU) and network analyzer are placed on the table in front of the magnet and used as instrumentation.

Figure A.4.: a) Close-up of the magnet bore. b) Photograph of the entire measurement setup for the evaluation of DUTs in high magnetic field.

Massive aluminum blocks were used to support the cables and magnetic parts, for instance clamps or screws, in order to fix them in the magnetic field.

A.3. Simulation of the Cryogenic Low-Pass Filter

The measurement setup including the filter (see Figure 3.4 in chapter 3.2.3) was simulated with with the RF simulation environment Advanced Design System (ADS) from Agilent. The schematic used for the simulation is shown in Figure A.5.

First, the low-pass filter without diodes was simulated. Since the calibration of a network analyzer cannot remove the effect of cable capacitance, the cable capacitance has to be inserted by hand into the model. In our case the cables used in the cryogenic measurement setup add a capacitance of 400 pF to the filter output. The simulation result in Figure A.6 shows very good agreement between simulation and measurement. Note that for changing the filter specification with respect to the temperature of 290 K and 4.2 K only the resistor values were multiplied by a factor of 2.28 (see chapter 3.2.3).

The next step was to add the diodes using the SPICE (Simulation Program with Integrated Circuit Emphasis) diode model [54, 97] with standard parameters for the NXP Semiconductors silicon Schottky diode BAS70 [2]. It turned out that the zero bias junction capacitance C_{j0} and the saturation current I_S are diode model parameters which

[2]Diode SPICE model parameters were taken from `http://www.nxp.com/documents/spice_model/BAS70_04.prm`

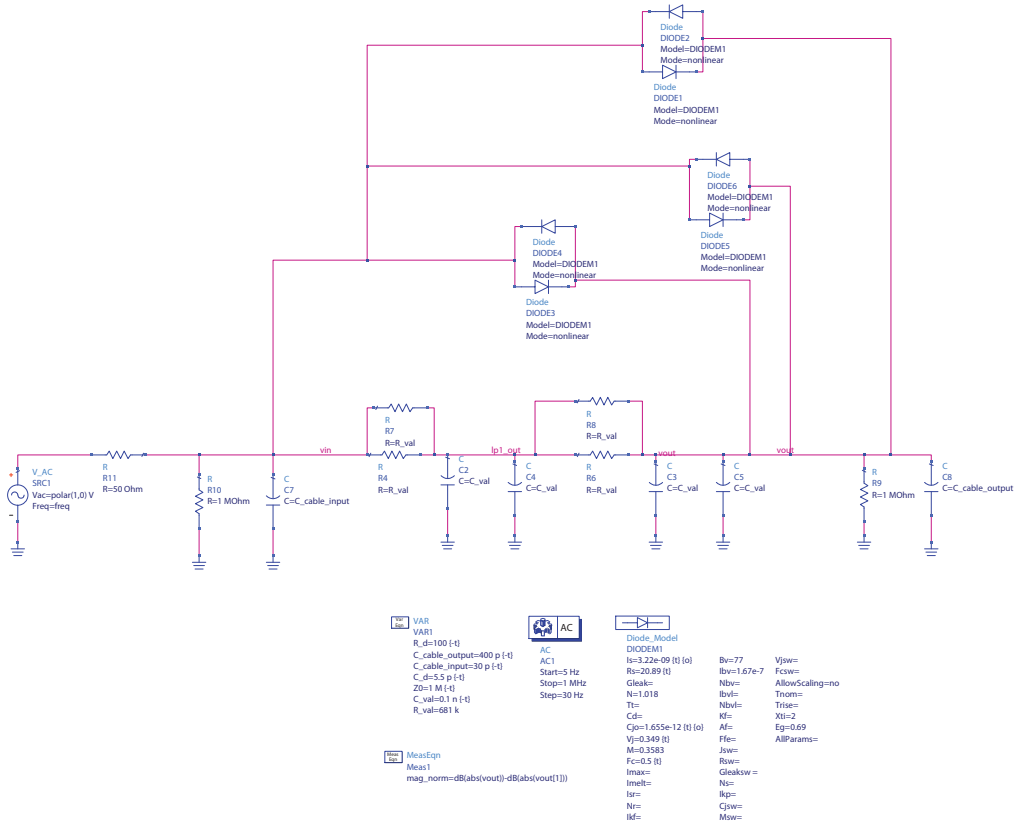

Figure A.5.: ADS schematic of the model used for simulating the cryogenic low-pass filter.

are sufficient to describe and adapt the changes of the filter characteristics in case of putting diodes in parallel to the low-pass filter. The default diode model parameters are $C_{j0} = 1.655$ pF and $I_S = 3.22$ nA and Table A.1 summarizes the parameter values for C_{j0} and I_S in order to fit the measured filter characteristics shown in Figure A.7. Note that both fitted parameters for 290 K and two diode pairs are in excellent agreement with the nominal simulation parameters. The room temperature measurements were done with different cables, thus the added capacitance was 20 pF compared to 400 pF in case of the cryogenic measurement setup.

When cooled to 4.2 K, the diode saturation current and junction capacitance are reduced by several orders of magnitude. This result is in good agreement with the data presented in [98] where silicon carbide (SiC) rectifier diodes were measured down to 77 K. In the same reference the change of other diode parameters with temperature are identified such as the so-called ideality factor n (also called emission coefficient) and the barrier height Φ_B (also called energy gap). These additional parameters may be needed in order to

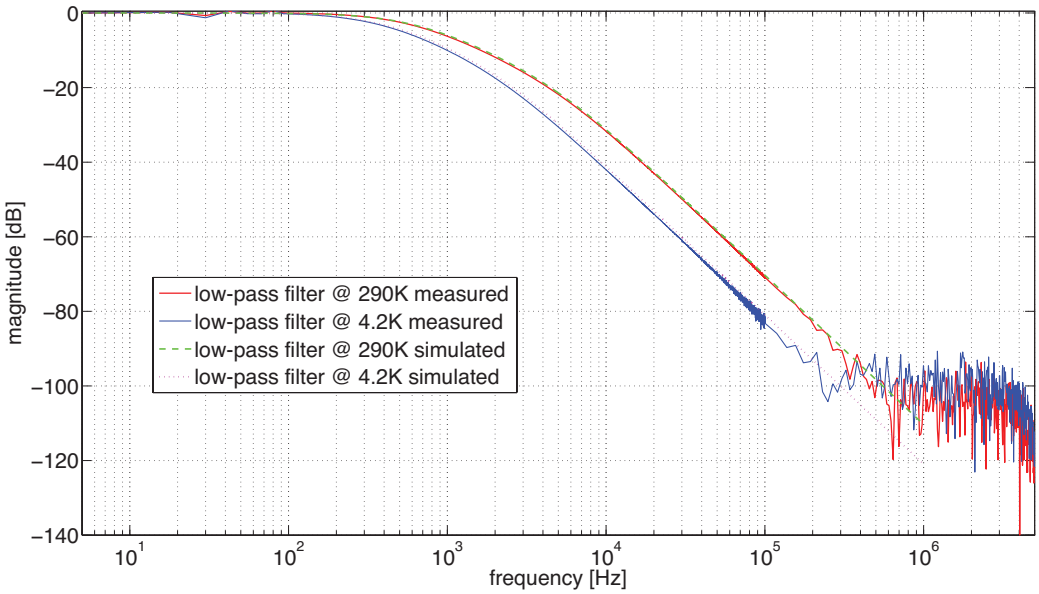

Figure A.6.: Comparison of simulated and measured low-pass filter characteristic for 290 K and 4.2 K.

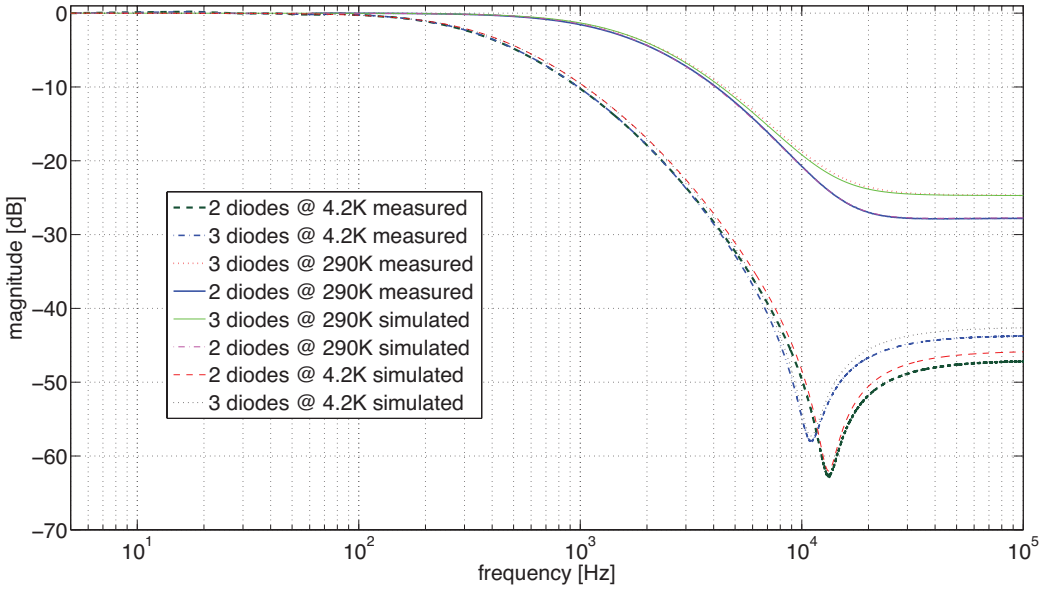

Figure A.7.: Result of simulated and measured nonlinear low-pass filter characteristic for 290 K and 4.2 K and with 2 and 3 diode pairs in parallel.

describe the diode low temperature effects even more accurately. The bottom line of the filter measurement and simulation is that every capacitance has to be accounted for since

our low-pass filter represents a high impedance environment.

temperature [K]	C_{j0} [pF]	I_S [pA]
2 diode pairs		
290.0	1.597	4.461
4.2	0.302	0.076
3 diode pairs		
290.0	1.576	4.169
4.2	0.284	0.050

Table A.1.: Diode fitting C_{j0} and I_S parameters for 290 K and 4.2 K as well as 2 and 3 diode pairs.

A.4. Verification of Quality Factor Calculation with Matlab

The Q-factor calculation from measured reflection coefficient measurement was verified by feeding synthetic data into the calculation framework. The test set data was synthesized with ADS. Figure A.8 shows the simulation model which contains the following parts:

- "Term" is a terminal element with a specified characteristic impedance Z_0 that allows to measure the scattering parameter (S-parameter) and represents the network analyzer in reflection measurement mode.
- An amplifier in order to simulate reduced losses when cooling to 4.2 K with respect to the room temperature calibration of the measurement setup.
- The coupling is realized by means of a coupling capacitor $C_p = 0.2$ pF like in the real measurement setup.
- The tuned circuit equivalent circuit (RLC) is used to define the resonance frequency (LC) and the Q-factor (R).

ADS offers a data save tool which allows to export the simulated values in standardized Touchstone format which is in turn read in with Matlab. Depending on the frequency resolution of the data (measured and simulated) the calculation error was smaller than 5%. The simulation result for a resonator with an unloaded Q of 10^4 is shown in Figure A.9.

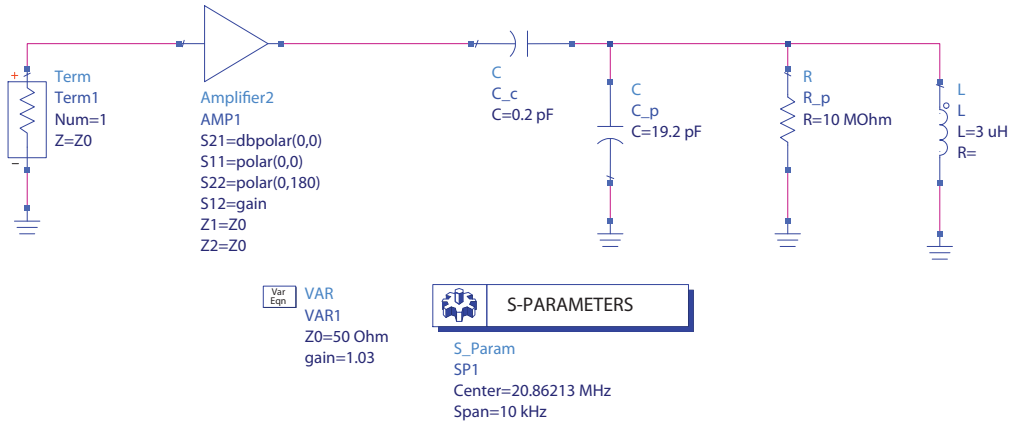

Figure A.8.: ADS simulation schematic in order to generate synthetic resonator data.

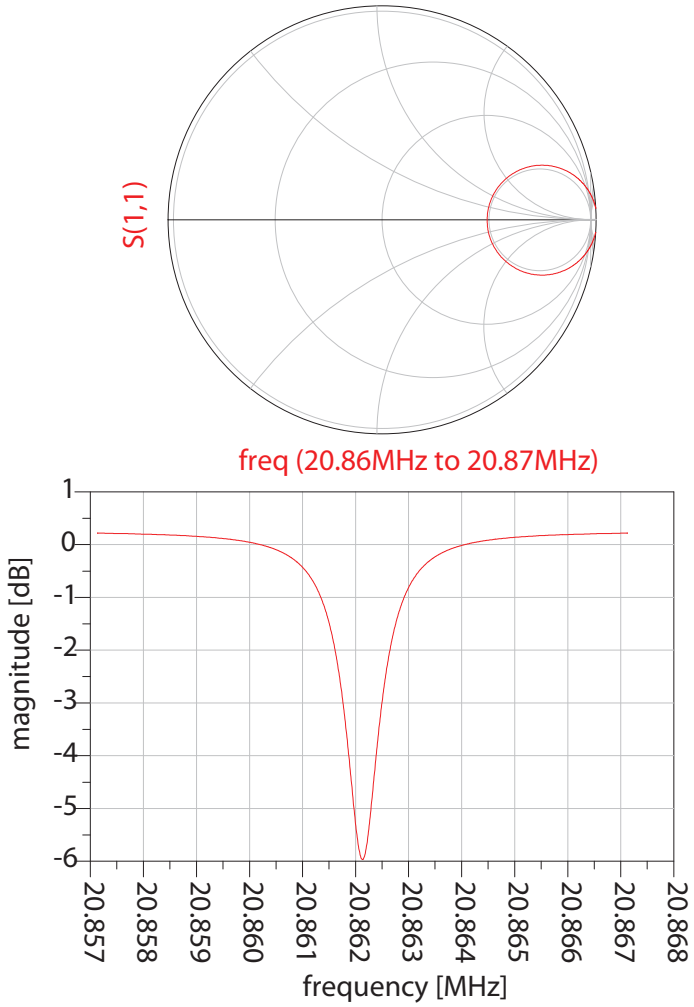

Figure A.9.: Example for an ADS simulation result using the RLC equivalent circuit and the model in order to describe the reduced loss when cooled (see Figure A.8).

Bibliography

[1] P. A. M. Dirac, "The quantum theory of the electron," *Proceedings of the Royal Society of London. Series A*, vol. 117, no. 778, pp. 610 – 624, 1928.

[2] F. Close, *Antimatter*. New York: Oxford University Press, 2009.

[3] C. D. Anderson, "The positive electron," *Phys. Rev.*, vol. 43, pp. 491 – 494, Mar. 1933.

[4] O. Chamberlain, E. Segrè, C. Wiegand, and T. Ypsilantis, "Observation of antiprotons," *Phys. Rev.*, vol. 100, pp. 947 – 950, Nov. 1955.

[5] B. Cork, G. Lambertson, O. Piccioni, and W. Wenzel, "Antineutrons produced from antiprotons in charge-exchange collisions," *Phys. Rev.*, vol. 104, pp. 1193 – 1197, Oct. 1956.

[6] M. Gell-Mann, "A schematic model of baryons and mesons," *Physics Letters*, vol. 8, no. 3, pp. 214 – 215, 1964.

[7] G. Zweig, "An SU_3 model for strong interaction symmetry and its breaking part I," *CERN Report*, p. 24, Jan. 1964.

[8] G. Zweig, "An SU_3 model for strong interaction symmetry and its breaking part II," *CERN Report*, p. 80, Feb. 1964.

[9] J. Ellis, "Beyond the standard model with the LHC," *Nature*, vol. 448, pp. 297 – 301, Jul. 2007.

[10] D. Kazakov, S. Lavignac, and J. Dalibard, eds., *Particle physics beyond the Standard Model*, vol. 84 of *Lecture Notes of the Les Houches Summer School 2005*. Amsterdam: Elsevier, 2006.

[11] C. Amsler, M. Doser, *et al.*, "Review of particle physics," *Physics Letters B*, vol. 667, no. 1 – 5, pp. 1 – 6, 2008. Review of Particle Physics.

[12] D. Griffiths, *Introduction to elementary particles*. Berlin: Wiley-VCH, 2nd ed., 2008.

[13] C. Bernardini, G. Corazza, G. Ghigo, and B. Touschek, "The Frascati storage ring," *Il Nuovo Cimento*, vol. 18, pp. 1293 – 1295, 1960.

[14] G. Budker, "An effective method of damping particle oscillations in proton and antiproton storage rings," *Soviet Atomic Energy*, vol. 22, pp. 438 – 440, 1967.

[15] I. Meshkov, "Electron cooling: Remembering and reflecting," *Proceedings of EPAC 2004*, pp. 244 – 248, 2004.

[16] S. van der Meer, "Stochastic damping of betatron oscillations in the ISR," Tech. Rep. CERN-ISR-PO-72-31. ISR-PO-72-31, CERN, Geneva, Aug. 1972.

[17] S. van der Meer, "Stochastic cooling and the accumulation of antiprotons," *Rev. Mod. Phys.*, vol. 57, pp. 689 – 697, Dec. 1984. Nobel lecture.

[18] P. Bramham, G. Carron, H. Hereward, K. Hübner, W. Schnell, and L. Thorndahl, "Stochastic cooling of a stored proton beam," *Nuclear Instruments and Methods*, vol. 125, no. 1, pp. 201 – 202, 1975.

[19] G. Baur *et al.*, "Production of antihydrogen," *Physics Letters B*, vol. 368, no. 3, pp. 251 – 258, 1996.

[20] D. Wineland, P. Ekstrom, and H. Dehmelt, "Monoelectron oscillator," *Phys. Rev. Lett.*, vol. 31, pp. 1279 – 1282, Nov. 1973.

[21] P. B. Schwinberg, R. S. Van Dyck, and H. G. Dehmelt, "New comparison of the positron and electron g factors," *Phys. Rev. Lett.*, vol. 47, pp. 1679 – 1682, Dec. 1981.

[22] L. Brown and G. Gabrielse, "Geonium theory: Physics of a single electron or ion in a Penning trap," *Reviews of Modern Physics*, vol. 58, pp. 233 – 311, Jan. 1986.

[23] G. Gabrielse, X. Fei, K. Helmerson, S. L. Rolston, R. Tjoelker, T. A. Trainor, H. Kalinowsky, J. Haas, and W. Kells, "First capture of antiprotons in a Penning trap: A kiloelectronvolt source," *Phys. Rev. Lett.*, vol. 57, pp. 2504 – 2507, Nov. 1986.

[24] M. Amoretti *et al.*, "Production and detection of cold antihydrogen atoms," *Nature*, vol. 419, pp. 456 – 459, Oct. 2002.

[25] G. Gabrielse, N. S. Bowden, P. Oxley, A. Speck, C. H. Storry, J. N. Tan, M. Wessels, D. Grzonka, W. Oelert, G. Schepers, T. Sefzick, J. Walz, H. Pittner, T. W. Hänsch,

and E. A. Hessels, "Background-free observation of cold antihydrogen with field-ionization analysis of its states," *Phys. Rev. Lett.*, vol. 89, p. 213401, Oct. 2002.

[26] G. B. Andresen *et al.*, "Trapped antihydrogen," *Nature*, vol. 468, pp. 673 –676, Dec. 2010.

[27] C. Amole *et al.*, "Resonant quantum transitions in trapped antihydrogen atoms," *Nature*, vol. 483, pp. 439 – 443, Dec. 2012.

[28] T. W. Hänsch, "Nobel lecture: Passion for precision," *Rev. Mod. Phys.*, vol. 78, pp. 1297 – 1309, Nov. 2006.

[29] T. Eriksson, W. Bartmann, P. Belochitskii, H. Breuker, F. Butin, C. Carli, R. Kersevan, M. Martini, S. Maury, S. Pasinelli, G. Tranquille, and W. Oelert, "The Elena project: Progress in the design," in *Proceedings of the 3rd International Particle Accelerator Conference (IPAC) 2012*, (New Orleans), May 2012.

[30] B. Heckel, E. Adelberger, S. Baessler, J. Gundlach, M. Harris, C. Hoyle, S. Merkowitz, U. Schmidt, A. Sharp, G. Smith, and E. Swanson, "Results on the strong equivalence principle, dark matter, and new forces," *Advances in Space Research*, vol. 25, no. 6, pp. 1225 – 1230, 2000. Fundamental Physics in Space.

[31] M. M. Nieto and T. Goldman, "The arguments against 'antigravity' and the gravitational acceleration of antimatter," *Physics Reports*, vol. 205, no. 5, pp. 221 – 281, 1991.

[32] E. G. Adelberger, B. R. Heckel, C. W. Stubbs, and Y. Su, "Does antimatter fall with the same acceleration as ordinary matter?," *Phys. Rev. Lett.*, vol. 66, pp. 850 – 853, Feb. 1991.

[33] G. Y. Drobychev *et al.*, "Proposal for the AEGIS experiment at the CERN antiproton decelerator (Antimatter Experiment: Gravity, Interferometry, Spectroscopy)," Tech. Rep. SPSC-P-334. CERN-SPSC-2007-017, CERN, Geneva, Jun. 2007. Technical Report.

[34] A. Kellerbauer *et al.*, "Proposed antimatter gravity measurement with an antihydrogen beam," *Nuclear Instruments and Methods in Physics Research Section B: Beam Interactions with Materials and Atoms*, vol. 266, no. 3, pp. 351 – 356, 2008. Low Energy Positron and Positronium Physics – Proceedings of the XIV International Workshop on Low Energy Positron and Positronium Physics.

[35] M. Charlton, "Antihydrogen production in collisions of antiprotons with excited states of positronium," *Physics Letters A*, vol. 143, no. 3, pp. 143 – 146, 1990.

[36] C. H. Storry, A. Speck, D. L. Sage, N. Guise, G. Gabrielse, D. Grzonka, W. Oelert, G. Schepers, T. Sefzick, H. Pittner, M. Herrmann, J. Walz, T. W. Hänsch, D. Comeau, and E. A. Hessels, "First laser-controlled antihydrogen production," *Phys. Rev. Lett.*, vol. 93, p. 263401, Dec. 2004.

[37] M. H. Holzscheiter, M. Charlton, and M. M. Nieto, "The route to ultra-low energy antihydrogen," *Physics Reports*, vol. 402, no. 1 – 2, pp. 1 – 101, 2004.

[38] K. F. Canter, A. P. Mills, and S. Berko, "Efficient positronium formation by slow positrons incident on solid targets," *Phys. Rev. Lett.*, vol. 33, pp. 7 – 10, Jul. 1974.

[39] J. R. Danielson, T. R. Weber, and C. M. Surko, "Plasma manipulation techniques for positron storage in a multicell trap," *Physics of Plasmas*, vol. 13, no. 12, p. 123502, 2006.

[40] S. Ulmer, *First observation of spin flips with a single proton stored in a cryogenic Penning trap*. Ph.D. thesis, Johannes-Gutenberg Universität, Mainz, 2011.

[41] P. Smith, *Electronic applications of the Smith chart*. New York: McGraw-Hill Book Company, 1969.

[42] F. Caspers, "RF engineering basic concepts: the Smith chart," *CAS - CERN Accelerator School: RF for Accelerators*, p. 22, Jan 2012. Comments: 22 pages, contribution to the CAS - CERN Accelerator School: Specialised Course on RF for Accelerators; 8 - 17 Jun 2010, Ebeltoft, Denmark.

[43] A. H. R. Patterson and S. Gerber, *Performance of various types of resistors at low temperatures*. NASA Glenn Research Center, Aug. 2001. Test report.

[44] A. Hammoud, S. Gerber, R. Patterson, and T. MacDonald, "Performance of surface-mount ceramic and solid tantalum capacitors for cryogenic applications," in *Annual Report Conference on Electrical Insulation and Dielectric Phenomena*, pp. 572 – 576 vol. 2, Oct. 1998.

[45] M.-J. Pan, "Performance of capacitors under DC bias at liquid nitrogen temperature," *Cryogenics*, vol. 45, no. 6, pp. 463 – 467, 2005.

[46] A. Briggs, "Characterization of some chip resistors at low temperatures," *Cryogenics*, vol. 31, no. 11, pp. 932 – 935, 1991.

[47] Q. Li, C. Watson, R. Goodrich, D. Haase, and H. Lukefahr, "Thick film chip resistors for use as low temperature thermometers," *Cryogenics*, vol. 26, no. 8, pp. 467 – 470, 1986.

[48] F. Collins and W. Mathias, *High voltage chip resistors*. Ohmcraft, 2007. White paper.

[49] T. Barge and F. Collins, *Photo patterning resistors*. Ohmcraft, 2007. White paper.

[50] C. Yeager and S. Courts, "A review of cryogenic thermometry and common temperature sensors," *IEEE Sensors Journal*, vol. 1, pp. 352 – 360, Dec. 2001.

[51] Lake Shore Cryotronics Inc., *A comparison of physical property and performance characteristics of Lake Shore cernox resistance temperature sensors with commercially available thick film resistors*, Aug. 1993. Application note.

[52] Johanson Dielectrics, *High voltage surface mount MLCCs 250 - 6,000 VDC*, 2012. Datasheet.

[53] Agilent Technologies, Inc., *E5061B network analyzer*, Jul. 2011. Datasheet.

[54] S. Tietze, *Halbleiter-Schaltungstechnik*. Berlin: Springer, 12. Aufl. ed., 2002.

[55] S. Stahl, *Cryogenic low pass filter unit type KA-Fil 2a*. Stahl-Electronics, 2009. Datasheet.

[56] S. L. R. Kirschman and J. Lipa, "Infrared readout electronics," in *Evaluation of GaAs FETs for Cryogenic Readout*, 1992.

[57] IXYS, *Gallium arsenide Schottky rectifier*, 2001. Datasheet.

[58] IXYSRF/Directed Energy Inc., *Gallium arsenide Schottky rectifier*, 2003. Datasheet.

[59] Infineon Technologies AG, *Silicon Schottky diode*, 2006. Datasheet.

[60] D. J. Wineland and H. G. Dehmelt, "Principles of the stored ion calorimeter," *Journal of Applied Physics*, vol. 46, pp. 919 – 930, Feb. 1975.

[61] S. Peil, *Quantum jumps between Fock states of an ultracold electron cyclotron oscillator*. Ph.D. thesis, Harvard University, 1999.

[62] X. Feng, M. Charlton, M. Holzscheiter, R. A. Lewis, and Y. Yamazaki, "Tank circuit model applied to particles in a Penning trap," *Journal of Applied Physics*, vol. 79, no. 1, pp. 8 – 13, 1996.

[63] H. Häffner, T. Beier, S. Djekic, N. Hermanspahn, H.-J. Kluge, W. Quint, S. Stahl, J. Verdu, T. Valenzuela, and G. Werth, "Double Penning trap technique for precise g factor determinations in highly charged ions," *European Physical Journal. D, Atomic, molecular and optical physics*, vol. 22, no. 2, pp. 163 – 182, 2003.

[64] D. H. E. Dubin, "Theory of electrostatic fluid modes in a cold spheroidal non-neutral plasma," *Phys. Rev. Lett.*, vol. 66, pp. 2076 – 2079, Apr. 1991.

[65] J. J. Bollinger, D. J. Heinzen, F. L. Moore, W. M. Itano, and D. J. Wineland, "Low order modes of an ion cloud in a Penning trap," *Physica Scripta*, vol. 46, no. 3, p. 282, 1992.

[66] U. Warring, *Laser spectroscopy on Os^-: A prerequisite for the laser cooling of atomic anions.* Ph.D. thesis, Ruperto-Carola University, Heidelberg, 2009.

[67] W. Macalpine and R. Schildknecht, "Coaxial resonators with helical inner conductor," *Proceedings of the IRE*, vol. 47, pp. 2099 – 2105, Dec. 1959.

[68] R. Schiffel and A. Köhler, *Werkbuch Hochfrequenz Technik - Grundlagen, Formelsammlung, Datensammlung, Bauelemente und Diagramme.* München: Franzis Verlag GmbH, Reprint-Ausgabe ed., 2003.

[69] F. E. Terman, *Radio engineer's handbook.* New York and London: McGraw-Hill Book Company, Inc., 1943.

[70] S. Ulmer, H. Kracke, K. Blaum, S. Kreim, A. Mooser, W. Quint, C. C. Rodegheri, and J. Walz, "The quality factor of a superconducting RF resonator in a magnetic field," *Review of Scientific Instruments*, vol. 80, no. 12, p. 123302, 2009.

[71] D. Phillips, *A precision comparison of the $\bar{p}$-p charge-to-mass ratios.* Ph.D. thesis, Harvard University, 1996.

[72] W. H. Hartwig and C. Passow, *RF superconducting devices.* New York: Academic Press, third ed., 1975.

[73] S. Ulmer, "Entwicklung eines experimentellen Aufbaus zur Messung des g-Faktors des Protons in einer Penning-Falle," Master's thesis, Johannes-Gutenberg Universität, Mainz, 2006.

[74] **T. Kaltenbacher**, F. Caspers, M. Doser, A. Kellerbauer, and W. Pribyl, "Resistive cooling circuits for charged particle traps using crystal resonators," *Review of Scientific Instruments*, vol. 82, no. 11, p. 114702, 2011.

[75] N. Gufflet, *Quartz crystal resonators*. KVG Quartz Crystal Technology, Aug. 2005. Report.

[76] R. Brendel, C. E. Hassani, M. Brunet, and E. Robert, "Influence of magnetic field on quartz crystal oscillation," *IEEE Conference Publications*, 1989. Proceedings of the 43rd Annual Symposium on Frequency Control.

[77] J. Rychen, T. Ihn, P. Studerus, A. Herrmann, K. Ensslin, H. J. Hug, P. J. A. van Schendel, and H. J. Güntherodt, "Operation characteristics of piezoelectric quartz tuning forks in high magnetic fields at liquid helium temperatures," *Review of Scientific Instruments*, vol. 71, no. 4, pp. 1695 – 1697, 2000.

[78] J. Aslam and W. Weyhmann, "A tunnel diode NMR spectrometer," *Review of Scientific Instruments*, vol. 44, no. 1, pp. 71 – 72, 1973.

[79] B. Lengeler, "Semiconductor devices suitable for use in cryogenic environments," *Cryogenics*, vol. 14, no. 8, pp. 439 – 447, 1974.

[80] J. Suter, "Piezoelectric properties of quartz crystal resonators below 10 K," *Cryogenics*, vol. 30, no. 6, pp. 547 – 548, 1990.

[81] N. Sclar and D. Pollock, "On diode thermometers," *Solid-State Electronics*, vol. 15, no. 5, pp. 473 – 480, 1972.

[82] S. Gong, H. Shen, and N. Barker, "Study of broadband cryogenic DC-contact RF MEMS switches," *IEEE Transactions on Microwave Theory and Techniques*, vol. 57, pp. 3442 – 3449, Dec. 2009.

[83] E. Carrasco, M. Barba, B. Reig, C. Dieppedale, and J. Encinar, "Characterization of a reflectarray gathered element with electronic control using ohmic RF MEMS and patches aperture-coupled to a delay line," *IEEE Transactions on Antennas and Propagation*, vol. 60, pp. 4190 – 4201, Sep. 2012.

[84] R. C. Richardson, *Experimental techniques in condensed matter physics at low temperatures*. United States: Basic Books, new ed., 1998.

[85] N. A. Walter and J. J. Scialdone, *Outgassing data for selecting spacecraft materials*. National Aeronautics and Space Administration, revision 4 ed., Oct. 1997. NASA-RP-1124-REV-4.

[86] R. W. Powell, R. P. Tye, and M. J. Woodman, "Thermal conductivities and electrical resistivities of the platinum metals," *Platinum Metals Review*, vol. 6, pp. 138 – 143, Oct. 1962.

[87] R. Vaccarone and F. Möller, "Cryogenic behavior of piezoelectric bimorph actuators," *Advances in Cryogenic Engineering*, vol. 46, no. 468, pp. 275–282, 2000.

[88] N. Oukhanski, M. Grajcar, E. Il'ichev, and H.-G. Meyer, "Low noise, low power consumption high electron mobility transistors amplifier, for temperatures below 1 K," *Review of Scientific Instruments*, vol. 74, no. 2, pp. 1145 – 1146, 2003.

[89] Agilent Technologies, *Techniques & applications for high throughput & stable characterization (AN 356-1)*, 1988. Application note.

[90] P. Horowitz and W. Hill, *The art of electronics*. Cambridge: Cambridge University Press, second ed., 1989.

[91] S. Ulmer, K. Blaum, H. Kracke, A. Mooser, W. Quint, C. Rodegheri, and J. Walz, "A cryogenic detection system at 28.9 MHz for the non-destructive observation of a single proton at low particle energy," *Nuclear Instruments and Methods in Physics Research Section A: Accelerators, Spectrometers, Detectors and Associated Equipment*, vol. 705, pp. 55 – 60, 2013.

[92] B. D'Urso, B. Odom, and G. Gabrielse, "Feedback cooling of a one-electron oscillator," *Phys. Rev. Lett.*, vol. 90, p. 043001, Jan. 2003.

[93] C. H. Suh and A. van der Ziel, "A noise spectrum described by a distribution in time constants," *Applied Physics Letters*, vol. 37, no. 6, pp. 565 – 566, 1980.

[94] C. Suh, A. van der Ziel, and R. Jindal, "1/f noise in GaAs MESFETS," *Solid-State Electronics*, vol. 24, no. 8, pp. 717 – 718, 1981.

[95] M. Fujiwara, M. Sasaki, and M. Akiba, "Reduction method for low-frequency noise of GaAs junction field-effect transistor at a cryogenic temperature," *Applied Physics Letters*, vol. 80, no. 10, pp. 1844 – 1846, 2002.

[96] N. H. Balshaw, *Practical cryogenics: An introduction to laboratory cryogenics*. Oxford Instruments Superconductivity Limited., Apr. 1996. Manual.

[97] G. Massobrio, G. Massabrio, and P. Antognetti, *Semiconductor device modeling with SPICE*. Columbus: McGraw-Hill Prof Med/Tech, second ed., 1998.

[98] M. Shanbhag and T. Chow, "Cryogenic operation of 4H-SiC Schottky rectifiers," in *Proceedings of the 14th International Symposium on Power Semiconductor Devices and ICs*, pp. 129 – 132, 2002.